A Thesis Submitted for the Degree of PhD at the University of Warwick

Quantifying the Transient Interfacial Area During Slag-Metal Reactions

Stephen R. A. Spooner

A thesis submitted in partial fulfilment of the requirements for the degree of
Doctor of Philosophy in Engineering

University of Warwick

Warwick Manufacturing Group

January 2017

Contents

List of Figures **v**

List of Tables **xi**

Acknowledgments **xiii**

Declaration **xvi**

Chapter 1 Introduction **1**

- 1.1 Objectives of Study 3
- 1.2 Thesis Structure 4

Chapter 2 Underpinning Knowledge **6**

- 2.1 Modern History of the Steel Industry 6
- 2.2 The Integrated Steel Plant 7
  - 2.2.1 Coke Making 7
  - 2.2.2 Ironmaking 8
  - 2.2.3 Basic Oxygen Steelmaking 9
  - 2.2.4 Steel Forming and Finishing 10
- 2.3 The Basic Oxygen Furnace 11
  - 2.3.1 Further Dephosphorization Technologies 13
- 2.4 Phosphorus reaction: Thermodynamics and Kinetics 14
- 2.5 The Interfacial Area of reaction within the Emulsion 17
  - 2.5.1 Droplet Size Distribution 17
  - 2.5.2 Droplet Generation 20
  - 2.5.3 Residence Time 21
  - 2.5.4 Spontaneous Emulsification 21

2.6 Unresolved Findings from the Literature 23

Chapter 3 Formulating the Research Approach 25

3.1 Hypotheses 25
  3.1.1 Hypothesis 1 25
  3.1.2 Hypothesis 2 26
  3.1.3 Hypothesis 3 26
  3.1.4 Hypothesis 4 26
  3.1.5 Hypothesis 5 27
  3.1.6 Hypothesis 6 27
  3.1.7 Hypothesis 7 27
3.2 Hypothesis Approach 27
  3.2.1 Hypothesis 1 27
  3.2.2 Hypothesis 2 28
  3.2.3 Hypothesis 3 & 4 28
  3.2.4 Hypothesis 5 28
  3.2.5 Hypothesis 6 28
  3.2.6 Hypothesis 7 29

Chapter 4 Experimental Methods 30

4.1 Pilot Plant Based Experiments 30
4.2 High-Temperature Confocal Scanning Laser Microscopy 31
4.3 X-ray Computed Tomography 32
4.4 Phase-Field Simulation 34
4.5 Additional Analytical Techniques 36
  4.5.1 Scanning Electron Microscopy (WDS and SIMS) 36
  4.5.2 XRF, ICP and LA-ICPMS 36
4.6 Materials 37
4.7 Technical Approach 39

Chapter 5 Calculating the Macroscopic Dynamics of the Gas/Metal/Slag Emulsion During Steelmaking 41

5.1 Hypothesis to be Interrogated 41
5.2 Introduction 41

5.3 Experimental 45
5.3.1 Heat Characteristics 45
5.3.2 Model of BOS Converter for Calculating Macroscopic Dynamics 47
5.3.3 X-ray Computed Tomography 51
5.4 Results 52
5.4.1 Amount of Metal in the Emulsion 53
5.4.2 Average Residence Time in the Emulsion 53
5.4.3 Metal Circulation Rate in the Emulsion 53
5.4.4 XCT Results of Slag/Gas/Metal Emulsion Samples 53
5.5 Discussion 58
5.5.1 Residence Times 58
5.5.2 % Tap Weight in the Emulsion 61
5.5.3 Metal Circulation Rates 62
5.5.4 Evaluation of Assumptions 63
5.5.5 Consideration of Original IMPHOS Conclusions 65
5.6 Conclusions 66

Chapter 6 Investigation into the Cause of Spontaneous Emulsification of a Free Steel Droplet; Validation of the Chemical Exchange Pathway 68

6.1 Hypothesis to be Interrogated 68
6.2 Introduction 68
6.3 Experimental 72
6.3.1 Materials & Methods 72
6.3.2 High-Temperature Confocal Scanning Laser Microscope . . . 73
6.3.3 X-ray Computer Tomography 74
6.3.4 Chemical Analysis 74
6.4 Results and Discussion 75
6.4.1 The Pathways of Emulsification 76
6.4.2 Chemical Analysis of System 1 78
6.4.3 System 2, Dynamic Changes in Surface Area 82
6.4.4 System 3, Validation of Chemical Exchange Causing Spontaneous Emulsification 83

6.4.5 Mechanisms of Oxygen Transfer into the Droplet 84
6.5 Conclusions and Revisiting the Hypothesis 87

Chapter 7 Quantifying the Pathway and Predicting Spontaneous Emulsification During Material Exchange in a Two Phase Liquid System 88
7.1 Hypothesis to be Interrogated 88
7.2 Introduction 88
7.3 Experimental 90
7.3.1 Materials 90
7.3.2 High-Temperature Confocal Scanning Laser Microscopy . . . 91
7.3.3 Micro X-ray Computer Tomography 92
7.3.4 Phase-Field Modelling 93
7.4 Results and Discussion 93
7.5 Conclusion 116

Chapter 8 Spontaneous Emulsification as a Function of Material Exchange 118
8.1 Hypothesis to be Interrogated 118
8.2 Introduction 118
8.2.1 Theoretical Consideration of Interfacial Tension 120
8.3 Experimental 122
8.4 Results 126
8.5 Discussion 131
8.6 Conclusions 138

Chapter 9 Conclusions and Suggested Further Work 139
9.1 Conclusions 139
9.1.1 Macroscopic Dynamics 139
9.1.2 Driving Force of Spontaneous Emulsification 140
9.1.3 Physical Pathway of Spontaneous Emulsification 141
9.2 Potential Industrial Impact 141
9.3 Suggested Further Work 142

Appendix A Appendix 1: Method of determining perturbation length 156

List of Figures

1.1 Global production statistics (2013) with relation to tonnage. [2] . . . 2
1.2 Phosphorus impurity levels in ore sources around the globe. 2

2.1 A schematic of the modern integrated steel mill [7]. 8
2.2 Schematic of the BOF, whith key phases/locations labled [24]. . . . 13
2.3 The kinetic steps required for phosphorus removal from liquid steel. 17

4.1 The High-Temperature Confocal Scanning Laser Microscope. a) Shows a broader image of the instrument complete with both the high-temperature and tensile/compression stage. b) Shows the interior of the high temperature chamber. 31
4.2 A schematic representation of image formation in the XCT process [62]. 33

5.1 Schematic of MEFOS 6 ton converter with sample levels, dimensions and S_{pv}/E_v defined 46
5.2 The amount of metal in the emulsion as a percentage of final tap weight. a) "Mid blow inflection" group, b) "High start then fluctuation" group, c) "Residual heats" group. 54
5.3 The average residence time as a function of blow time. a) "Mid blow inflection" group, b) "High start then fluctuation" group, c) "Residual heats" group. 55
5.4 Metal circulation rates in the emulsion as a function of blow time. a) "Mid blow inflection" group, b) "High start then fluctuation" group, c) "Residual heats" group. 56
5.5 2D orthoslice of the 3D volume. There is a clear contrast between the steel (whitest), the slag (grey) and porosity within the sample (black). 57

5.6 3D segmentation with semi-transparent slag phase in order to see the dispersion of metal droplets (light grey). 57
5.7 Rates of decarburization from IMPHOS analysis. a) “Mid blow inflection” group, b) “High start then fluctuation” group, c) “Residual heats” group. 60
5.8 Rates of dephosphorization from IMPHOS analysis. a) “Mid blow inflection” group, b) “High start then fluctuation” group, c) “Residual heats” group. 61

6.1 Reconstructed images from XCT scanning, showing only the metal fraction of the sample 77
6.2 2D slice of 95 second sample showing the orientation of the domed part of the sample 78
6.3 Measured oxygen concentration as a function of depth into the 20s sample (using a cross section) from Assis *et al* [62] 79
6.4 Expected oxygen concentration profile as a function of reaction time (LA-ICPMS only available at 20s) 80
6.5 Low magnification SEM picture of 'P-rich' particles 81
6.6 Metal droplet 3D spatial geometry for different holding times in system 2 82
6.7 Normalized surface area of metal droplets as a function of time, for system 2 where oxygen from the slag enters the droplet, and system 1 where phosphorus from the droplet is being refined to the slag . . 84
6.8 Ortho slice of CT scan of system 4 sample quenched at 90 seconds . 85

7.1 A 2D XCT reconstruction of a system at equilibrium, where the metal droplet is displayed in white, the slag in light grey, the crucible in dark grey and porosity as black (3μm resolution scan). 94
7.2 A three step sequence showing the quiescent droplet in the equilibrium system with time as imaged by the HT-CSLM through a transparent slag. 95
7.3 Reconstructed XCT images of the $Fe - FeO$ system quenched at defined times; only the metal part of the sample is displayed in light grey (3 μm resolution scan). 96

7.4 3D reconstructions of the 20- and 25-second samples, with the addition of the segmented perturbations displayed in colour dependent on length of protrusion from the segmentation sphere. 98
7.5 The quantified surface area of the metal droplet in the $Fe - FeO$ system with time from XCT analysis, along with the expected surface area of the null experiment assuming a perfectly quiescent sphere; the null experiment surface area reduces with time due to slight oxidation as modelled using the equilibrium module in Factsage^{TM}. 99
7.6 The programmed heating cycle of the HT-CSLM, showing a slow early heating regime and a quench point on cooling for protection of the equipment against thermal shock. 99
7.7 An image time step of the $FeAl - SiO_2$ system as visualised by the HT-CSLM at lower magnification; the droplet can be seen to grow in size, spread and perturbations are observable surrounding it, followed by dispersion into a cloud covering the field of view before coalescence. 100
7.8 Emulsification visualization of the $FeAl - SiO_2$ system at higher resolution via the HT-CSLM. As noted in the main text, the HT-CSLM effectively views a 2D slice of the sample; this results in perturbations from lower in the sample appearing as a halo of in-focus white line or spots around the parent droplet such as seen at 9 seconds, this is also the reason the image at 11 seconds shows a continuous metal phase, as overlapping droplets will appear as one mass. 101
7.9 3D reconstructions of the quenched $FeAl - SiO_2$ system where the crucible and slag phases have been removed to expose the metal phase of the sample in free space. 102
7.10 A graphical representation of the surface area change of the $Fe - FeO$ and $FeAl - SiO_2$ systems as measured through XCT, as well as the volume change of the $Fe - Al$ droplet mass with time and the modelled surface area change within the null experiment. 103
7.11 Selected graphical outputs from the 2D $Fe - FeO$ phase-field modelling showing the progression from a quiescent sphere to a highly perturbed state where material has begun to break away from the parent droplet. 104

7.12 3D graphical outputs from the $FeAl - SiO_2$ phase-field model, where the full life cycle of emulsification and coalescence can be seen within the simulated 70,000 time steps. 105
7.13 a) 2D ortho slices of the XCT 20- and 25-second reconstructions where the metal phase is in light grey, slag in dark grey and porosity in black. b) Magnified section of the 20- and 25-second ortho slice images where each growth cycle stage of a perturbation as identified from the phase-field modelling has been highlighted as present in the experimental samples. 106
7.14 Graphical display of the transient surface area as measured via XCT for experimental samples and output geometries from the phase-field model; experimental samples have been time-step normalized through comparison of in-situ HT-CSLM with phase-field results. 107
7.15 Perturbation dimensions for the 20-second $Fe - FeO$ sample. 108
7.16 Perturbation dimensions for the 25-second $Fe - FeO$ sample. 108
7.17 Examples of the perturbation geometries displayed in 3D space as produced via the XCT segmentation method implemented. 109
7.18 Perturbation height/width ratio distribution for the 20- and 25-second samples truncated to represent close to 85% of the total perturbations from each sample. 110
7.19 The computed distribution of surface tension through and in close proximity to a growing perturbation (t*=15000, 20000, 30000 and 35000 δ t). 113
7.20 The simulated variation of chemical composition, specifically aluminium content as a distribution through the metal droplet (t*=15000, 20000, 30000 and 35000 δ t). 114
7.21 The gradient of driving force for perturbation growth and breakaway as a combination of chemical free energy and interfacial energy in close time proximity before and after material break away (t* =20000 and 35000 δ t). 115

8.1 A schematic of the interface between a molten iron droplet (black particles) and a molten oxide suspension medium (grey particles). An Al atom is present at the interface (red) with examples of inter (E^{P1-1}) and intra (E^{P1-2}) phase interactions depicted. 121

8.2 The nominal heating cycle used for both pre-melting of metal oxides and experimentation of oxide/metal alloy reaction in the HT-CSLM. 124

8.3 Images of the sectioned quenched samples showing the droplet suspended in the oxide phase and the reduction in metal recovery in higher Al content systems. a) 0% $FeAl$, b) 3% $FeAl$, c) 5% $FeAl$. . 126

8.4 Time step images of the 5% $FeAl$ experiment as seen in the HT-CSLM. In focus metal phases appear as lighter in grey scale and the molten metal oxide phase is seen as black. a)-f) show the cycle of perturbation-emulsification and finally coalescence. 127

8.5 Time step images of the 4% $FeAl$ experiment as seen in the HT-CSLM. In focus metal phases appear as lighter in grey scale and the molten metal oxide phase is seen as black. a)-f) show the cycle of perturbation-emulsification and finally coalescence. 128

8.6 Time step images of the 3% $FeAl$ experiment as seen in the HT-CSLM. In focus metal phases appear as lighter in grey scale and the molten metal oxide phase is seen as black. a)-f) show the cycle of perturbation growth with no emulsification seen. 129

8.7 Time step images of the 2% $FeAl$ experiment as seen in the HT-CSLM. In focus metal phases appear as lighter in grey scale and the molten metal oxide phase is seen as black. a)-f) show the cycle of perturbation growth to quiescent droplet. 129

8.8 Time step images of the 1% $FeAl$ experiment as seen in the HT-CSLM. In focus metal phases appear as lighter in grey scale and the molten metal oxide phase is seen as black. a)-f) show the cycle of perturbation growth to quiescent droplet. 130

8.9 The surface area ratio profiles as deduced from image analysis of the HT-CSLM video (to the nearest 0.05). 1 in 15 frames have been analysed but only the points corresponding to those in figures 8.4-8.8 are highlighted. 130

8.10 A schematic of the interface between an iron aluminium metal alloy (black particles represent iron atoms, red particles represent aluminium atoms) and a metal oxide medium (specifically silica molecules, grey particles). An example of perturbation growth and necking is given with varying diffusion distances of SiO_2 bulk particles to perturbation head ($SiO_{2-B}Al_{-H}$, neck ($SiO_{2-B}Al_{-N}$) and bulk droplet ($SiO_{2-B}Al_{-D}$) qualitatively depicted. The strain angle θ as a result of necking is also indicated. 134

8.11 Global interfacial tension during the increase and reduction of interfacial area as measured for the 8% $FeAl$ sample coupled with the free energy gain of reaction to equilibrium for the 8, 5, 4, 3, 2, and 1% FeAl systems. Period A is during initial light perturbation, B during heavy perturbation, C fully emulsified, D ongoing coalescence and E a fully coalesced droplet. 137

A.1 An example of the sphere created from the minima averaging of perturbations 156

A.2 a) A 2D slice of the 20-second sample, where the metal has been highlighted in blue and all other material removed. b) The resultant volume left after removal of the interior of the droplet through overlapping of the minima averaging sphere. 157

A.3 The effective segmentation of the droplet surface as a result of the automated method within the software splitting at defined minima. Each colour represents a separately defined perturbation. 158

A.4 The grey-scale distribution of the sample space as defined from the original average minima produced sphere size. The black circle is in the space of the sphere and the grey values lighten radially outwards from its surface. 158

List of Tables

4.1 IMPHOS heats and their starting “hot metal” compositions collected by spark optical emission spectrometry. [4]. 37

4.2 The compositions of all metallic alloys used in HT-CSLM experiments measured using ICP (where all N levels are <0.001%. 38

4.3 The compositions of all slags used in HT-CSLM experiments measured using XRF. 38

5.1 Collation of previously reported residence times, with the experimental/modelling technique used. 44

5.2 Nominal start composition of hot metal used in IMPHOS trials. . . . 45

5.3 XCT scanning parameters used for the interrogation of solid emulsion shards removed from the sampling pots. 51

5.4 Overall average and SD of %Tw, t_r, and MCR for all blows. 52

5.5 Initial results from XCT scanning of shard emulsion samples. The number of discrete metal packages detected and their average diameter. 58

6.1 A summary of the previous findings of metal droplet size in oxygen steelmaking emulsions. 70

6.2 XRF detected chemical composition of master slags, used in this study and by Assis et al. 72

6.3 ICP detected chemical composition of Fe- alloys used in this study. . 73

6.4 Heating and quenching regime of all samples. ## being the period of time a sample was held at high temperature for. 73

6.5 Parameters used within the two scanners. * There is an additional focusing step performed by an optic in the Zeiss machine, where x0.4 was used in this study. 75

6.6 Summary of chemical analysis performed using the various techniques described 79
6.7 Raw data for surface area measurements of system 3. 83
6.8 Raw data for volume measurements of system 2. 83

7.1 Compositions of $FeAl$ alloys used for the experiments in HT-CSLM presented in mass %. Compositions were measured by ICP. 111

8.1 Compositions of $FeAl$ alloys used for the experiments in HT-CSLM presented in mass %. Compositions were measured by ICP (all alloys contained <0.001 %N). 122
8.2 Composition of the metal oxide mixture used for HT-CSLM experimentation after pre-melting of reagent grade hand-mixed powders presented in mass %. Compositions were measured by XRF. 123
8.3 Literature values used for calculation of global interfacial tension and dissipation of free energy as displayed in figure 8.11. 136

Acknowledgements

There are many people who have aided the pathway to completing this thesis, all of whom I wish to express gratitude to. . . however I will keep it short.

To begin, I wish to thank Professor Sridhar Seetharaman. You created an environment to not only conduct exciting and interesting research, but also make friends, develop myself and interact with the wider steel community. It has been a great experience from the early days when I asked “when will there be more than two people?” to the now spectacle of diversity there is within the group. I doubt many see such change and progression during time as a student. The understanding and trust you give to students creates a unique environment to challenge the experienced and peruse the bold.

Deepest gratitude to:
Professor Mark Williams, Dr Jason Warnett, Dr Alireza Rahnama, Dr Zushu Li, Dr Andre Assis, Dr Mohammed Tayeb, Dr Carl Slater, Dr Rohit Bhagat, Professor Richard Fruehan, Dr Hongbin Yin colleagues, co-workers and Dr Alison Lusty.
- Your support, guidance, knowledge and time, has been inspiring and invaluable.

I would like to thank Tata Steel, and EPSRC for proposing and funding the project.

In addition I would like to thank:
Deborah Spooner (Mum), John Spooner (Dad), David McGovern and further family and friends who both remain and have moved on.
- Your friendship, help and love have been a light of encouragement.

Victoria Lusty, I have not forgotten you, nor will I ever. Somehow you kept me going, even when I was trying not to. With grace and humility you have driven me to continue. My adoration and thanks are yours.

“The duty of youth is to challenge corruption” - Kurt Cobain

“Learning never exhausts the mind” - Leonardo da Vinci

Declaration

This thesis is submitted to the University of Warwick in support of my application for the degree of Doctor of Philosophy. It has been composed by myself and has not been submitted in any previous application for any degree The work presented (including data generated and data analysis) was carried out by the author except in the cases outlined below:

- X-ray Computer Tomography scanning and image analysis was carried out by Dr Jason Warnett
- Phase-field modelling was conducted by Dr Alireza Rahnama
- Chemical analysis of metal/slag droplet experiments was conducted by Dr Andre Assis

Inclusion of Published Work

Parts of this thesis have been published by the author:

1. Spooner, S., Assis, A. N., Warnett, J., Fruehan, R. Williams, M. A. & Sridhar, S., "CTSSC-EMI Symposium CSLM , XCT Couple Interrogation of the Emulsification Interaction between Free Steel Droplets Suspended in Steel Making Slags". *EMMISYMP*, Tokyo, (September, 2015).
2. Spooner, S., Warnett, J. M., Bhagat, R., Williams, M. A. & Sridhar, S., "Calculating the Macroscopic Dynamics of Gas/Metal/Slag Emulsion during Steelmaking". *ISIJ Int.* (2016). doi:10.2355/isijinternational.ISIJINT-2016-361
3. Spooner, S., Assis, A. N., Warnett, J., Fruehan, R. Williams, M. A. & Sridhar, S.,"Investigation into the Cause of Spontaneous Emulsification of a Free Steel

Droplet; Validation of the Chemical Exchange Pathway". *Metall. Mater. Trans. B* (2016). doi:10.1007/s11663-016-0700-3

4. Tayeb, M. A., Spooner, S., & Sridhar, S., "Phosphorus: the noose of sustainability and renewability in steelmaking". *JOM*, 66 (9) (2014), 1565-1571
5. Assis, A. N., Warnett, J. M., Spooner, S., Williams, M. A., & Sridhar, S., "Spontaneous Emulsification of a Metal Drop Immersed in Slag Due to Dephosphorization: Surface Area Quantification". *Metall. Mater. Trans.* B 568-576 (2014). doi:10.1007/s11663-014-0248-z
6. *Under Submission* - Spooner, S., Rahnama, A., Warnett, J. M., Williams, M. A., & Sridhar, S., "Spontaneous Emulsification during Material Exchange in Two Phase Liquid Systems". *Sci. Rep.* (Submitted January 2017)
7. *Under Submission* - Spooner, S., Li, Z., & Sridhar, S., "Spontaneous Emulsification as a Function of Material Exchange". *Sci. Rep.* (Submitted January 2017)

During the period of study this thesis was produced, further findings were also published:

1. Slater, C., Spooner, S., Davis, C. & Sridhar, S. "Observation of the reversible stabilisation of liquid phase iron during nitriding". *Mater. Lett.* 173, 98-101 (2016).
2. Slater, C., Spooner, S., Davis, C. & Sridhar, S. "Chemically Induced Solidification: A New Way to Produce Thin Solid-Near-Net Shapes". *Metall. Mater. Trans. B: Process Metall. Mater. Process. Sci.* 47, 1-4 (2016).
3. Rahnama, A., Spooner, S. & Sridhar, S. "Control of intermetallic nano-particles through annealing in duplex low density steel". *Mater. Lett.* 189, 13-16 (2017).

Abstract

The steel industry is facing significant competition on a global scale due to the drive for light-weighting and cheaper more sustainable construction. Not aided by over-supply in geographic sectors of the industry, there is significant competition within the slowly shrinking sector. The recent growth in developing countries through installation of modern plant technology has led to the reduction in unique selling points for mature steelmaking locations. As such, to compete with the equalling product capability and innate cheaper production costs within developing areas the industries in Europe and North America require significant improvements in productivity and agile resource management. To date the basic oxygen furnace has been somewhat treated as a black box within industry, where only control parameters are monitored, not the fundamental mechanisms within the converter. Studies over the past 30 years have shown the basic oxygen furnace is unable to attain the thermodynamic minimum phosphorus content within the output liquid steel. Coupled with the need to drive down resource cost, with a potential for high content phosphorus ores the internal dynamic system of the basic oxygen furnace requires more rigorous understanding.

With the aid of in-situ sampling of a pilot scale basic oxygen furnace, and laboratory studies of individual metal droplets suspended in a slag medium (known to be a key driving environment for impurity removal) the present project aims to provide insight into the transient interfacial area between slag and liquid metal through basic oxygen steelmaking processing. Initially the macroscopic dynamics including the amount of metal suspended in the gas/slag/metal emulsion, the period of time it is suspended for, and the speed at which it moves, is investigated. It was found that these parameters vary greatly through the blow, with a normal peak in residence times near the beginning of the blow and a dramatic increase in metal circulation rates at the end of the blow, when foaming is reduced or collapsed. Further to this, a method of interrogating the size of metal droplets within the slag layer using X-ray computed tomography is introduced.

The study then progresses into the microscopic environments that individual droplets are subjected to during steel processing. Initially the cause of spontaneous emulsification in basic oxygen furnace type slags is investigated through high temperature-confocal scanning laser microscopy/X-ray computed tomography led experimentation, with the addition of null experiments conducted to rationalize the experimental technique. It was found that the flux of oxygen across the interface was the cause and thus the confirmation of material transfer across the interface being the driving force. Furthermore the physical pathway of emulsification is interrogated and quantified, with in-situ observation of spontaneous emulsification in the high temperature-confocal scanning laser microscope enabled through use of optically transparent slags. The life cycle of perturbation growth, necking and budding is observed and quantified through high-resolution X-ray computed tomography. In addition a phase-field model is developed to interrogate slag/metal systems in 2D and 3D variations, giving rise to the ability to track the cause of emulsification and to predict its occurrence.

Finally the project progresses with the in-situ investigation of spontaneous emulsification as a function of initial metal composition. The behaviour of droplet spontaneous emulsification is seen to reduce in severity and subsequently to decline into a non-emulsifying regime below a critical level. Free energy calculations coupled with a measure of the global interfacial tension increase give quantifiable reasoning as to the behaviour seen.

List of Abbreviations

%Tw	Percentage Tap Weight
BF	Blast Furnace
BOF	Basic Oxygen Furnace
BOS	Basic Oxygen Steelmaking
CFD	Computational Fluid Dynamics
DRI	Direct Reduced Iron
EAF	Electric Arc Furnace
HT-CSLM	High-Temperature Confocal Scanning Laser Microscopy
ICP-MS	Inductivly Coupled-Mass Spectroscopy
IMPHOS	Improved Phosphorus Refining
LA-ICPMS	Laser-Ablation Inductivly Coupled-Mass Spectroscopy
LD	Linz Donawitz
LD-LBE	LD-Lance Bubbling Equilibrium
LD-NRP	LD-Converter Type Dephosphorization Process
LD-ORP	LD-Converter Optimized Process
MURC	Multi Refining Converter Process
NRP	Ladle-type Dephosphorization Process
OHF	Open Hearth Furnace

RRS	Rosin-Rammler-Sperling
SE	Spontaneous Emulsification
SEM	Scanning Electron Microscope
SIMS	Secondary Ion Mass Spectroscopy
USA	United States of America
WDS	Wavelength Dispersive Spectroscopy
XCT	X-ray Computed Tomography
ZSP	Zero Slag Process

Chapter 1

Introduction

1.3 billion tons of steel were produced in 2015 across 65 countries [1] making it the largest industrially produced material in the world by weight. This along with overall significant growth of 30% since 2006 gives reason for the global need of the steel industry to adapt and survive. There are two main routes of production today: the Electric Arc Furnace (EAF) and the integrated Blast Furnace-Basic Oxygen Furnace (BF-BOF) route. Combined they account for 99% of steel production worldwide (30% and 69% respectively) with the remaining 1% through production via Open Hearth Furnace (OHF) and other processes [2]. The relative proportions differ widely from country to country with for example North America producing 60% of its steel through the EAF whereas Europe is heavily dependent on the BF-BOF route at 70% of total production. Scrap and hot metal are charged into the BOF whereas the EAF is mainly charged with scrap and pig iron; however recent and continued reduction in natural gas prices following successful shale rock exploration has encouraged the use of direct reduced iron (DRI) in North America and other countries rich in natural gas such as those in the Middle East [2].

DRI can be used to substitute scrap and pig iron, for both economic and compositional control reasons. With the extensive markets of China and India there is a huge overcapacity of production in local areas with the ability to undersell on the global stage. Figure 1.1 shows the global production of steel in each region of the world for 2013. As a result developed markets are searching for ways to stay competitive and justifiable in years to come. One way this is being explored is through diverse and untraditional approaches to steel production, for example end-point variable product control.

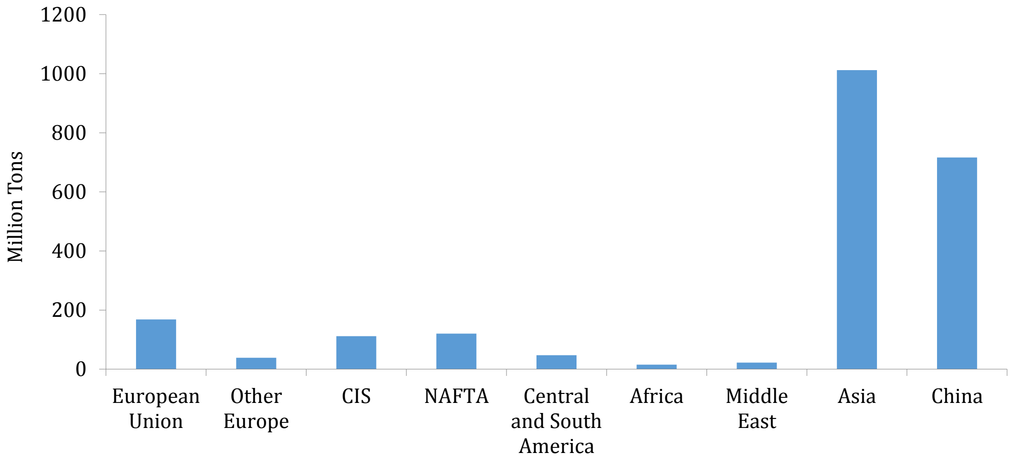

Figure 1.1: Global production statistics (2013) with relation to tonnage. [2]

With the price of iron ore exponentially growing in present years, the need for resource flexibility is integral to a sustainable primary steel industry. Sources of iron ore quality have great variability in levels of iron content, as well as impurity levels. Phosphorus is used as an example in figure 1.2, where cheaper ores from Peru and China for instance have much higher initial phosphorus content.

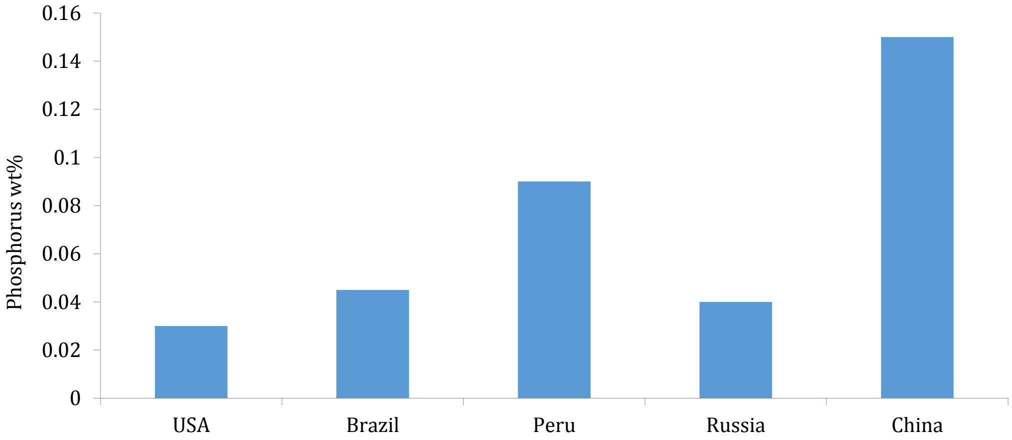

Figure 1.2: Phosphorus impurity levels in ore sources around the globe.

Predefined treatments for sulfur and optimised carbon removal process in the BOF leave phosphorus as a chemical restriction on usable ore within European plants. The BOF is relied upon for phosphorus removal; with the introduction of lime based slags providing a partitioning phase for refined phosphorus to be held. This process is however primarily operated and optimized for carbon removal from steel which has been heavily enriched during coke reduction in the BF [3]. As previously mentioned EAF's are primarily charged with scrap, however with the addition of DRI phosphorus content can again become an issue for steel product via this route.

Considering this the pathway and fundamental reaction kinetics of phosphorus removal is to be investigated under pseudo-industrial conditions. Data from the European Commission funded project "IMPHOS: Improved phosphorus refining" [4] in conjunction with lab-based emulsification experiments will be used to gain greater understanding into the fundamental conditions responsible for phosphorus removal. The aim of the project is to provide insight into factors which could be manipulated to increase overall BOF performance.

Currently P removal is through the partition between liquid metal and slurries of metal oxides (slag). This has been the provided pathway in steelmaking for many years. Studies of the last 30 years however have consistently reported the thermodynamic maximum partitioning of phosphorus is not attained through conventional BOF operation; thus current processes are kinetically hindered. Developments of further technologies such as torpedo ladle refining, double slagging and double converter refining have been explored and subsequently implemented in some countries (Japan, Korea and China mostly). These systems are working to combat higher purity demands of the consumer, for instance interstitial-free high strength pipeline steels. Although these systems are in place, they are for the most part incredibly inefficient, causing temperature loss from the hot metal and productivity reduction. The necessity for increase of workforce, large amount of excess waste and loss of material through ladle refining are further issues. For a sustainable industry more effective ways of combating phosphorus levels is desperately needed.

1.1 Objectives of Study

The overall objective of this project is to offer quantification to the transient interfacial area between liquid metal and metal oxide phases in the BOF. This is in order to provide insights into factors of influence for long term steel production and dynamic product design.

The study can be broken down into an investigation into the macroscopic dynamics within the BOF through use of IMPHOS data, giving improved knowledge of the quantity of metal, how long it is suspended and the circulation rates within the gas/slag/metal emulsion in the BOF. These findings will inform future models as to the potential of refining through quantification of interfacial area, as well as the turnover of reactive phases in contact with each other, and hence the level of sustained chemical potential while the interface is present.

Further to this the effects of refining on individual droplet dynamics will be investigated through the coupling of High-Temperature Confocal Scanning Laser Microscopy (HT-CSLM), X-ray Computed Tomography (XCT) and the further addition of phase-field modelling for predicting interfacial phenomena. Efforts will be made to define the cause, level of influence required and the pathway by which spontaneous emulsification occurs, in order to offer quantification as to the interfacial area development, as well as knowledge on how the phenomenon may be encouraged or prevented depending on the application. This study will be significantly relevant to slag/metal reaction in a broader scheme of steelmaking, such as those seen in ladles during secondary steelmaking, the tundish before casting, electro-slag refining, interaction with mould powders during casting and droplets generated in the HIsarna process. The physical pathway and ability to model spontaneous emulsification presents knowledge applicable further afield, such as to copper production, silicon nano-particle synthesis or waste recovery.

1.2 Thesis Structure

Following from this brief 1. “Introduction” the layout of the first half of this thesis follows an ordered path of: 2. “Underpinning knowledge”; in this section the basic background on steelmaking is presented, along with deeper discussion on the BOF, phosphorus reactions, droplet generation in the BOF, droplet residence times in the BOF and spontaneous emulsification previously witnessed in slag/metal reaction systems. 3. “Formulating the Research Approach”; where hypotheses are identified and the approach to interrogate them is discussed. 4. “Experimental Methods”; where the overarching techniques used within the study are introduced and briefly described (more in-depth comments on the experimental methods are given in the relevant results chapters).

Following on from these background chapters, the thesis contains four results chapters: 5. “Calculating the Macroscopic Dynamics of the Gas/Metal/Slag Emulsion During Steelmaking” where the transient environment of metal droplets in the BOF emulsion phase is interrogated; 6. “Investigation into the Cause of Spontaneous Emulsification of a Free Steel Droplet; Validation of the Chemical Exchange Pathway” which includes standardization of experimental techniques against those previously reported in the literature as well as rationalization as to why spontaneous emulsification occurs in the presented systems; 7. “Quantifying the Pathway and Predicting Spontaneous Emulsification During Material Exchange in a Two Phase Liquid System”, in this chapter the physical morphology of the perturbed droplet surface is examined along with the introduction of a phase-field model to offer the ability to predict spontaneous emulsification. 8. “Spontaneous Emulsification as a Function of Material Exchange”, finally the implication of material exchange on interfacial tension is discussed along with the interrogation of the phenomenon using the developed in-situ observation technique to study the level of material exchange required for emulsification to occur, this is rationalized through dissipation of free energy calculations.

Finally the experimental and modelling results are brought together in an encompassing “Conclusions and Suggested Further Work” section, where comments on the relevance and possible impact of findings to industrial practice are made along with suggestions of future work to guide the development and greater understanding of the findings and implications presented.

Chapter 2

Underpinning Knowledge

2.1 Modern History of the Steel Industry

Steel is an iron matrix alloy usually containing less than 1% carbon. It is used most frequently in the automotive, construction, pipes, and consumer goods sectors. Steel is produced in many shapes and forms including bars, sheets, wire, rod or pipe as needed by the intended consumer.

The process of steelmaking has undergone many changes in the last century based on the political, social and technological environment. In the 1950s and 60s, demand for high quality steel encouraged the industry to produce large quantities via integrated steel mills. Large integrated mills were thrust into the driving seat of the industry throughout the USA and Europe, with the ability to produce large quantities of consistent steel products from raw materials [2]. However these plants required high capital costs and were constructed with limited flexibility.

The 1970s saw thermal efficiency made a priority within steel production. Integrated plants contain an innate efficiency due to economies of scale and factors such as heat retention when dealing with large volume. Despite this, improvements in common production practices became vital to viability. Previously (1950s and 60s) steel production had been dominated via batch processes, as a result idle equipment was not uncommon as an individual batch was taken through each process stage from raw materials to finished product. Huge energy savings were made by the large scale uptake of processes such as continuous casting and the continuously supply of raw materials to the blast furnace.

As environmental concerns gained importance in the 1980s and 90s, regulations became more stringent again changing the steelmaking industry. By 1995, compliance with environmental legislation was estimated to make up 20-30% of the capital costs [5] for new steel production. Competition has also increased during the recent decades due to decreasing markets and increasing international steel capacity. The nature of alternative material use and global over-supply has driven reduction in production cost and an increase in product quality.

Global economics and legislation is driving a change to just-in-time technology through the mass uptake of mini-mill technology in the USA and other geographic sectors as opposed to the previously dominating status of integrated production. Mini-mills rely on steel scrap as a base material rather than ore. It is expected mini-mills will never completely replace integrated steel plants as they cannot maintain the tight control over chemical composition and thus cannot consistently produce high quality steel. Mini-mills work through a narrow production line and cannot produce the speciality products integrated plants currently provide. Technology however continues to improve and since the mid-1990s the introduction of direct reduced iron and pig iron sources to the scrap production route has allowed for access to a greater diversity of products [6].

2.2 The Integrated Steel Plant

Steel production through an integrated steel plant involves three primary product steps. First, the heat source used to melt iron ore is produced; followed by the melting and reduction of iron ore in the blast furnace; finally the molten metal is reacted with oxygen to form the low carbon compositions of steel. The steps can be conducted at one facility through an on-site power station and collocation of BF and BOS facilities. However power is often supplied from off-site producers. A schematic of a modern integrated mill is shown in figure 2.1.

2.2.1 Coke Making

Coke is the solid carbon fuel used to melt and reduce iron ore. Coke production begins with pulverised bituminous coal. The coal is fed into a coke oven, sealed and heated to around 1573 K for 14 to 36 hours. Coke is produced in a batch process, with multiple ovens operating simultaneously to offer a constant supply of material

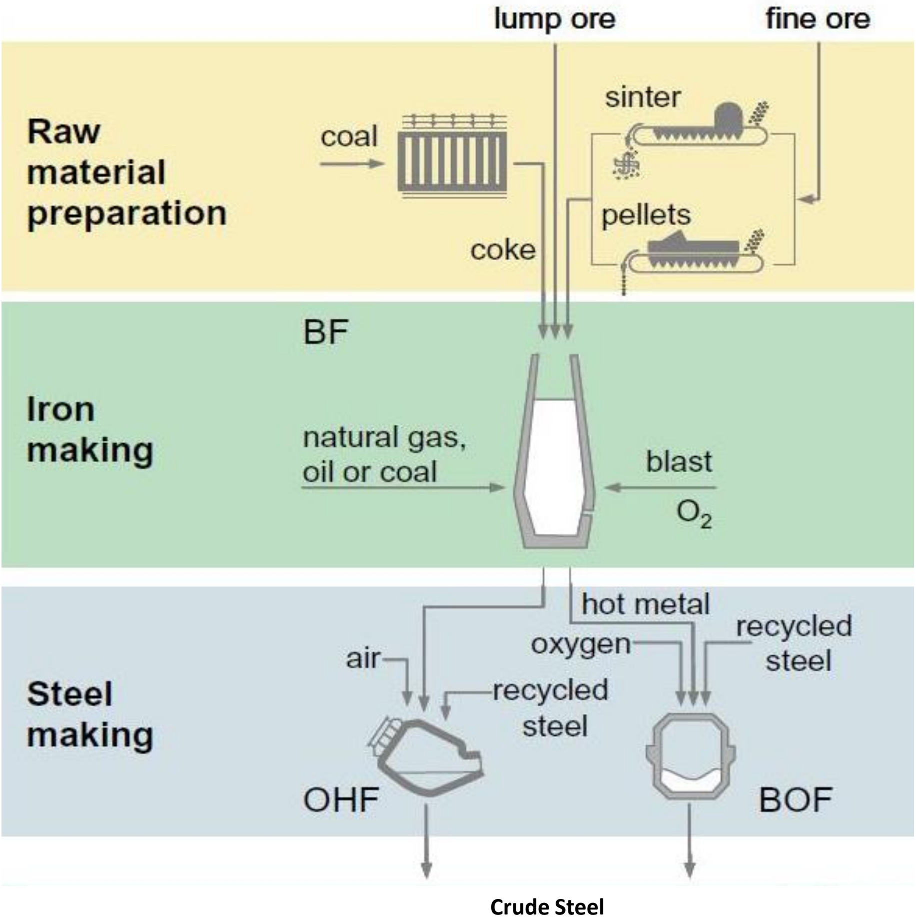

Figure 2.1: A schematic of the modern integrated steel mill [7].

to the BF.

Heat is frequently transferred from one oven to another, reducing energy requirements [8]. After the coking process is finished, the coke is moved to a quenching tower where it is cooled with water spray. Once cooled the coke is moved directly to an iron making furnace or into storage.

2.2.2 Ironmaking

During ironmaking, iron ore, coke, heated air and limestone or other fluxes are fed into the BF. The heated air causes the coke to combust, which provides heat and the carbon source for iron production. Limestone or variants (e.g. dolomite) are added to react with and remove the acidic impurities from the molten iron. The limestone-impurity mixture floats on the top of the liquid metal forming a slag and can be skimmed off during the continuous process.

Sintering products may also be added to the furnace. Sintering is the process in which solid wastes are combined into a porous mass which can be added to the BF. The wastes can include iron ore fines, pollution control dust, coke breeze, water treatment sludge and flux. Sintering plants help reduce solid waste by combusting waste products and capturing trace levels of iron present in the mixtures. Sintering plants are not used at all steel production sites [6] [9]. The process of iron making has issues of phosphorus carry over from the originating ore as well as coke additions.

2.2.3 Basic Oxygen Steelmaking

Molten iron from the BF is sent to the BOF. The BOF gives utility for the final refinement of the iron into steel. High purity oxygen is blown into the furnace via a top lance at supersonic speeds. The oxygen combusts with elements such as carbon and silicon in the molten iron. Further fluxes are fed into the BOF to offer a partitioning oxide phase for the removal of impurities such as phosphorus, manganese and titanium etc. Further to refining in the BOF, liquid steel often undergoes alloying steps within the ladle to deliver the required compositions.

The resulting steel is most often cast into slabs, beams or billets. Further shaping of the metal may be conducted within steel foundries, which re-melt the steel and pour the liquid into moulds, or at rolling facilities with both hot and cold conditions, depending on the desired product shape and properties.

Slag is a significant by-product of the BOF. Slag is essentially a slurry of metal oxides in liquid state. The most common components within slag of the steel industry are CaO, FeO (in variable oxidation states), Al_2O_3, SiO_2, MgO, Cr_2O_3, TiO_2, P_2O_5 and MnO. The ratio of these oxides affects the melting point, viscosity, and impurity partitioning capability along with other processing factors such as foam stability and refractory wear. Of the varying properties the slags basicity is often considered one of the more important features; the basicity is effectively a measure of free oxygen, meaning network forming oxides such as SiO_2 reduce basicity whereas network breaking oxides such as CaO increase basicity. The two selected examples are in fact the most influential and are thus combined to calculate the binary basicity ($\%CaO/\%SiO_2$), the quickest and most common way to understand how a slag is likely to behave during a process or reaction. With the likely high levels of FeO within the recovered BOF slag, there is significant potential for internal recycling as an additive in the sintering process [10]. However due to its relatively low iron content compared to raw materials, recently there has been significant activity in its use as carbon sinks, road materials and water purification systems [11].

Hot gases are a further by-product of the BOF, with modern furnaces being equipped with air pollution control equipment able to contain and cool the gases. The gas is quenched and cooled using water and cleaned of suspended metals and other solids. The process produces air pollution control dust [10] and water treatment plant sludge [12].

Steel Production from Scrap

Steelmaking from scrap involves melting of scrap, removing impurities and casting into a desired shape. The EAF is often used, and melts with the use of electrical energy in the presence of oxygen. The process is a direct method to produce desired products (as opposed to the multiple steps required through the BF-BOF route) offering the potential to be economically viable on a much smaller scale. Frequently mills producing steel with EAF technology are referred to as mini-mills. In addition it is possible to utilise a portion of scrap within the BOF. The key reasons for doing so are temperature control and the fluctuation in raw material price on a global scale; whereas scrap prices are often dictated within smaller geographic regions due to oversupply and government preference through legislation for internal recycling.

2.2.4 Steel Forming and Finishing

After molten steel is released from either the BOF or EAF, it must be formed into its final shape and finished to prevent corrosion. Traditionally steel was poured into a conventional ingot and stored until a specific final product was required. However current practices favour continuous casting where the steel is poured directly into semi-finished shapes. Continuous casting saves time by: reducing the steps required to produce the desired shape; it increases length versatility of product; and lends itself well to the modern just-in-time manufacturing approach to production and acquisition.

After cooling within the mould further shaping is conducted through hot or cold forming. Hot forming consists of heated steel being passed between rollers until it reaches its desired thickness. The process lends itself to the production of slabs, strips, bars or plates from the steel.

Cold forming is used to produce wire, tube, sheet and strip. This process involves the steel being passed between rollers without being heated to reduce thickness. The steel is then heated in an annealing furnace to improve the ductile properties. Cold rolling is more time consuming, but is used because products taking this route have better mechanical properties, better machinability and can more easily be manipulated into challenging sizes and thinner gauges [8]. After rolling is completed the steel pieces are finished to prevent corrosion and improve properties of the metal [8] [13]).

2.3 The Basic Oxygen Furnace

As previously discussed the BOF serves as a refining vessel for hot metal produced in the BF. With the incorporation of a desulfurization pre-treatment before entering the BOF, the primary functions remaining are decarburization, dephosphorization and temperature adjustment [8].

Carbon content is around 4 wt% when hot metal enters the BOF, the majority of which is present due to the reducing process in the BF being conducted through addition of coke. With regards to phosphorus, the sources are from iron ore, coke during ironmaking and poor quality scrap input at the BOF stage. Under the reducing conditions within the BF all phosphorus entering the BF is carried over into the output hot metal.

The dephosphorization reaction is facilitated in several ways through oxygen steelmaking. Firstly the introduction of desulfurization pre-treatments reduces the competition for interfacial sites between liquid steel and slag, allowing phosphorus removal to begin at a high rate from early in the blow. With controlled oxygen partial pressure and lime introduction, the chemical pathway for dephosphorization is enabled through the oxidation of Fe to FeO and availability of Ca for inorganic complex formation [14] [15] such as in equation 2.1:

$$2CaO + 2PO_{2.5} = 2CaO.P_2O_5 \tag{2.1}$$

With a target liquid slag composition which maximizes the P partition at high binary basicity's (CaO/SiO_2) of 3-5, which varies as a result of incomplete lime dissolution and the extension of blow time past that needed for sufficient carbon removal (end blow period), the BOF presents a period of favourable environment with reduced competition for the dephosphorization reaction.

Problems with the existing practice are caused inherently by additional function requirements. Including: the removal of carbon; a competing reaction for available oxygen [16] (see equations 2.2 2.3); unfavourable high target temperature required for the material to stay liquid in transport to the casting operation [17]; and the converter size/batch mass which inhibits the controllability of micro conditions and predictive interface formation [18] [19].

$$[C] + (O_2) \rightarrow (CO_2) \tag{2.2}$$

$$(CO_2) + [C] \rightarrow 2(CO) \tag{2.3}$$

where material within () is in a gas phase and those within [] are in the liquid steel.

Within the BOF, there are several locations/zones where refining takes place. Initially the quiescent interface of the bulk bath-slag, being the simplest region, is now thought to be less significant in controlling phosphorus refining. Secondly the "hot zone" (the location where the steel bath surface is directly struck by the impinging oxygen jet) as a kinetically released hyper-reaction site due to high comparative temperatures and abundance of oxygen [20] [21] [22]. Finally the three phase gas/slag/metal emulsion presents a possibility of significant influence over the governing phosphorus removal rate due to the drastically larger interfacial area provided through the dispersion of metal droplets (in comparison to the quiescent interface). Figure 2.2 shows a schematic of phases and their locations within the BOF. The large slag to metal ratios in the area offers an increased and refreshing driving force through maintained chemical potentials in the micro environment [23].

S and P are both undesirable elements in the steel due to segregation to grain boundaries in subsequent processing of the steel, where several surface defects and in-application failures are associated with their overabundance. As previously stated phosphorus partition to the slag phase is favourable at lower liquidus temperatures and high oxygen potentials; however sulfur has a converse relationship, providing a

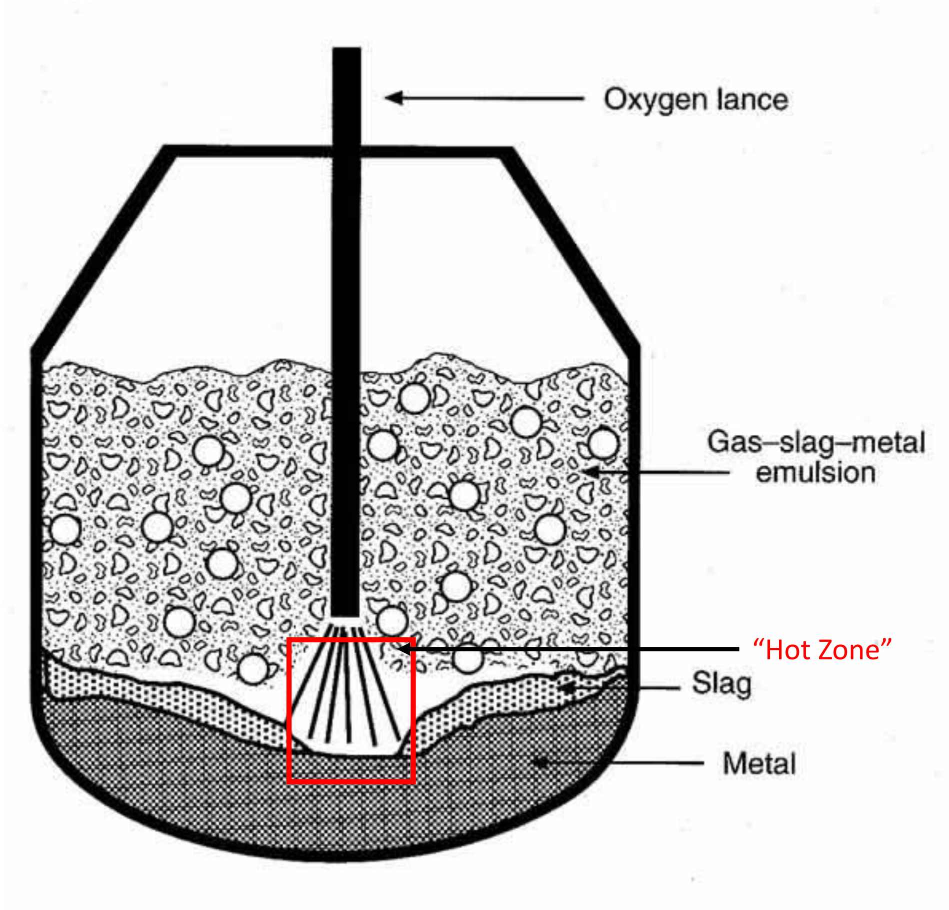

Figure 2.2: Schematic of the BOF, whith key phases/locations labled [24].

difficult if not near impossible situation to control both residual elements levels at the same time [2] [6] [25] [26] [27] [4].

2.3.1 Further Dephosphorization Technologies

Advanced converter-type hot metal pre-treatments for dephosphorization have been developed and are in use commonly in markets such as Japan and Korea to address the need for ultra-low P level in steel production. Since initial introduction in 1993, several technologies have been implemented.

An initial example is the Zero Slag Process (ZSP), based on desiliconization to below 0.1 wt% Si prior to dephosphorization. Each is conducted within a separate ladle station between BF output and prior to BOF loading. Via such a method there is claim that slag volume may be markedly reduced and iron yield increased [13].

Two methods implemented within de-P stations are the ladle-type dephosphorization process (NRP) and the LD-Converter-Type-Dephosphorization process (LD-NRP). In each process calcium requirement is much less as low silicon levels are present; $CaO.P_2O_5$ may form in preference to $CaO.SiO_2$ at low temperatures favourable for efficient de-P. The LD converters perform decarburization followed by dephosphorization. The average phosphorus content after such treatment is less than 0.012 wt%. Although these processes are considerably innovative, the capital cost in addition to the increase in processing times are major constraints of the processes which inhibit international acceptance and application.

LD converter optimized process (LD-ORP) is an example of technology which uses two double converter operations. This breaks down into desiliconization and dephosphorization coupled removal in one converter followed by decarburization in a second vessel. In multi refining converter processes (MURC) the hot metal is dephosphorized and decarburized sequentially in the same converter separated through de-slagging (slag discharging by tilting the converter) [13]. The advantages of such a process over conventional hot metal pre-treatment in a torpedo ladle or molten metal ladles is the improved productivity through high oxygen potentials (due to direct high speed oxygen blowing), low slag basicities (dropping the slag volume) and the low temperatures all favourable to dephosphorization. The MURC process does not require a pre-desiliconization step or a change in vessel; while offering the ability to reuse the rich carbon treatment slag (high in FeO) for dephosphorization in the following charge. Such considerations promote the use of MURC processing over LD-ORP. The introduction of slag replacement systems such as the MURC process, notwithstanding its advantages, causes a relatively large increase in requirements of lime provision, flux and other slag components; as such there is a greater waste output [2] [13].

2.4 Phosphorus reaction: Thermodynamics and Kinetics

The thermodynamics and kinetics of phosphorus reactions are important aspects to consider towards understanding of phosphorus behaviour in the steelmaking processes.

Steelmaking oxygen partial pressures favour the stability of phosphorus in the slags as phosphate ions (PO_4^{3-}) [28]. As such, the phosphorus oxidation follows the following ionic reaction:

$$\underline{P} + 2.5(FeO) + 1.5(O^{2-}) = (PO_4^{3-}) + 2.5\underline{Fe} \tag{2.4}$$

The equilibrium constant of equation 2.4 can be defined as [29]:

$$K = \frac{\mathrm{a}_{PO_4^{3-}}}{a_P\ a_{FeO}^{5/2}\ a_{O^{2-}}^{3/2}} = C\frac{(\%P)\gamma_{PO_4^{3-}}}{[\%P](T.Fe)^{5/2}\gamma_{FeO}^{5/2}a_{O^{2-}}^{3/2}} \tag{2.5}$$

The phosphorus partition ratio has long been used as a criterion to evaluate the slag's capability to remove phosphorus from the melt; it is usually defined as:

$$L_P = \frac{(\%P)}{[\%P]} \tag{2.6}$$

Researchers have interchangeably expressed the capacity of a slag to contain phosphorus by apparent phosphorus partition, defined in equation 2.7

$$L_P = \frac{(L_P)}{(T.Fe)^{5/2}} \tag{2.7}$$

The logarithmic of apparent phosphorus partition has been expressed as a function of slag composition, and temperature using multiple regression analysis of controlled equilibrium experimental data, for example [29] [30]:

$$\begin{aligned}\log(\frac{L_P}{Fe_t^{2.5}}) = 0.06[(\%CaO) + 0.37(\%MgO) + 4.65(\%P_2O_5) - 0.05(\%Al_2O3)\\ - 0.2(\%SiO_2)] + \frac{11570}{T} - 10.52\end{aligned} \tag{2.8}$$

In the above equations: The underlined/square brackets represent the content in the metal, while the parentheses denote the content in the slag

a_i : Activity of component i in the metal or slag

γ_i : Activity coefficient of component$i$

$T.Fe$: Total iron in the slag

C : Term, which includes the conversion factors

At low concentrations of phosphorus, and oxygen, as in most of the experimental melts, the phosphorus activity coefficient is close to unity; therefore mass concentrations have been used in formulating the equilibrium constant in the above reaction. From the exothermic phosphorus reaction; the reaction is proceeding to the right, and would achieve relatively high phosphorus partition when satisfying conditions including; high amounts of lime (CaO) in the slag (oxygen anions), high oxygen content in the slag (FeO activity) and low activity of phosphate ions. Accordingly, high lime, and comparative lower temperatures are favourable for the dephosphorization reaction.

Phosphorus partition in the BOF is not at predicted equilibrium for the conditions, and intrinsically kinetics must be considered [22]. This non-equilibrium is primarily caused by the kinetic conditions in the steelmaking operation where fluxes, oxygen, and carbon addition take place continuously or in batches at different stages of the melt-process, semi-continuous slag flushing, and the resultant temperature changes [31] [15] [32].

The rate of the dephosphorization reaction consists of a series of kinetic steps as follows:

1. Phosphorus transfers from bulk steel to slag/steel interface
2. Oxygen ions transfer from bulk slag to slag/steel interface
3. Chemical reaction at slag/steel interface
4. Oxygen transfers from slag/steel interface to bulk steel
5. Phosphate ions transfer from slag/steel interface to bulk slag

Figure 2.3 gives a schematic representation of these steps.

The chemical reaction at the interface is known to be relatively quick under operating conditions and therefore is not the rate-limiting step. The rate is hence thought to be predominantly controlled by the mass transfer of phosphorus in the metal phase, slag phase, or mixed controlled. The metal-slag reaction in the BOF involves not only flat area reactions, but also 3-14 times that area due to emulsification behaviour caused by metal droplets in the slag. As a result within the BOF much work has been carried out into the study of droplet refining in the emulsion area of the converter [17] [33] [34] [35] [36].

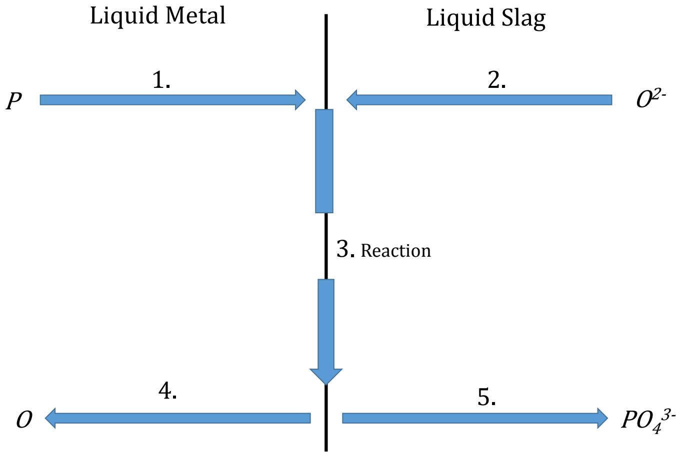

Figure 2.3: The kinetic steps required for phosphorus removal from liquid steel.

2.5 The Interfacial Area of reaction within the Emulsion

2.5.1 Droplet Size Distribution

The metal phase within the BOF slag/gas/metal emulsion has been quantitatively investigated by only a few researchers on an industrial or laboratory scale. These investigations have focused primarily on identifying the size distribution of the metal droplets, weight percentage and surface area at various stages of blow or under controlled laboratory conditions.

The investigation by Meyer [37] of metal droplet size distribution was conducted using a 230 ton BOS converter. Material which was ejected through the converter tap hole was rapidly cooled on large steel pans positioned outside the vessel. The size distribution was then measured using sieving technology after the emulsion material had undergone crushing, screening and magnetic profiles to separate the metal phase from the slag material. Droplet size ranged between 14-100 mesh and the emulsion was reported to contain up to 80% metal material by weight at a particular blow period; however some of the droplets exhibited features such as cavities caused by CO nucleation within the droplets. Skewing of droplet size distribution towards finer sizes is also discussed due to fracturing of larger droplets during the physical breakup procedures.

A further study conducted by Cicutti et al [23] focused on slag-metal reactions in an LD-LBE converter. Samples of the gas/slag/metal emulsion were collected simultaneously from a 200 ton converter during full operation using a uniquely designed lance; the lance allowed for sampling during process and at different times of the blow. From the separation and post analysis of the metal fraction within the collected emulsion samples it was found droplet sizes ranged from 230 - 335 μm. In addition to this the droplet size distribution agrees well with the Rosin-Rammler-Sperling (RRS) function, given in equation 2.9:

$$R = 100exp[-(\frac{d}{d'})^n]\% \tag{2.9}$$

where R is the cumulative weight of droplets retained in the sieve (%), d is the upper limit of class diameter in a given class (μm), d' is the size parameter - mean particle size (dimensionless) and n the distribution parameter - measure of spread of particle sizes (dimensionless).

As with Meyer [37], Cicutti [23] reported droplets being more decarburized than the metal within the bulk bath at a given time. Further to this droplets of smaller sizes had progressed further through decarburization than large droplets, and overall the direct decarburization of metal droplets within the emulsion was proposed as a significant factor contributing to the global decarburization performance with the BOF.

Millman et al [4] investigated the processing events with a 6 ton BOF pilot plant converter with specific emphasis on the phosphorus behaviour during the blow. Samples of the emulsion, slag and bulk metal bath were simultaneously collected at 2 minute intervals during an average blow time of 16 minutes. Emulsion samples for two heats were microscopically analysed to produce size distributions of the emulsion metal droplets and voids. Independent of blow time and measured across a limited size range of 0 - 400 μm, the majority of droplets possessed a diameter below 100 μm. In addition CFD modelling was employed to simulated droplet generation and the reported findings from both modelling and experimental avenues had significant correlation for the lower emulsion levels, while the model over-predicted size distribution at higher levels within the converter.

Price [38] conducted studies on the significance of the emulsion in carbon removal through sampling an industrial working BOF using an 'in-blow bomb' capable of collecting slag and emulsion samples simultaneously. The predominant size range of droplets within the emulsion was found to be 100 - 2000 μm; although it was noted that agglomeration of droplets on the sampler support chain may have affected the credibility of reported droplet size distributions.

Block [39] and Urqhuart [40] collected samples from inside the reaction area with the former using a specially designed lance to sample the emulsion phase. Tokovoi [41] sampled the slag/metal emulsion by collecting droplets from the upper layer. Resch [42] and Baptizmanskii et al [43] also sampled the emulsion; Resch [42]) by tilting the reaction vessel and Baptoizmanskii [43] by cutting a hole in the crucible.

Lange and Koria [44] sampled oxidised drops by using a combination of high speed filming (viewing the impingement area of the oxygen jet) and collecting splashed emulsion samples from the top of a converter. Smaller droplets were spherical whereas larger droplets (those $<$2000 μm) appeared to have flattened. Droplet size distribution was again found to obey the RRS distribution function. Droplet size ranged between 500 and 5000 μm diameter mostly, however larger droplets up to 70,000 μm were also found. The conclusions drawn were larger droplets (those $<$2000 μm) decarburized less because of their inherent smaller surface area to volume ratio and lower emulsion residence time.

Koria and Lange [45] further experimentally investigated the disintegration of 5% FeC droplets falling vertically through a high-velocity jet. Results showed that after fragmentation by the high-velocity jet into secondary droplets, further breakup does not occur; a finding which led the authors to conclude droplet size distribution is solely a characteristic of the Weber number. In further studies the authors discuss the insignificance of initial droplet diameter on the final droplet size distribution [46].

Nordquist et al [47] conducted metal droplet size distribution experiments within a 30 kg induction furnace. Analysis of emulsion samples by electron probe microanalysis technique showed the majority of metal droplets had a diameter of 360 μm or less and were predominantly spherically shaped. Droplets sizes were recorded through spacial detection of iron intensity.

2.5.2 Droplet Generation

A gas jet impinging on a liquid surface causes depression of the surface due to the momentum of the gas jet. The deflected gas flowing along the depressed surface exerts a shear force on the liquid surface and drives liquid flow. When jet momentum is very slow there is no droplet formation on the surface as the dense phase has a tendency of self-adjustment to keep the force balance. If the gas flow rate is increased, droplets will be generated at the edge of the depression. There are two factors which dominate the generation of droplets: an external factor which is the momentum intensity of the gas jet; an internal factor which involves the properties of the liquid from which droplets are ejected. These include viscosity and surface tension. Noticing the Weber number is built upon similar principles He and Standish [48] used it to describe droplet generation rate. The Weber number is expressed in equation 2.10

$$We = \frac{\rho_g u_g^2}{(\rho_l g \sigma)^{1/2}} \tag{2.10}$$

where We is the nominal Weber number and represents a ratio of inertia forces to the square root of surface tension and buoyancy forces; u_g the jet velocity; ρ_g and ρ_l: densities of gas and liquid respectively and σ is the surface tension of the liquid.

He and Standish [48] along with Li and Hondros [49] predicted the onset of splashing according to the Kelvin-Helmholtz instability criterion. The splashing occurs when $\frac{\rho_g u_g^2}{2\sqrt{\rho_l g \sigma}} = 1$. The physical meaning of the left hand term is how many times the critical Kelvin-Helmholtz instability criterion is exceeded based on observation. Subagyo et al [50], named the dimensionless parameter NB as the blowing number, which is used to describe the metal droplet generation where $NB = \frac{\rho_g u_g^2}{2\sqrt{\rho_l g \sigma}}$.

Further to this Subagyo et al [50] derived the following empirical correlation (equation 2.11) using an asymptotic solution approach when droplet generation rate is plotted as a function of blowing number:

$$\frac{RB}{RG} = \frac{(NB)^{3.2}}{[2.6x10^6 + 2.0x10^{-4(NB)^{12}}]^{0.2}} \tag{2.11}$$

where RG is the volumetric flow of blown gas in normal m^3s^{-1}, and RB is the droplet generation rate.

2.5.3 Residence Time

Discrepancies exist regarding the residence time of metal droplets within the BOF emulsion. The reported times range anywhere from 0.25 s to 120 s. Price [38] estimated a value of 2 minutes ± 0.5 minutes through use of a radioactive gold isotope tracer technique in an industrial-scale converter. Kozakevitch [51] argues the length of time a droplet is present in the emulsion to be likely less than 1.5 minutes whereas Urquhart et al [40] observed the residence time to be around 0.25 seconds during the room temperature experiments conducted. Considering the large discrepancies between experimental efforts, Subagyo [50] developed a mathematical model to predict residence time of metal droplets in the emulsion phase. The underlying principles of this were those of an accelerated moving body in a flowing fluid. The model was unsuccessful as there was no account for chemical reaction between the phases. Brooks et al [52] developed this initial work to successfully predict residence times under varying conditions. The residence time was found to be less than 1 second without the consideration of droplet swelling, however when swelling of the droplet (due to decarburization) in addition to the formation of a gas halo is considered, the residence time could be prolonged to more than 60 seconds. The swollen droplets have less density reducing the momentum to push through the foaming slag or resist turbulence within the layer further extending the residence time [32] [52] [50] [53] [54] [55] [56] [57].

2.5.4 Spontaneous Emulsification

Definition of an emulsion: “An emulsion is a mixture of two or more liquids that are usually immiscible”. Emulsions are used in every day life, such as oil droplets suspended in water within milk, ice cream and mayonnaise; or water droplets suspended in oil within butter, margarine and moisturising lotions.

When two immiscible liquids are at thermodynamic equilibrium, the interfacial area and free energy of the system are at a minimum. If this is the case, in order to promote emulsification there is a requirement for the supply of energy and the system to be away from thermodynamic stability. If two immiscible liquids are not initially at equilibrium and brought into contact spontaneous emulsification can be promoted by dynamic interfacial phenomena caused by temporary instabilities (for example concentration gradient, thermal gradient or electrochemical potentials), with no requirement for external stirring.

Spontaneous emulsification was first observed in 1870 and has been a present topic in organic and biological system investigation [31] [58]. The phenomenon however has implicit kinetic impacts in steelmaking, where the refining of impurities from liquid metal to slag relies on high interfacial area such as that provided through the formation of slag/gas/metal emulsion in the BOF [59].

A variety of authors [60] [61] [62] have assumed that during a period of intense mass transfer of elements such as oxygen and sulfur (surface active species), spontaneous emulsification can occur due to a pronounced reduction in the interfacial tension between metal and slag phases. The kinetic importance of this behaviour is beneficial to refining conditions, as a temporary increase in interfacial area is possible thus increasing the rate of a given chemical reaction. Quantification of this phenomenon is uncommon due to the intrinsic difficulties of high temperature experimentation.

The recent investigations by Rhamdhani et al [63] [64] [65] provide an example of the few studies which have attempted to quantify how the interfacial area of the metal/slag system may change as a given chemical reaction is ongoing between the two phases. The work involved the investigation of $FeAl$ droplets immersed in $CaO - SiO_2 - Al_2O_3$ slags. The interfacial area of the metal droplets recovered after experiments were measured using callipers for regular shaped droplets and the overlay of known paper sizes to cover irregular droplet shapes. They observed that the total interfacial area was a function of the initial reaction rate and could increase by of a factor of 4.

Other studies have investigated the phenomena of Fe alloys in slags usually by either direct observation or 2D X-ray images [35] [66]. These studies observed that if the initial driving force of a reaction is high enough the interfacial tension between slag and metal decreased rapidly and the droplet may wet the slag. Gaye et al [67] estimated that oxygen flux across the interface may cause interfacial tension to approach a value close to zero if a rate of 0.1g atom $m^3 s^{-1}$ is achieved. As the chemical reaction slows the interfacial tension increases to values seen at equilibrium conditions and droplets become spherical [56] [68].

Understanding the behaviour of metal droplets immersed in slag during steelmaking is critical for better consideration of the kinetic conditions which inhibit a thermodynamic equilibrium (specifically the partitioning of phosphorus to the slag phase to a thermodynamically predicted level). Spontaneous emulsification may occur when rapid mass transfer of oxygen takes place at the interface between slag and metal systems, however this is yet to be confirmed as all previous work has been conducted under non-equilibrium conditions. The theory results in a substantial decrease in interfacial tension, thus increasing the reaction area and the reaction overall rate. To date no direct calculation of reaction area change due to interfacial phenomena has been possible.

Previous studies have used metal droplets in the range of a few grams which results in droplet sizes of several millimetres. However Koria et al [46] along with recent findings by Millman et al [69] allude to the presence of metal droplets produced in oxygen steelmaking to be a few tens or several hundred micrometres in size. The size of metal droplets can drastically influence the behaviour and resulting transient interfacial area.

2.6 Unresolved Findings from the Literature

1. During BOF processing the amount of metal material in the emulsion and how long it stays there is of significant importance to the refining performance achieved. Previous studies have made use of industrial and laboratory experimentation, as well as modelling approaches. However there is a lack of cohesive understanding due to poor sampling techniques and biased data acquisition due to the manual nature of sampling location and the need to pause processing with industrial studies.

2. Metal droplet size within the BOF emulsion has seen significant interest in the literature. However there is yet to be a study which combines both in-situ sampling of a working BOF and undeniable analysis of resulting droplets collected.

3. Interfacial phenomena has received significant attention within the steelmaking community, however there have been multiple factors in play during experimental studies. In addition laboratory studies have found it difficult to replicate the unbound environment of a metal droplet as is the case within the suspended emulsion phase of the BOF.

4. Effects of residuals other than oxygen and sulfur have seen little attention with relation to interfacial phenomena. Specifically phosphorus is of interest due to the potential increase in abundance in the supply chain, and need to further reduce levels as the industry evolves.

5. The physical pathway of spontaneous emulsification is yet unknown. Slow or interrupted trials of emulsification have been the menu of the past and as a result droplets have seen little attention while in the process of undergoing emulsification.

6. Finally the prediction and energy required for spontaneous emulsification to occur in metal/metal-oxides system is yet unknown. Previous efforts have been unable to track or explain the phenomena in a quantifiable manner suitable for implementation in process control models.

Chapter 3

Formulating the Research Approach

This chapter focuses the project through a hypothesis driven approach. The key gaps in the literature along with the drive of industrial influence are considered in drawing hypotheses for exploration, followed by a plan of exploration for each targeted question.

3.1 Hypotheses

3.1.1 Hypothesis 1

"Periods of greater dephosphorization in the BOF correspond to times of greater interfacial area between slag and metal."

To tackle this hypothesis IMPHOS trial data will be used in order to investigate contributing factors to the size of the interface. This will include the mass of metal ejected into the emulsification, the period of time metal is in contact with slag and the rate at which the droplet environment is changing. As well as this, control parameters such as lance height, temperature and blowing volume will be discussed. This hypothesis has direct industrial relevance as findings will be trackable against process control via the extensive IMPHOS trial parameter recordings.

3.1.2 Hypothesis 2

“The use of in-situ sampling and 3D volumetric analysis of droplet sizes produced within the BOF will offer updated, more accurate results than previous methods.”

This hypothesis tackles the ability to conduct research using new techniques which may either reinforce or improve on previous findings. Previous methods have involved either sampling in a reduced capacity such as outside of the BOF, or intermittent with blowing; otherwise 2D analysis of droplet size such as sectioning an emulsion sample and conducting optical analysis has been the norm. Therefore previous results may be affected due to coalescence of droplets, selective retention of specific droplet size fractions or measurement of unknown representations of droplet diameter. The use of in-situ samples taken from the BOF in IMPHOS trials, and 3D XCT analysis of the recovered samples aims to provide a true representation of droplet size.

3.1.3 Hypothesis 3

“Spontaneous emulsification is a result of material transfer across the metal slag interface, causing a drop in interfacial tension. This causes an overall increased rate of free energy reduction, physically expressed by the production of an increased surface area.”

Hypothesis 3 is essential for the continued study of metal slag interfaces. A matrix of experiments will be conducted in order to validate CSLM testing of this phenomenon as well as providing a bench mark for parameter comparison. Primarily the proof of ion transfer across the membrane being the cause, rather than monolayer enrichment or electrochemical effects at the interface, will be determined.

3.1.4 Hypothesis 4

“Factors that are known to affect the rate of dephosphorization also promote spontaneous emulsification.”

As dephosphorization of iron by slag is an interface dependent process, it is reasonable to assume that at rates of higher dephosphorization there is potential for a greater interfacial area. A contributing factor to interfacial area change is expected to manifest as emulsification of droplets in environments similar to the slag-metal-gas emulsion present in the basic oxygen furnace.

3.1.5 Hypothesis 5

“Spontaneous emulsification is initiated by perturbation and the potential this creates for reducing diffusion distance.”

Liquid interfaces are known to perturb. As such the produced heterogeneous morphology of the interface creates an environment where the potential for transfer of material across the interface is non-uniform. Impurity refinement in high temperature systems is reportedly often restricted by mass transfer of material in either bulk phase; the growth of a perturbation has the potential to remove or reduce this kinetic restriction, drastically increasing the rate of free energy dissipation.

3.1.6 Hypothesis 6

“Spontaneous emulsification can be predicted from fundamental knowledge of the system.”

Spontaneous emulsification is driven through the refining of material, and the extent to which the two phases aid or resist intermixing. If variables such as diffusion rates, viscosities and interfacial tension are known, the likelihood and extent of emulsification should be predicable via an appropriate method.

3.1.7 Hypothesis 7

“Within a given system there is a critical point at which the spontaneous emulsification will begin to occur with respect to starting material composition.”

If spontaneous emulsification is driven by the transfer of material across the interface of metal and slag, then there should be a critical inflection of behaviour where the phenomenon does and does not occur. As such there should be energetic accountability for the relief of increased global interfacial tension between the two systems.

3.2 Hypothesis Approach

3.2.1 Hypothesis 1

Previous work [4] carried out by Tata Steel Europe scientists will be examined, progressed and developed. This will involve combining quantitative data from the

IMPHOS trials with statistical representations for the full converter. The calculation will not only provide experimentally deduced macroscopic conditions within the BOF, but will also allow validation of assumptions and conceptions of how BOF refining takes place, as well as which factors have the greatest influence on refining.

3.2.2 Hypothesis 2

To explore this hypothesis, the solid emulsion samples taken from IMPHOS trials will be examined via XCT, in order to gain a more accurate representation of this converter's droplet size. This will be compared to size of droplets formed by interfacial emulsification and physical separation forces, similar to those seen in the BOF. A comparison of findings should show if the previous methods of analysing this situation have been successful, or if the reported findings are a product of the sampling and analysis techniques used.

3.2.3 Hypothesis 3 & 4

The cause of spontaneous emulsification will be approached via a rigorous method where base-line experimentation will be conducted, showing replication of the literature findings, and validation of the experimental technique being used. From this base line, the cause of emulsification in BOF systems will be evaluated through the introduction of compositions which thermodynamically favour interfacial exchange, such as phosphorus and oxygen transfer.

3.2.4 Hypothesis 5

Use of an $FeAl{-}SiO_2$ reactive system will enable the investigation of this hypothesis. An oxide phase lacking in transition metals will give an optically transparent medium for viewing of the reactive metal droplet using HT-CSLM. Further to this XCT of quenched droplets which have undergone differing hold times in the HT-CSLM will undergo high-resolution XCT. This will allow for tracking of the emulsification pathway, and quantification of perturbation growth as the reaction progresses.

3.2.5 Hypothesis 6

Phase-field modelling will be employed to track the evolution of the interface in 2D and 3D for known emulsifying systems. Phase-field works on the premise of a defined interface boundary; ideal for tracking its movement in space and time. Modelling of the same systems investigated experimentally will allow for conversion from Fourier time and space, to Cartesian space and relative times of reaction. The ability to make this comparison will allow for cross interrogation of results to verify that the driving forces within the model are similar to those in the physical systems.

3.2.6 Hypothesis 7

Variable initial alloy composition of 8, 5, 4, 3, 2, 1 and 0wt% aluminium in iron will be used to observe interfacial phenomena in-situ. The development of automated HT-CSLM and post-process image analysis will allow for quantification of observed perturbation, necking and spontaneous emulsification levels. In addition an attempt to verify any changes in behaviour via a free energy dissipation balance will be investigated.

Chapter 4

Experimental Methods

The present work consists of three distinct experimental ventures:

1. Sequential inline sampling of a 6 ton pilot plant BOF.
2. The coupling of HT-CSLM, XCT and phase-field simulation
3. Post processing analytical techniques

4.1 Pilot Plant Based Experiments

The results chapter entitled “Calculating the macroscopic dynamics of the Gas/Metal/Slag Emulsion during steelmaking” builds on the initial findings of the European Commission funded project “IMPHOS: Improved Phosphorus Refining”.

The groundings of the experiment are the sequential sampling of a 6 ton BOF at the MEFOS site in Sweden. A robotic carousel was used to deliver a 7 height sampling lance to the converter roughly two minutes apart through 24 blows.

The samples can be split into groups, where level 1 consists of bulk bath material, 2 and 3 are at the interface level between the bulk steel bath and emulsion phase, and 4-7 are at increasing height within the emulsion phase.

For the investigations in this work, chemical analysis of steel and slag phases was required, along with time dependent off-gas composition and mass fraction of each phase within a single sample.

In addition, unprocessed emulsion samples were used to briefly touch on the droplet sizes within the emulsion phase; the data from which is used to give rudimental validation to an assumption within the investigation of percentage contribution to decarburization of each zone within the BOF.

Further details of this programme of experimentation are presented within the relevant results chapter.

4.2 High-Temperature Confocal Scanning Laser Microscopy

The HT-CSLM is a key tool used for the development of the presented results. The equipment itself is depicted in figure 4.1. The main body consists of an elliptical gold-coated chamber with a halogen bulb positioned in the lower focal point, and the sample positioned in the upper focal point. The sample is held in place through the extension of an alumina rod from the side of the chamber, through which an R-type thermocouple is threaded, and subsequently fused to the underside of a platinum ring positioned at the free end of the alumina rod. It is on this ring that the sample is placed. IR radiation produced from the halogen bulb is then reflected from the chamber walls and focused onto the sample. This results in possible heating rates of up to 700 K min^{-1} and temperatures up to 1973 K.

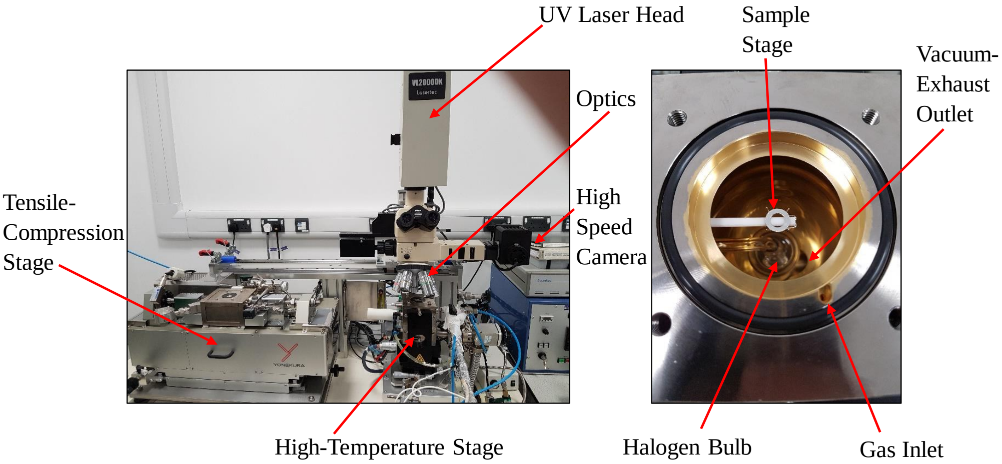

Figure 4.1: The High-Temperature Confocal Scanning Laser Microscope. a) Shows a broader image of the instrument complete with both the high-temperature and tensile/compression stage. b) Shows the interior of the high temperature chamber.

The instrument is equipped with a rotary vacuum pump and a high-purity argon gas feed (99.9999% purity) supply which is subsequently passed through a further system of cold zirconium based getters, filters, drying chambers and a heated getter at 623 K containing copper and magnesium turnings. This results in a consistent oxygen level <2 ppb. The instrument is also linked to a switched helium source for quenching, enabling cooling rates at steel/slag solidification temperatures of 3000 K min^{-1}.

Above the heating chamber there is a UV laser positioned with pin hole focusing apertures. The UV laser is used so that the IR radiation from both the bulb and heated sample do not interfere with the image produced. The laser can be controlled both manually and automatically through use of a third-party program. This allows for reactive imaging in relation to the ongoing observations of a study being carried out, as well as a predetermined focusing regime which will allow for tracking of the horizontal plane within the sample being viewed. As a result it is possible to assess surface topologies of a sample, as well as tracking a system moving in the z-direction.

The nature of the confocal optics allows for high resolution in the z-direction imaging plane. For the in-situ spontaneous emulsification observations in the chapter entitled “Spontaneous Emulsification as a Function of Material Exchange” it was necessary to follow the droplet with accuracy to enable quantification of surface area. As a result both the z-focal positioning and aperture of the laser were rastered to enable a greater depth of field, but also the accurate imaging of a 2D plane within the sample. The video capture and temperature programming is controlled through the HiTOS software package.

The individual experimental set-ups for each experiment are described within the relevant chapters.

4.3 X-ray Computed Tomography

XCT has been used for medical purposes for a reasonable period of time now; however the last 25 years has seen the technique find application in industrial metrology for non-destructive testing and measurement. Full 3D evaluation of objects with no physical modification or destruction to the original part is possible.

The machines used in this study consist of an X-ray cone beam source and detector positioned at either side of a rotational stage upon which the object for inspection is placed as shown in figure 4.2. The source produces X-rays which pass through the sample, resulting in an image produced on the detector screen. Locations where a higher number of X-rays have been attenuated by the object appear as a darker patch on the results screen. As the object is rotated a large number of images are taken, and using a method of Feldkamp back projection the object is reconstructed as a series of 3D pixels known as voxels. Dependent on the number of attenuated X-rays at the relative position in each projected image, each voxel will have an associated grey scale. The calculated voxel size is dependent on the magnification of the object. The reconstruction can further be exported for analysis.

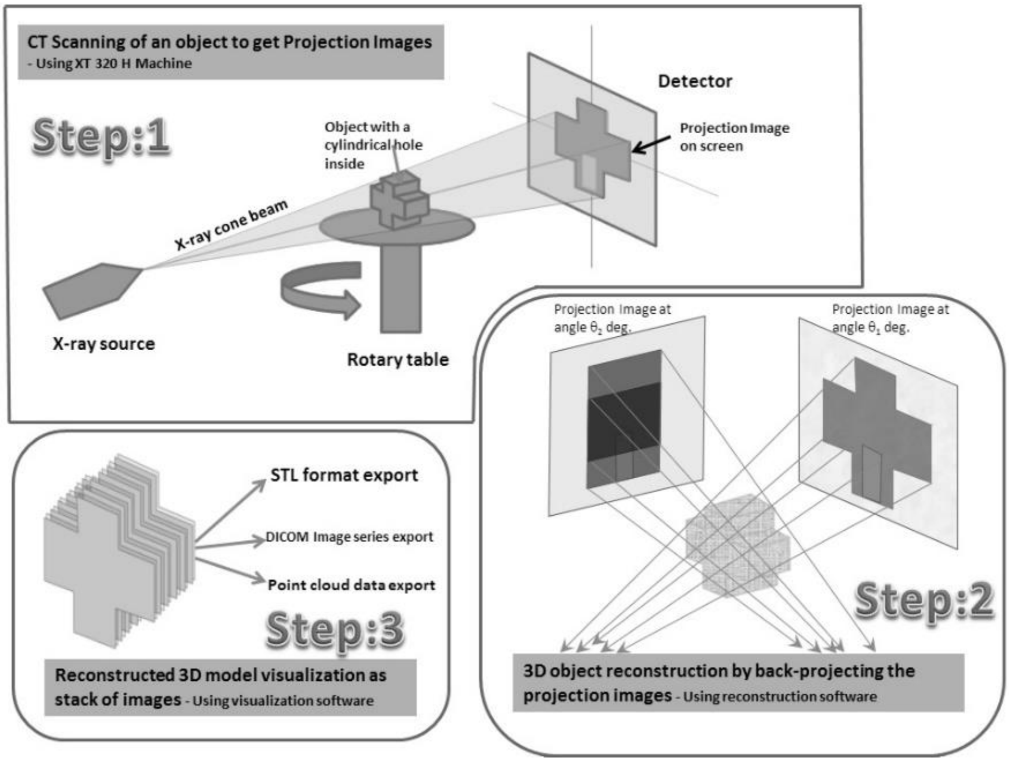

Figure 4.2: A schematic representation of image formation in the XCT process [62].

Optimal X-ray parameters are determined by the operator. The magnification is first set while containing the entire object within the field of view. X-ray settings are then selected to ensure the maximal use of grey-scale range, while also preventing the saturation of the signal. Objects which contain metal components require some filtering at the source to ‘harden’ the beam, blocking lower energy X-rays which would create artefacts in the scan due to high levels of scattering.

Further details on individual scanning conditions and parameters are reported within the relevant results chapters.

XCT scanning and subsequent 3D volume analysis for the current reportings were carried out by Dr Jason Warnett.

4.4 Phase-Field Simulation

To model the droplet behaviour in the experimental emulsification systems, the dual effects of non-Newtonian rheology and the moving interface had to be considered.

Navier-Stokes equations were employed to model the unsteady, viscous, incompressible and immiscible two-fluid systems in two- and three-dimensional space:

$$\rho_i(\frac{\delta u_i}{\delta t} + u_i.\nabla u_i) = -\nabla p_i + \nabla.[\eta_i(\nabla u_i + \nabla u_i^T)] + \boldsymbol{SF} \quad in\ \Omega_i \tag{4.1}$$

and

$$\nabla.U_i = 0 \quad in\ \Omega_i \tag{4.2}$$

where $\rho_i(x,t)$ refers to the density, $u_i(X,t) = (u_1(x,t), u_2(x,t), u_3(x,t))$ denotes velocity, $\rho_i(X,t)$ and $\eta_i(X,t)$ are the pressure and viscosity of fluids $i = 1, 2$, respectively. The transcript T refers to transpose and Ω represents the domain of each fluid. $\boldsymbol{SF}$ represents surface tension force. Normally this surface tension is considered a singular force and is defined as $\boldsymbol{SF}_{sing} = -\sigma\kappa\Gamma n$ where σ is the surface tension coefficient and κ is the mean curvature of the interface [62] and δ_Γ is the surface delta function [70]. In order to make the mathematical definition of surface tension compatible with the phase-field formalism, a regular $\boldsymbol{SF}$ force was employed. It is then possible to implement the Laplace-Young calculation [71] at the exact interface boundary using a continuum surface force. This converts the surface tension jump condition across the interface into an equivalent volume force to which the Navier-Stokes equations are added. Thus $\boldsymbol{SF}$ is defined as:

$$\boldsymbol{SF} = 6\sqrt{2}\varepsilon\sigma\nabla.(|\nabla c|^2 I - \nabla c \otimes \nabla c) \tag{4.3}$$

where ε is the gradient coefficient, c is the composition, I is the identity matrix and $(\nabla c \otimes \nabla c)_{ij} = \frac{\delta c}{\delta x_i}\frac{\delta c}{\delta x_j}$ is the usual tensor product.

Density and viscosity are defined as linear functions of the phase-field [72] and harmonic interpolation and linear interpolation for the density and viscosity are used respectively:

$$\frac{1}{\rho(\phi)} = \frac{1+\phi}{2\rho_1} + \frac{1-\phi}{2\rho_2} \tag{4.4}$$

$$\eta(\phi) = \frac{1+\phi}{2}\eta_1 + \frac{1-\phi}{2}\eta_2 \tag{4.5}$$

where ϕ is the phase-field variable and is defined as $\phi = \frac{m_1-m_2}{m_1+m_2}$,where m_1 and m_2 refer to the masses of fluids 1 and 2. Harmonic interpolation is employed because the solution of the Cahn-Hilliard equation does not satisfy the maximal principle [70]. Linear interpolation cannot be bound away from zero, while the harmonic interpolation results in the desired properties due to the L^{∞}-bound of the solution [71]. An advective Cahn-Hilliard equation is introduced as the governing equation for the phase-field:

$$\phi + u.\nabla\phi = \nabla.(M(\phi)\nabla\mu) \tag{4.6}$$

$$\mu = F'(\phi) - \varepsilon^2\Delta\phi \tag{4.7}$$

where μ is the bulk velocity and $M(\phi) = 1-\phi 2$ denotes the phase-field non-negative mobility [72]. $F(\phi)$ is the double well potential of a unit volume of homogenous material of composition ϕ. To derive the Cahn-Hilliard equation with variable mobility the chemical potential μ is added as the vibrational derivative of Ginzburg-Landau free energy, $\mu := \delta G/\delta\phi = F'(\phi) - \varepsilon^2\Delta\phi$ which defines the flux as ${}_T := -M(\phi)\nabla\mu$. As a result of mass conservation $\delta\phi/\delta t = -\nabla._T$. The natural and no-flux boundary conditions used are:

$$\frac{\delta\phi}{\delta n} = \nabla\phi.n = 0 \tag{4.8}$$

and

$${}_T.n = 0 on\delta\Omega \tag{4.9}$$

where n is a unit normal vector to $\delta\Omega$. The parameters used in this study were taken from the literature [73] [74] [75]. A semi-Implicit-Fourier-Spectral-Method [76] is then used for numerical analysis with a periodical boundary condition. The system size for the simulation is $300\Delta x$ X $300\Delta x$ X $300\Delta x$ for the 2D and $1000\Delta x$ X $1000\Delta x$ X $1000\Delta x$ for the 3D simulation. The method is programmed using C++ and the output is visualized using in-house visualization software (ARVisual) developed by our research group.

Dr Alireza Rahnama was responsible for formulating and coding the phase-field simulation.

4.5 Additional Analytical Techniques

4.5.1 Scanning Electron Microscopy (WDS and SIMS)

Scanning electron microscopy (SEM) is the bread and butter of materials characterization today. The technique was applied in the research for the clarification of the stock $Fe-P$ alloy. The SEM instrument used for this project was the Sigma-Zeiss model, a field-emission gun SEM (FEG-SEM). In addition to the imaging capability of the instrument, time of flight-secondary iron mass spectroscopy (TOF-SIMS), and wavelength dispersive spectroscopy (WDS) were used for the analysis of oxygen and phosphorus content respectively.

4.5.2 XRF, ICP and LA-ICPMS

X-ray Florescence (XRF) was used for chemical analysis of the synthetically produced slags. The model of equipment used in this project was the "Thermo Scientific ARL PERFORM'X Sequential 2.5kW XRF Spectrometer". A bead of slag is loaded into the sample holder in the XRF machine and the chamber is vacuumed and the sample ionized with X-rays. Analysis of fluorescent X-rays and their intensities were then compared against intensity profiles from certified calibration reference material, which had been prepared under the same conditions as the experimental samples. XRF OXSAS software was then used to calculate the average composition from 3 identical scans.

Inductively coupled plasma mass spectroscopy (ICP) was used to determine stock alloy compositions used in the HT-CSLM experiments in this study. For the instrument used in this project a portion of the sample is dissolved and then introduced to the plasma source through a spray chamber. The sample undergoes ionization from the plasma source and is then focused into a quadrupole region by single iron lenses. This focuses the beam of ions for chemical modification to eliminate interference. Once in the mass spectroscopy chamber, ions are separated via mass to charge ratios and picked up by the detector.

Laser ablation inductively coupled plasma mass spectrometry (LA-ICPMS) differs from traditional ICP in that a laser is used to directly ablate some of the sample surface which is then passed into the quadrupole/mass spectrometry detector series. This technique was used to confirm the data collected via WDS for some samples. LA-ICPMS is generally regarded as a very accurate chemical analysis technique.

4.6 Materials

Table 4.1 contains their heat number and starting “hot metal” composition for each IMPHOS heat used for calculating the macroscopic dynamics.

Table 4.1: IMPHOS heats and their starting “hot metal” compositions collected by spark optical emission spectrometry. [4].

Heat ID	$\%C$	$\%Si$	$\%Mn$	$\%P$	$\%S$
S1828	4.19	0.54	0.46	0.079	0.048
S1829	4.07	0.51	0.46	0.085	0.044
S1830	4.10	0.47	0.40	0.086	0.037
S1831	4.16	0.46	0.44	0.095	0.038
S1832	4.10	0.58	0.44	0.067	0.037
S1833	3.94	0.44	0.44	0.070	0.042
S1834	3.83	0.66	0.43	0.082	0.048
S1835	4.04	0.60	0.44	0.084	0.047
S1836	4.06	0.64	0.48	0.086	0.051
S1837	3.90	0.59	0.42	0.094	0.051
S1840	3.79	0.58	0.42	0.084	0.054
S1843	4.04	0.56	0.42	0.089	0.043
S1845	4.07	0.53	0.46	0.095	0.045
S1846	4.16	0.55	0.43	0.087	0.043

The compositions of alloys and slags used in HT-CSLM experiments are given in table 4.2 and 4.3 respectively.

Table 4.2: The compositions of all metallic alloys used in HT-CSLM experiments measured using ICP (where all N levels are <0.001%.

Alloy ID	$\%Mn$	$\%P$	$\%Ni$	$\%Cr$	$\%Al$	$\%C$	$\%S$	$\%O$
a1	0.011	0.201	0.003	0.002	0.002	0.0008	0.0012	0.0737
a2	0.0003	0.0004	0.0001	0.0003	0.0005	0.004	<0.001	0.0034
$Fe - FeO$	0.003	0.0004	0.0001	0.0003	0.0005	0.004	0.001	0.0034
Null	0.003	0.0004	0.0001	0.0003	0.0005	0.004	0.001	0.0034
$FeAl - SiO_2$	0.0002	0.0004	0.002	0.0005	7.87	0.0007	0.001	0.0038
0% Al	0.0003	0.0004	0.0001	0.0003	0.00005	0.004	0.001	0.0034
1% Al	0.0003	0.0004	0.002	0.0005	0.99	0.0011	0.001	0.0028
2% Al	0.0004	0.0004	0.001	0.0003	1.92	0.0006	0.001	0.0029
3% Al	0.0002	0.0004	0.002	0.0005	2.84	0.0011	0.002	0.0035
4% Al	0.0004	0.0004	0.002	0.0005	3.98	0.0007	0.002	0.0042
5% Al	0.0003	0.0003	0.002	0.0004	4.92	0.0009	0.002	0.0040
8% Al	0.0002	0.0004	0.002	0.0005	7.87	0.0007	0.001	0.0038

Table 4.3: The compositions of all slags used in HT-CSLM experiments measured using XRF.

Slag ID	$\%CaO$	$\%MgO$	$\%SiO_2$	$\%FeO_t$	$\%P_2O_5$	$\%CaO/SiO_2$	$\%Al_2O_3$
S1	36.64	7.08	16.98	33.56	1.66	2.16	0
S2	36.89	7.14	16.21	33.31	1.65	2.28	0
S3	38.15	10.26	16.89	34.70	0.01	2.26	0
S4	43.02	8.74	24.11	0	0	1.78	24.13
$Fe - FeO$	36.89	7.14	16.21	32.31	1.65	2.28	0
Null	43.02	8.74	24.11	0	0	1.78	24.13
$FeAl - SiO_2$	36.17	0	23.11	0	0	1.57	38.53

4.7 Technical Approach

The above techniques combine to give a unique approach to the interrogation of the project hypotheses.

The extensive experimental sampling and recording of data within the IMPHOS project offers a unique set of information to cohesively interrogate the refining pathways present. The sequential multi-layered sampling offers the highest time-resolved in-situ sampling of a BOF today, with the addition of the converter process being able to continue while sampling takes place, there was the opportunity to take samples more representative of the continuing process than ever before.

In addition the multiple heats, accurate reporting of processing parameters and time-resolved off-gas analysis, gives the opportunity to truly see how process parameters affect the distribution of refining contributions with the reported bulk bath, hot zone and emulsion zones of the BOF.

The laboratory based techniques offer several advantages. HT-CSLM allows for the controlled suspension of a metal droplet in a slag phase, which is able to heat at relatively high rates ensuring close time proximity of slag and metal melting. This offers the ability, along with in-situ observation of the slag melting, to report a true $t = 0$ for interaction to occur. In addition HT-CSLM allows for the in-situ observation of the phenomena when optically transparent slags are used. This is necessary to truly appreciate how spontaneous emulsification progresses (for instance in such an instantaneous manner for the higher $FeAl$ content samples). Variation in user application can have a significant effect upon HT-CSLM results, this is due to effects of surface roughness on light radiation heating, required speed of image focusing response and maintenance of the chamber environment. To develop this technique it required signifcant investment of time and process improvment, for example: Deducing the correct amount of slag to pack above and below the metal droplet to avoid interaction with the crucible or floating of the metal on the slag surface; maintenace and cleaning of both the HT-CSLM chamber and argon gas (removal of oxygen down to ppt levels) in order to avoid contamination or the metal droplet oxidizing before the reaction could take place; correct alighnment and trial of the heating profile programming in order to attain the desired sample temperature profile (as the control thermocouple is attached to the bottom of the sample stage, not the sample itself); experties of focusing on a moving target (melting surface) in order to gain image data from a near t=0 point; improvment of experimental set-up to increase the homogenouity of temperature through the sample (through use of saphire crucibles and sample location testing) to enable the molten droplet to remain still enough for imaging; introducing helium gas as a quenching enviroment in order to preserve molten morphologies to room temperature. The above lists some of the major factors in controlling the HT-CSLM experiments in order to gain the insights presented in this thesis. Although a significant amount of experimental development was required, once a working proceedure was identified the experiments became extreamly reliable.

In addition, the small sample size within the HT-CSLM allows for rapid quenching of the sample by turning off the heat source and introducing an atmosphere with higher thermal capacity (in the case of these experiments swapping from argon to helium gas). This allows for reliable shape retention from liquid to solid and thus ex-situ XCT can be applied. High-resolution XCT for well-defined phase boundaries and spatial confidence requires long scanning times, giving limitation to the ability of using the techniques in a high-throughput fashion.

XCT offers 3D calibrated analysis of the physical shape and size of each phase within a sample. This is favourable compared to other techniques used in the literature such as SEM or X-ray radiography as these only allow you to see either a given cross section or the largest form of the droplet in all directions respectively. There are obvious inherent issues with each of these.

Finally, phase-field modelling is unique in its depiction of the interface. As experiments within this project are interface driven it is thus the chosen method. Phase-field modelling offers the ability to track composition change, the tension of the interface with respect to angular strain and the spatially dependent driving force of reaction. These couple to give a good interpretation and visualization through image output of the cause of spontaneous emulsification. The unavoidable issues with phase-field modelling are the need to define an interface width (usually over estimated) and the significant computational effort required.

Chapter 5

Calculating the Macroscopic Dynamics of the Gas/Metal/Slag Emulsion During Steelmaking

5.1 Hypothesis to be Interrogated

Hypothesis 1: “Periods of greater dephosphorization in the BOF correspond to times of greater interfacial area between slag and metal.”

Hypothesis 2: “The use of in-situ sampling and 3D volumetric analysis of droplet sizes produced within the BOF will offer updated, more accurate results than previous methods.”

These hypotheses present a platform to interrogate the environment within the BOF and to quantify the nature of the transient slag/metal interface present in the emulsion zone.

5.2 Introduction

Currently phosphorus levels are controlled through operation of the Basic Oxygen Furnace (BOF); however this is a secondary function of the converter, whose main job is decarburization (the reaction pathways shown in equations **??** and **??**. As a result processing parameters have to be balanced and inhibiting factors such as oxygen removal and high temperatures occur which reduce the phosphorus refining performance of the BOF.

The dephosphorization reaction consists of a series of potentially kinetic limiting steps:

1. Transfer of phosphorus from bulk steel to slag/steel interface
2. Transfer of oxygen ions from bulk slag to slag/steel interface
3. Chemical reaction at slag/steel interface
4. Transfer of oxygen from slag/steel interface to bulk steel
5. Transfer of phosphate ions from slag/steel interface to bulk slag

As previously stated in the chapter entitled ”Underpinning Knowledge” it is typically assumed the chemical reaction at the interface can be ruled out as rate limiting due to the speed at which it takes place. As a result the rate is believed to be predominantly controlled by the mass transfer of ions in either or both bulk metal and slag [22] [77] [78]. The term “bulk metal” in this case refers to a region where the material is compositionally constant in space and could be in the metal bath or inside a metal droplet. This leads to a rate of dephosphorization dependent upon metal packet size, and the time period required for that metal to refine. Therefore the transient interfacial area is a macroscopic kinetically restricting factor for phosphorus refining. The quiescent interface of the bulk bath is a small portion of the overall metal/slag interface, as the emulsion phase of the BOF contains a dispersion of metal packets/ droplets. Previous studies have investigated the range of what sizes these droplets are [4] [51] [39] [40] [42] [43] [44] [46] [38]. However coupled with this information it is important to know the percentage of metal accounted for in the emulsion (% tap weight), the metal circulation rate within the emulsion (as this affects localised diffusion gradients), and how long the metal remains in the emulsion (residence time).

Residence times have been both modelled and calculated from blow sampling in several previous studies. The residence time is defined as the period of time which has lapsed between a “packet of metal” leaving the surface and re-entering the bulk bath. Table 5.1 shows a summary of the previous reported residence times, the author and the method of calculating/modelling the process.

The IMPHOS project was a European funded project to investigate the process of phosphorus refinement in the BOS converter. A 6 ton converter was sampled at systematic time intervals, simultaneously at selected levels throughout several heats. This sampling procedure enabled metal collection and compositional analysis of the metal in the emulsion in addition to that in the bulk bath during an un-interrupted blow. Using data from IMPHOS trials macroscopic dynamic factors such as the mass of metal in the emulsion, the average residence time (ART) of this metal, and the dynamic emulsion flow speeds can be calculated. The accurate quantification of these parameters is vital to fully understanding and optimising BOF refining. This chapter explores calculating macroscopic dynamics based upon carbon mass balancing from realistically attainable plant data, whilst neglecting previous widely accepted significant factors to still offer an accurate result.

Table 5.1: Collation of previously reported residence times, with the experimental/modelling technique used.

Author	Method of Deduction	Residence Time (s)
Price [38]	Gold isotope tracking, plant measurement	120±30
Kozakevitch [51]	Plant measurement of carbon and phosphorus level predictions in metal	60-120
Brooks et al [52]	Revised prediction to droplet trajectory model, with bloated droplet effects. On a defined 15% FeO and <85% gas fraction	20-80
Dogan et al [54] [79]	Similar to Brooks et al, but 14-30% FeO content screened and a fixed gas fraction of 80%	0.4-45
Qing [53]	3-D two phase (mercury/glycerine) model	1-40
Schoop et al [80]	Calculated from a kinetic model and chemical analysis of indirect plant samples	~ 60

5.3 Experimental

5.3.1 Heat Characteristics

This chapter interrogates 14 of the 25 heats conducted during the IMPHOS trials; these heats were selected due to consistently reliable data sets, and the inclusion of varying factors such as sampling time and hot metal silicon content. The heats included are: S1828-S1837, S1840, S1843; S1845 & S1846, the nomenclature for heat naming has been kept the same as the original IMPHOS report for ease of reference [4].) The IMPHOS report is publically available and can be found on the website for the European Commission.

The nominal composition for hot metal used in the trial is given in Table 5.2 and is near “normal” to hot metal outputs from the blast furnace in industrial practice to increase relevance to application.

Table 5.2: Nominal start composition of hot metal used in IMPHOS trials.

C mass%	Si mass%	Mn mass%	P mass%	S mass%	Temp ^{o}C
4.75	0.45 or 0.6	0.45	0.085	0.03	1375

Further breakdown of individual heat conditions, and parameters such as ‘V’ ratio (mass% CaO/mass% SiO_2), lime addition, lance height profiles and tapping temperatures can be found in the European Commission report [4]. The author recommends the data in the report is considered when evaluating the findings in the present work.

IMPHOS trials were carried out at Swerea MEFOS, Sweden, with use of the 6 tonne pilot plant BOS converter. The converter has a lining of Magnesia-Carbon (fired and fused) bricks, and is fitted with a single bath agitation tuyere blowing nitrogen at a rate of $0.5Nm^3min^{-1}$ and a water-cooled oxygen lance with a single De-Laval nozzle (a convergent divergent nozzle; a pinched geometry to make an asymmetric hourglass shape) blowing oxygen at $17Nm^3min^{-1}$. A schematic of the converter can be seen in figure 5.1 containing dimensions, sampling pot locations and labelling of the terms used later in calculations.

Sampling of the converter was carried out via robotic delivery of specially designed sample lances at 2 minute intervals throughout the blow. The lances consist of an inner and outer structure of three mild steel bars, the inner being joined to

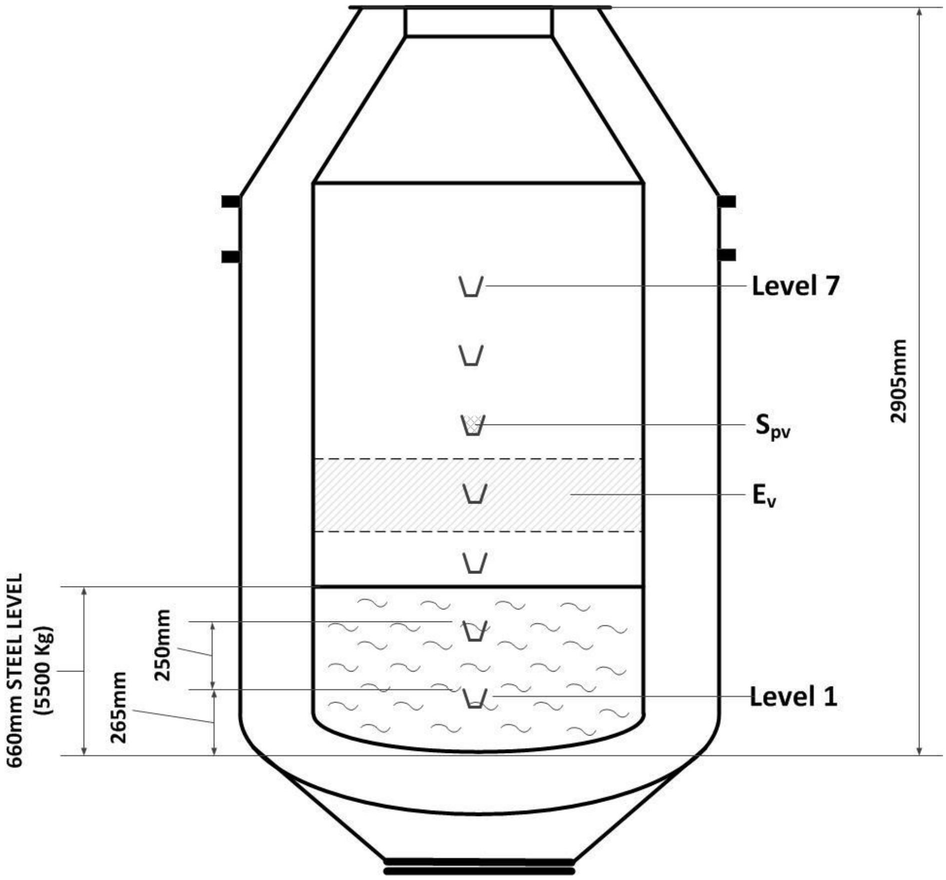

Figure 5.1: Schematic of MEFOS 6 ton converter with sample levels, dimensions and S_{pv}/E_v defined

the sides of inline sample pots, the outer joined to the sides of disc sample pot lids. The lance is lowered into the converter through an opening in the top (with a slight offset from the oxygen lance), with the lids in the closed position. Once lowered into position, the outer three bars are retracted lifting the lids in-situ, allowing the sample pots to fill. The lids were then closed after 3 seconds for all heats in this study, apart from S1844, S1845 and S1846 where the lids closed after 3.5, 4 and 5 seconds respectively. The lances are then retracted from the converter, the lance carousel rotates and the next lance is lowered after 2 minutes.

A small flake of each sample was extracted (for SEM analysis) after the full sample was weighed. Each sample was then passed three times through a small hammer mill. The material was then magnetically separated by hand-held magnet.

The now magnetic and non-magnetic fractions were weighed separately, and chemically analysed via spark OES. The original IMPHOS report used this to separate the heats into 5 characteristic phosphorus refining profiles. A full collation of

IMPHOS sample chemical analysis can be seen in the report.

5.3.2 Model of BOS Converter for Calculating Macroscopic Dynamics

Initial Analytical Input

The method of calculation used in this thesis has a significantly different assumption from that previously assumed in that sampling was linearly dependant on sample pot opening times. It has now been assumed that the sampling of the converter was instantaneous upon opening of the submerged sample pots, and the content of the pot does not change with time.

The reason for this assumption is that upon inspection of the amount of material collected in sample pots, as a function of sample pot opening time, longer opening times lay within the spread of data produced by the normal three second sampling time for this experiment. If sampling was to depend upon the pot opening time, it would be expected that a trend would exist where the average metal collected per pot per heat would increase with sample pot opening time.

Along with this change in sampling interpretation, a new method of modelling the macroscopic dynamics has been proposed which relies heavily on quantified off-gas analysis. Off-gas analysis is notorious for being inaccurate for full converter analysis. To minimise potential error a mass balance has been carried out between the mass of carbon lost between input and output hot metal, and that detected in the off-gas.

From the carbon mass balancing a discrepancy of up to around 13% can be seen, yet in most cases reasonable agreement is seen. To combat this discrepancy, off-gas carbon detection is given a correction variable which uniformly distributes the discrepancy across a heat's blow time.

Method of Macroscopic Dynamics Calculation

The model created in this study uses output analysis from IMPHOS trials [4], such as metal masses, chemical compositions and converter parameters. The main process is an iterative carbon mass balancing between elemental analysis of emulsion zone metal, and that of the bulk bath metal. Carbon mass balancing is used due to the off gas detection offering a higher time resolution sampling in refined material, as opposed to using phosphorus or silicon removal which would only be correlated to the less frequent 2 minute slag sampling. Also decarburization continues to a measureable point throughout the entire blow, where as other impurities are heavily refined earlier, and change little towards the end. Firstly the overall mass of metal in the emulsion zone is calculated through ratio scale up between sample volume and converter volume. The carbon mass balancing of this metal with the timeline of bulk bath composition in the same mass of metal is then used to calculate the ART. Finally a relationship between mass of metal collection and its period of residence is used to calculate metal circulation rate.

Equations 5.1 - 5.6 show the necessary steps for calculating the mass of metal in the emulsion, the ART of metal in the emulsion and the metal circulation rate within the emulsion.

Key assumptions beyond those previously stated are:

- The emulsion phase is solely responsible for decarburization. In this study the emulsion phase is defined as levels 4-7 in the IMPHOS converter. Although it is known that there are contributions from the bulk bath, and accelerated rates from the hot zone (the area of oxygen jet impact on the metal bath surface), this was deemed a reasonable working assumption due to the known high rates of carbon removal in the emulsion type phase, a check of the validity of this assumption is offered after the discussion. As such, levels 1-3 are considered bulk bath/interface samples and above level 7 the density of slag is assumed to be such that refining potential would be greatly reduced (a foam).

- The population (mass) of metal in the emulsion was consistent and remained constant throughout the time period covered by the calculated ART unless the calculated ART spanned two sampling points, upon which a regression of change was factored into the calculation. This assumption was necessary in order to perform the calculation and should be evaluated for each individual point as to its reliability. An indication as to its reliability may be to assess the change in metal circulation rate over the relevant time period.

- Sampling was a fair representation of environment throughout the full horizontal plane of the converter. This assumption is not strictly accurate in the vicinity of the main lance and the wall of the converter, but it is adopted because of simplicity. Thus if a cylindrical geometry is considered, it is assumed the changes are only in the z-direction thus rendering the problem 1D. This was considered to be a fair estimation when assuming constant population as material travelling in both directions through a section should be near equal.

Measured input data to the model includes:

- M_o = The mass of metal collected in a single sample pot.
- S_{pv} = The volume of a single sample pot.
- E_v = The volume of a defined section of the emulsion zone (depicted in Fig. 5.1).
- $C_{(e)(t)}$mass% = The average measured carbon mass percent of the metal from a sample pot in the emulsion zone.
- $C_{(e)(t)}$ = The total mass of carbon in the metal fraction of the emulsion zone at a point in time.
- $C_{(bb)(t)}$ mass% = The average measured carbon mass percent of a sample from the bulk bath (layer 1 in the sample lance).
- $C_{(bb)(t)}$ = The actual mass of carbon in the equivalent mass of metal collected in the emulsion at the interrogated time.
- $C_{(o)}$ = Mass of carbon detected in the off-gas analysis in 1 second.

Firstly the mass of metal in the emulsion at a point in time is calculated ($M_{(e)(t)}$) using a scaling factor dependant on effective emulsion zone and sample pot volume:

$$M_{(e)(t)} = \Sigma M_o(E_v/S_{pv}) \tag{5.1}$$

To carry out this calculation, first the emulsion volume must be deduced, this is achieved by interrogating the slag height profiles of the heats, calculated by inspection of the slag line on a sample lance. Also, in order to get a full representation, missing sample data has to be predicted, for instance if data was available for levels 4 and 6, but not 5, since we know 5 must have been occupied. This was done by fitting of a regression given by a full data set within IMPHOS trials with similar known results. The appropriate regression is taken from a heat with similar characteristics (sample sizes, and known distribution) and from the same time point as the sample set with missing data. There is strong consistency in these profiles, the match should give a realistic result.

Next the mass of carbon in the overall emulsion metal at a point in time must be calculated ($C_{(e)(t)}$) with use of a measured carbon mass percent of metal, and scaled metal content of the emulsion:

$$C_{(e)(t)} = \Sigma(M_o(E_v/S_{pv})/100)C_{(e)(t)mass\%} \tag{5.2}$$

The mass of carbon in the bulk bath is now calculated as a function of time for the same mass of metal as was found in the emulsion at time (t). This is done by using the measure of carbon mass% of bulk bath metal throughout the blow and the scaled mass of metal in the entire emulsion ($C_{(bb)}$):

$$C_{(bb)(t)} = (M_{(e)(t)}/100)C_{(bb)(t)mass\%} \tag{5.3}$$

It is now possible to add off-gas carbon detection values to the emulsion metal carbon weight, in 1 second steps back in time from the sampling point. This time-step carbon addition will intersect the local linear regression of analysed bulk bath carbon content for the corresponding heat, as such:

$$C_{(bb)(t-tr)} = C_{(e)(t)} + \Sigma_{i=o}^{n} C_{(o)i} \tag{5.4}$$

Where $C(o)$ is the mass of carbon, detected in the off gas in the nth second, prior to sampling. The ART of all metal in the emulsion at time t in seconds is (tr):

$$t_r = n \tag{5.5}$$

This includes metal recently ejected from the bulk bath, the metal soon to re-enter and all points in-between. Given the units of $M_{(e)(t)}$ (kg), and t_r (s), it is now possible to calculate the metal circulation rate (MCR) within the emulsion as defined previously by Millman et al [69]:

$$MCR = M_{(e)(t)}/t_r \tag{5.6}$$

5.3.3 X-ray Computed Tomography

Flakes of emulsion in solidified form from four different samples were scanned using X-ray Computed Tomography (XCT) for 3D observation of the steel in slag. Furthermore this could be segmented to determine the position, size, volume and surface area of each droplet contained within the slag. From the relatively uniform distribution of pores and metal droplets through the samples it is expected the samples solidified rapidly (if a slow solidification took place it would be expected that the different phases in a sample would have separated by density to a large extent, this behaviour was not seen), as such the ex-situ investigation of the droplet sizes and distribution is a good representation of the original environment.

The sample is placed on a rotating turntable between the source and detector. The scanner used in this study was the Nikon XT 225/320 with the parameters listed in Table 5.3. As X-rays traverse the sample they are either attenuated or pass through resulting in a grey-scale radiograph on the screen. Numerous images are taken through 360 degrees which are then reconstructed into a 3D volume through the process of filtered back projection. The volume consists of a number of 3D pixels called voxels with an associated grey value between 0 and 65535, proportional to the attenuation of the material. Validation of the instrument's accuracy has been reported by Kumar et al [81].

Table 5.3: XCT scanning parameters used for the interrogation of solid emulsion shards removed from the sampling pots.

Voltage (kV)	180
Current (micro A)	24
Exposure (s)	2.8
Filter (Cu, mm)	0.5
# Projections	3200
Voxel size (microns)	41

5.4 Results

The % tap weight (the amount of metal in the emulsion as a percentage of final tap weight), ART and metal circulation rate within the emulsion at a point in time have been calculated for 14 heats from a 6 ton pilot plant basic oxygen furnace. The highest average %Tw in the emulsion being 31.07%, and the highest average ART being 69 s; both of which occur in heat S1835. The highest average metal circulation rate is that of S1837 being 305.41 $kg\ s^{-1}$. Much larger variation is seen in the MCR of blows than that of t_r and %Tw . Table 5.4 shows the overall averages of all three parameters, and their respective standard deviation to give an idea of cross heat differences.

Table 5.4: Overall average and SD of %Tw, t_r, and MCR for all blows.

	Overall Average % Tw	Overall Average t_r s	Overall Average MCR kg s^{-1}
Mean Average	21.30	39	87.48
Standard Deviation	6.40	16	72.44

For the purposes of this discussion the selected IMPHOS heats have been split into three groups based on their computed ART profiles, these groupings are qualitative and a device to aid presentation and discussion of results in the thesis, the author is not stating it is possible to categorise all BOF profiles coherently into one of the three groups presented here. The three groups are: “Mid blow inflection” where the profiles show a raised and sustained relatively high ART through early blow, followed by a drastic decrease around the middle period of the blow, with the ART then staying low for the remainder of the blow; “High start then fluctuation” when profiles show a large rise in ART up to 6 minutes into the blow, this peak then rapidly decreases, followed by smaller fluctuations up and down in ART for the remainder of the blow; “Residual Heats” show profiles unfitting to the previous two groupings, these can be from an increased sustained high ART, to peaking mid blow, or even a very low ART profile throughout the entire blow. There is no correlation between these groupings and the operating conditions, input parameters or measured output data from the experimental trial. Similarly scales of the different grouping graphs that follow are different in the y-direction due to significantly varied numerical results and the need to keep profile differences clear within a single sub-set.

5.4.1 Amount of Metal in the Emulsion

The amount of metal suspended in the emulsion is given as a percentage of the final tap weight, rather than the input hot metal mass. This is due to FeO production and sublimation of Fe material during a blow, resulting in a reduced possible mass as the process continues. This is given as a function of blow time in figure 5.2.

5.4.2 Average Residence Time in the Emulsion

It should be noted these calculations are ART for packets of metal in the emulsion. When the process is considered it is correct to propose that the spread of residence times is variable from the calculated average through to a near zero second residence time, for instance some material will re-enter the bulk bath almost as soon as it leaves. Therefore residence time of individual packets of metal will be greater than the average calculated. This should be taken into account when interpreting the given ART, the defining of the greatest divergence from the calculated ART (min and max) is however beyond the scope of this work. The ART as a function of blow time is given in figure 5.3.

5.4.3 Metal Circulation Rate in the Emulsion

The speed of movement affects the end of blow results as apposed to a significant drop in the mass of metal moving. With the exceedingly high rates seen in the last 2 minutes of the blow within the converter emulsion it is important to consider two things; the first thing to note from the results of metal circulation rate is the graph gives the illusion of a sustained rate up until the very high end-blow values, seen in figure 5.4. Secondly, the metal circulation rates reported are an average of the overall emulsion, much as the reported residence times; individual packets of metal may be moving much faster or slower than the times calculated here.

5.4.4 XCT Results of Slag/Gas/Metal Emulsion Samples

An example 2D orthoslice of the resulting volume can be seen in figure 5.5 where the bright white areas are metal droplets, the light grey areas slag material and black areas porosity. As can be seen in the image the attenuation, and hence grey value, of the slag is much lower than the steel, allowing for simple segmentation using the Otsu

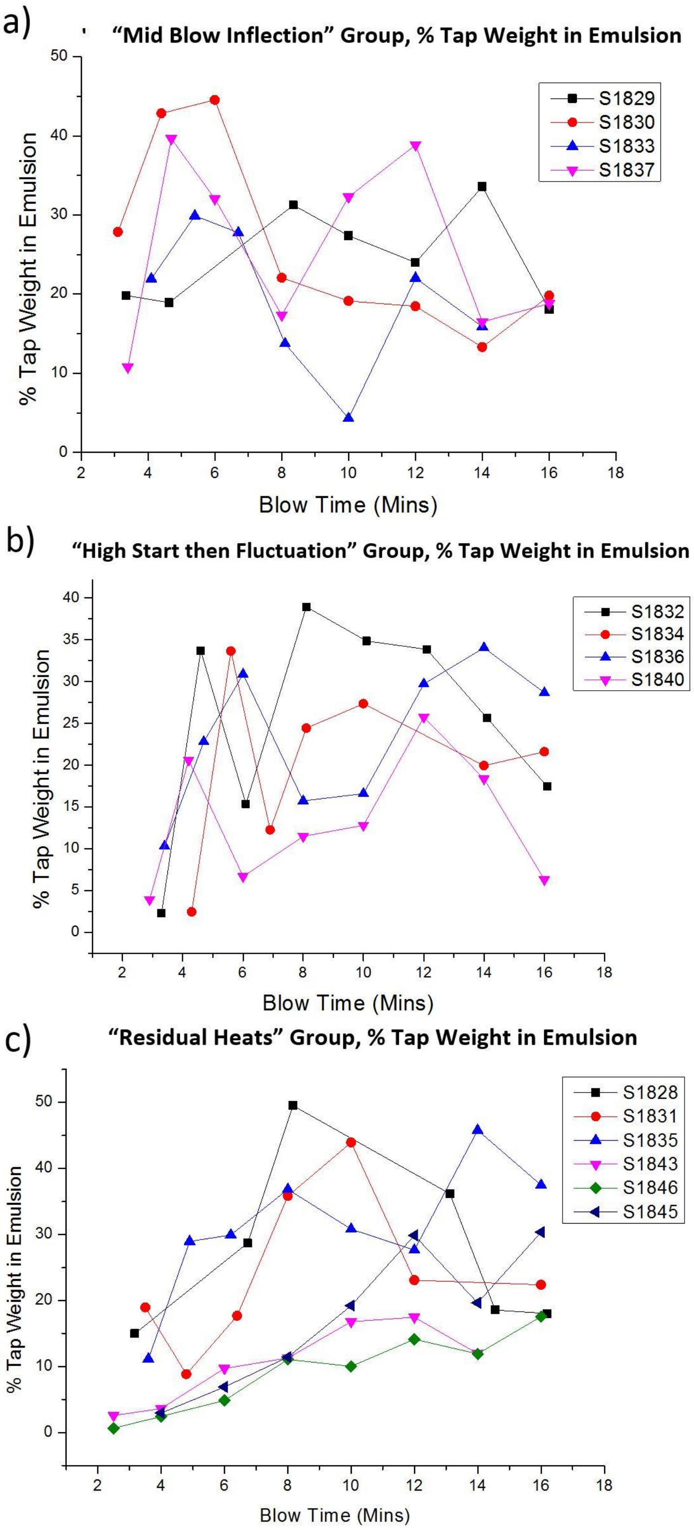

Figure 5.2: The amount of metal in the emulsion as a percentage of final tap weight. a) “Mid blow inflection” group, b) “High start then fluctuation” group, c) “Residual heats” group.

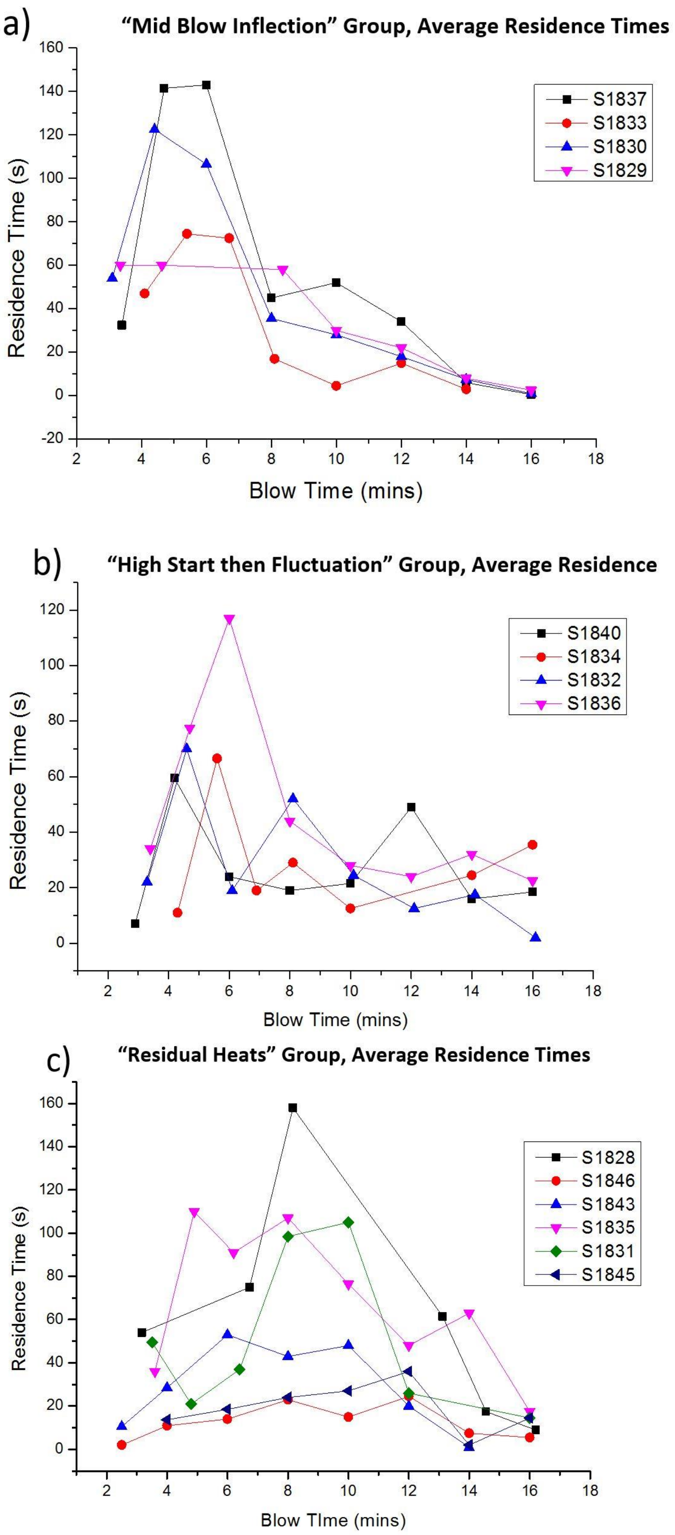

Figure 5.3: The average residence time as a function of blow time. a) “Mid blow inflection” group, b) “High start then fluctuation” group, c) “Residual heats” group.

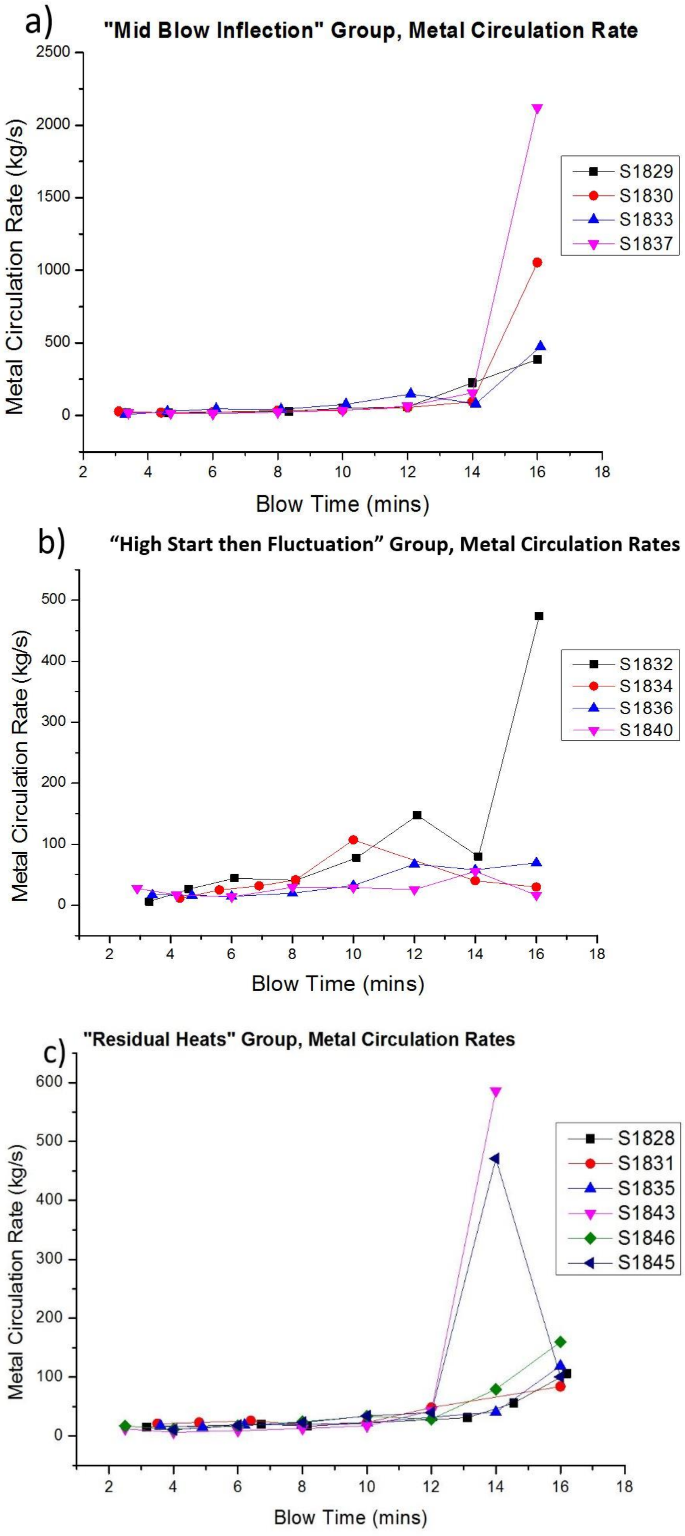

Figure 5.4: Metal circulation rates in the emulsion as a function of blow time. a) "Mid blow inflection" group, b) "High start then fluctuation" group, c) "Residual heats" group.

method [81]. The 3D output of the segmentation can be observed in figure 5.6 where the metal can be seen as light grey areas in the emulsion shards, and the slag (darker grey) has been made semi-transparent to allow viewing through the sample. Using the analysis software Avizo 8.1 (FEI, USA) individual steel pellets were then analysed for each individual flake providing the min/max diameter, volume and surface area. Table 5.5 gives an overall example of the results from XCT interrogation of the shard emulsion samples.

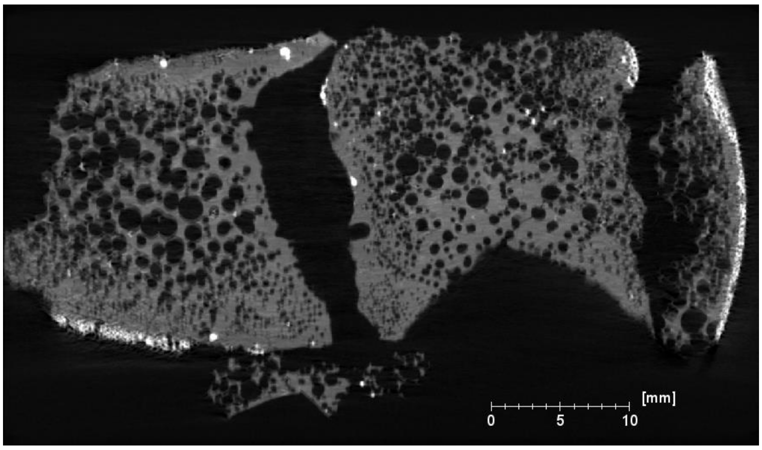

Figure 5.5: 2D orthoslice of the 3D volume. There is a clear contrast between the steel (whitest), the slag (grey) and porosity within the sample (black).

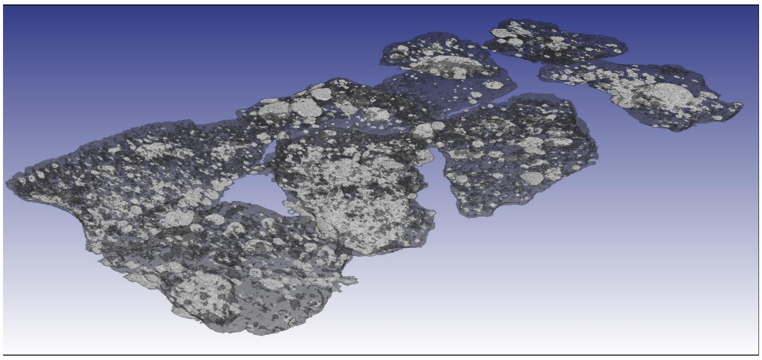

Figure 5.6: 3D segmentation with semi-transparent slag phase in order to see the dispersion of metal droplets (light grey).

With the use of XCT, the authors are able to remove any droplets which may have been dissected at the surface of the sample from the output results. This removes the unreliability of unknown droplet sectioning as has previously been the case in similar studies, as well as the linking of what would appear to be separate

Table 5.5: Initial results from XCT scanning of shard emulsion samples. The number of discrete metal packages detected and their average diameter.

Sample ID	No Droplets	Mean Droplet Diameter μ m
S1840-4-4	1062	375
S1840-4-5	841	292
S1840-4-6	469	307
S1840-4-7	133	322
Combined	2505	324

droplets on a sample surface but are in fact connected in the subsurface of the material. Along with the greater certainty of droplet size, XCT allows for a greater sample set to be analysed as the full dispersion of droplets through the sample can be investigated, not just those at the polished surface as has been the previous method via optical microscopy [4]. Visual investigation of the reconstructed images showed that many metallic surface sections showed the sub-surface linking previously suggested. Coupled with the detection of larger droplets than sizes previously reported, this gives the explanation as to why the average droplet size reported in this study is so much larger than the 28-51 micron range and modal 20 micron average previously reported for these samples [4].

5.5 Discussion

5.5.1 Residence Times

The highest calculated ART is that of heat S1828, 8.2 minutes into the blow with a value of 158 s. This value is of the same magnitude of most previous work with the closest being that of Price and the isotopic labelling technique [38]. This high value is an outlier and if the overall average of 39 s is taken, the author believes the results to be closest to that of Brooks et al. [52], of 20-80 s, giving a mid-point closest to the average value here, as well as a realistic range.

It should be noted that the highest ART calculated do not necessarily correspond directly to times of the highest decarburization rate, in fact there is a strong correlation of highest ART peaking just prior to the largest decarburization rates as seen in figure 5.7 (the decarburization rate has been calculated from the measured carbon content of sampled bulk bath material through the respective blow;

it is noted that the decarburization rate profiles show strong similarity within the groups that have been defined by residence time performance, indicating a significant link between the two). This makes sense as the decarburization rates are calculated from the bulk bath measurements. As the refining takes place in the high residence time droplets, a time-lapse close to the previously measured residence time would be required in order to notice this effect. As an example S1837 has a peak in ART at 6 minutes followed by a peak in decarburization at 8 minutes. As ART is over 120 seconds at 6 minutes, it is understandable that the higher decarburization performance is not expressed until later into the blow when these longer exposed packets of metal have had time to recombine with the bulk bath. Thus it is strongly suggested high residence times lead to higher decarburization rates. This is in agreement with the work by Brooks [52], as the initial trajectory modelling carried out was given a correction of transient droplet density due to decarburization reported by Molloseau and Fruehan [82], resulting in the previously reported values by Brooks.

There is a visible correlation between points of higher ART and higher dephosphorization rates, as shown in figure 5.8 (the dephosphorization rate has been calculated from the measured phosphorus content of sample bulk bath material through the respective blow; it is noted that dephosphorization rate profiles show less agreement with the residence time groupings than decarburization, however there are still more common profile trends within each group). This correlation is seen in the early blow with factors such as unfavourable temperature rise, removal of FeO from the slag by decarburization and a reduction in phosphorus partition gradient becoming increasingly unfavourable through the blow.

If the accepted strong link of high decarburization rates inhibiting dephosphorization are considered and taken into account when observing the given profiles, it is arguably seen that dephosphorization rates are slightly higher at periods of higher ART. This should be understood to be due to a larger effective interfacial area between slag and metal, which aids in dephosphorization due to the nature of phosphorus refinement through interfacial exchange. Not only is there a potential for greater numbers of droplets in the emulsion phase at higher ART (assuming constant droplet formation), the individual droplets are in contact with the slag for a longer period of time, allowing for reactions between the two phases to occur for longer and impurities to gain a closer phase balance to thermodynamic equilibrium.

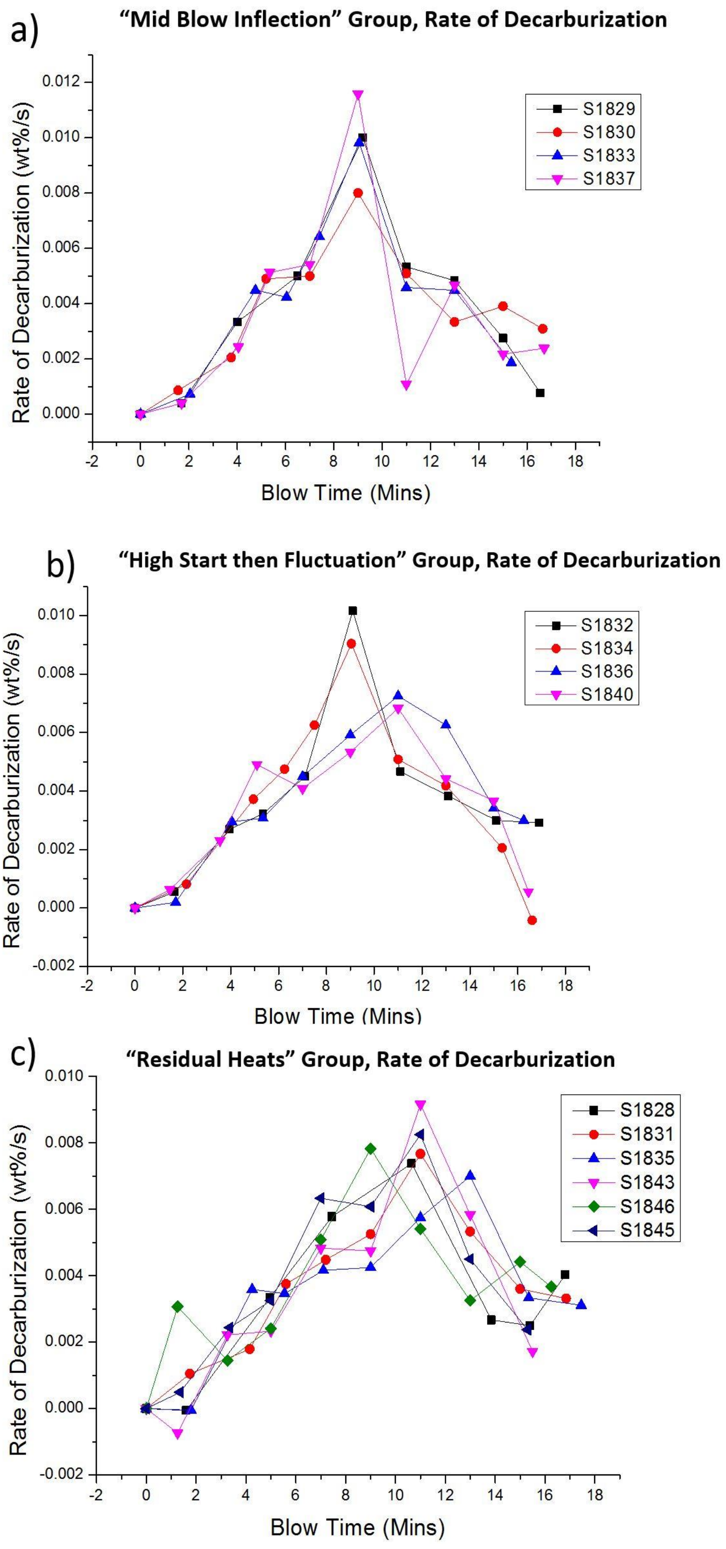

Figure 5.7: Rates of decarburization from IMPHOS analysis. a) “Mid blow inflection” group, b) “High start then fluctuation” group, c) “Residual heats” group.

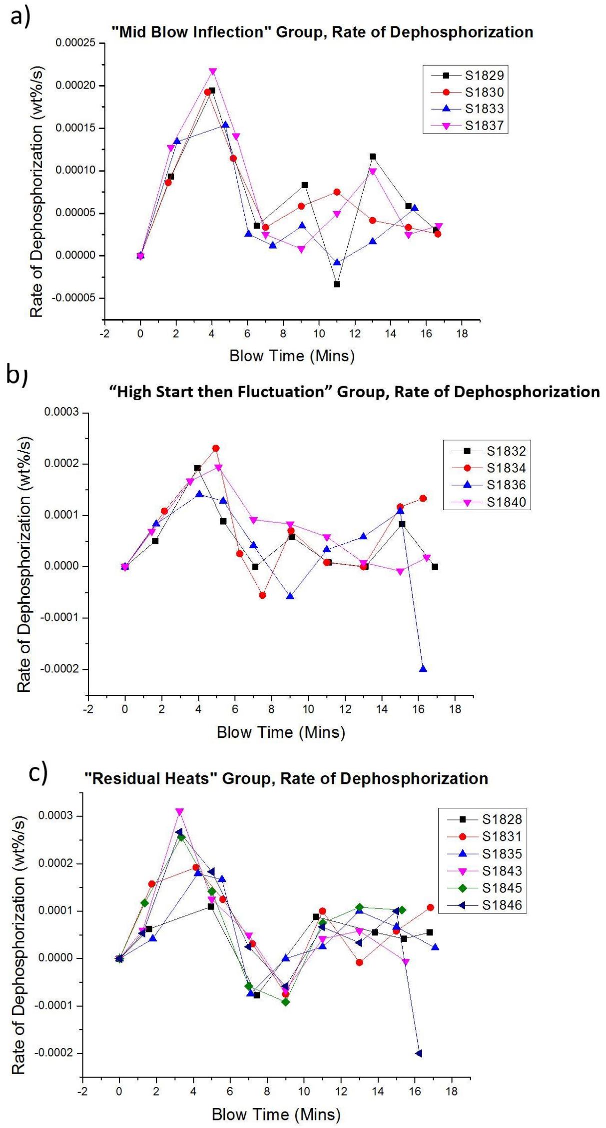

Figure 5.8: Rates of dephosphorization from IMPHOS analysis. a) "Mid blow inflection" group, b) "High start then fluctuation" group, c) "Residual heats" group.

5.5.2 % Tap Weight in the Emulsion

The largest value of % tap weight in the emulsion is that of heat S1828, at 49.5%. This is a supported value with several points of different blows above the 40% mark and at only twice the overall average calculated, compared to that of the highest ART being nearly four times its overall average calculated.

When % tap weight trends are compared to lance height profiles as reported previously by Millman et al. [83], it can be seen that changes in lance height have an effect on the % tap weight in the emulsion. Regardless of direction, a change in lance height appears to increase the value, whereas long periods of stagnated lance height tend to cause a trend back towards a minimum of around 10% (most values are above this after the initial 2 minute calculation).

It is difficult to interpret the effects of different levels of metal mass in the emulsion upon refining output directly, as without information on size distribution the effect on surface area and mass transport times are effectively unknown. Further work on IMPHOS data is planned to deliver better understanding in this area.

5.5.3 Metal Circulation Rates

The metal circulation rates have an apparent vast range. The highest value being 2,120.39 kg s^{-1} from heat S1837 which is an outlier from the majority of values which are below 150 kg s^{-1}. This value is partially due to the calculated ART being the only value computed for the parameter below one second, as a result effectively doubling the % tap weight in order to calculate metal circulation rate. As there is little agreement in % tap weight values in end blow, this trend of high MCR towards the end of the blow can be attributed to a reduction in ART. This effect is not seen in early blow where residence times are also 'low' because effects such as significantly lower masses of metal in the emulsion are also playing a role causing the effect to be reduced due to the nature of the model.

This is understandable due to reduction in metal droplet bloating from decarburization; the smaller higher-density metal packages would be able to penetrate through the slag medium with greater ease. Also when events such as slag layer collapse are considered, along with the sampling technique where only samples submerged in the slag layer are considered, it is unsurprising these circulation rates are so high when a consistent ejection of material from the bulk bath is coupled with a reduction in emulsion zone volume. It is also possible that due to the reduced effective emulsion zone, the assumption of 100% decarburization in the emulsion begins to break down, and the process is governed more strongly by bulk bath/slag interactions and hot zone refining.

With the exclusion of the high end values, there is still a general trend for MCR to increase as the blow time increases. This is a very slight increase and may be accounted for through measurement of emulsion viscosity reduction due to temperature increase (reducing slag viscosity), or higher gas fraction contribution to the overall emulsion composition. Evidence for the latter is shown by the sudden peak in decarburization shown in S1832 at 10 minutes into the blow, followed shortly by a brief increase in metal circulation rate by almost 90 kg s^{-1}.

5.5.4 Evaluation of Assumptions

The main observation that led to the diversion from the previously reported model by Millman et al. [32] was sample collection time being shown to have no overall effect on sample amount collected. As a result the method reported here was formulated. It is believed by the author that the actual sampling time does not simply correlate linearly with pot opening time, neither is it instantaneous; sampling is most likely to be variable, dependent upon height within the converter. As such a sample from level 4 would be more likely to be instantaneous as it is submerged in a denser, lower gas fraction medium. Whereas a sample at level 7 (which would be in a possibly more foam like medium) would have a continued filling for as long as the pot was open.

The assumption of constant population is at this stage believed to be fair. Metal circulation rates are not far from steady state, apart from an accountable rise through the main blow. Also an evaluation in the change in amount of material collected in consecutive samples shows mostly small variation.

Fair sampling of the converter is difficult to define. With the likelihood of interactions such as streams of metal possibly hitting a sample pot when open (which would be unrepresentative of the bulk emulsion phase), material over counting is a possibility. The other side to this assumption is that the environment is similar through a 2D horizontal sectioning of the converter. This environment will be significantly different close to the converter wall as opposed to at the oxygen lance in the centre. Recent work by Sabah and Brooks [84] [85], using a scaled-down cold model of water and air, has given significant support to this case. The authors intend to evaluate these effects in further work. In addition it should be noted the IMPHOS converter was only equiped with a single location for inert gas stirring in the base. Industrial scale converters can contain many more locations for intert gas enty with the amount and locations having significant effects of refining performance. It has previoulsy been reported that bottom blowing can reduce the residence time of metal droplets in the emulsion, due to a high gas fraction and thus reduced bouency (due to reduce contact with slag for decarburization - bloating/haloing; a lower foam density) [17].

Finally there is the assumption of 100% decarburization occurring within the emulsion zone. This is known not to be accurate but offers an initial estimation to construct this work. From the droplet size analysis carried out through XCT of the samples from heat S1840, coupled with the use of a decarburization rate per unit area and an average droplet size, it is possible to do a simple carbon mass balance to evaluate this assumption. The solid density of 7.874 g cm^{-3}, and a decarburization rate of 7.5 x 10^{-7} mol s^{-1} a lower bound taken from Molloseau & Fruehan's work [82] are used (an over estimation due to the closest available data being that for a 1 g droplet).

S1840 offers a mass of 554.82 kg metal in the emulsion and mean average droplet diameter of 324 μm at the respective time. The calculated number of droplets is 3.957 x 10^6. With an average droplet size ratio used the mass of CO_2 generated per second for one droplet is 4.627 x 10^{-6} g s^{-1}, and an overall CO_2 generation for the emulsion of 0.131 kg s^{-1}. At this point in time off-gas analysis detected 0.202 kg s^{-1} of CO_2. This gives a 64.6% possible contribution of CO_2 evolution to the droplets within the emulsion phase. A previous report of a similar estimation is made by Cicutti et al. [23], where the value range 20-50% is given for emulsion contribution to refining. From an initial glance this shows the estimation to be reasonable but not of high accuracy.

There are several factors to consider which lead to the calculated value being below what is expected in the true process. Firstly the decarburization rate implemented in the calculation was the most representative in terms of droplet size, this does not take into account the higher iron oxide levels in the slag at the time of calculation in the converter. Secondly the reported decarburization rate is from a static laboratory test where a quiescent gas halo is able to form and diffusion across this halo is likely rate limiting, this is unlikely to be the case in the industrial setting of converter decarburization when mass flow of material in the emulsion phase will disrupt a significant gas boundary forming, meaning ion mass transfer in the slag is more likely rate limiting. Given recent findings reported by Assis [62] and Spooner [86], where droplets are seen to spontaneously emulsify and the extreme increase in surface area this invokes, high values of emulsification contribution are possible. This would allow significantly higher decarburization rates, as such the above calculation does not take into account the morphology of detected droplets; spherical droplets are assumed.

The initial IMPHOS report grouped the heats into five dephosphorization profiles. No known reason behind the varied performance of the initial trials or the varied performances seen in industrial practice can be deduced from traditional methods of defining heat characteristics for example: lance height profiles, temperature measurements, input chemistries and slag phase formation. As such the behaviour has begun to be treated as chaotic. The new findings offer new BOF characteristic values to be compared with known refining performance measurements allowing for direct explanation of previously unjustified variances, such as peak times in dephosphorisation linking with peak points of average residence times.

The authors intend to carry out further work in order to offer further validation and potential correction terms into the model. Including: sampling time CFD modelling, scale up of sample contents dependant on location and converter zone contributions to the decarburization profiles. It is key to emphasise that without these more intricate additions to the model, there is still strong agreement with the previously reported findings in this area.

5.5.5 Consideration of Original IMPHOS Conclusions

The directly relevant conclusions from IMPHOS follow below, along with discussion on the insights currently presented:

1. “Consistent slag foaming only begins around two thirds of the way into the blow.”

    (a) Both percentage tap weight values and residence time values show less irregularity between heats in the last third of the blow. As slag formation, and foaming begin in a more sustained and predictable way (as well as a “deeper” slag layer), behaviour such as convection, droplet bloating/ trajectory and interaction with the furnace walls are likely to offer greater influence over metal droplet conditions than the fluctuating and erratic interaction of the high speed oxygen lance with the bulk metal bath, causing different splashing conditions.

    (b) The initial third of the blow shows the largest diversity in macroscopic dynamics, this is also the period of the blow when lance height, and temperature change most dramatically in a typical blow.

2. “Phosphorus removal takes place from the start of the blow.” (addressed with conclusion 3)

3. “Dephosphorization depends on changes in oxidation state of the slag and is driven by metal droplet-slag reactions and NOT bulk bath-slag reactions.”

    (a) This is supported with the high levels of residence time often seen in early blow, as is the characteristic of both the “mid blow inflection” and “high start then fluctuation” groupings.

    (b) High residence times- longer periods of sustained metal droplet/slag interactions allow for greater dephosphorization rates through reaction of dissolved P in the steel with FeO in the slag phase.

4. “Five alternative phosphorus removal profiles have been identified.”

    (a) The first profiles presented in the original IMPHOS trials are at best qualitative. The performance of these heats and characterisation into the five profiles are not explained through traditional heat characteristics. The observations made showing residence time and % tap weight profiles linking to rates of dephosphorization in this work begin to provide explanation as to why variable phosphorus refining performances are seen. Heats S1835 and S1836 show high levels of metal still in the emulsion phase at the end of the blow, thus for example the reduction of available oxygen for final carbon removal due to lance extraction or a final increase in temperature due to increased insulation from a stagnant slag foam, the larger amount of metal in the emulsion phase creates a susceptible condition for phosphorus reversion back into the liquid metal.

5.6 Conclusions

The % tap weight in the emulsion, average residence time of metal in the emulsion and metal circulation rate within the emulsion have all been calculated for a 6 ton BOS converter. The residence times reported show correlation with previously reported data from other authors, as well as reasonable correlation with carbon and phosphorus profiles. % tap weights are high and show up to nearly 50% of the overall metal may be suspended in the emulsion at a point in time. Metal circulation rates are shown to be rising in the order of a few kg s^{-1} throughout the blow; until end blow where these can increase dramatically, most likely due to slag collapse and the density of droplets being higher due to reduced decarburization. These calculations come from the first comprehensive set of data where a functional converter has been sampled in-situ at several time points during the same blow.

Within this body of work the correlation of dephosphorization profiles with the calculated macroscopic dynamics show interesting links with periods of higher residence times and % tap weights in the emulsion; these findings lead to the support of hypothesis 1, however there is some irregularity that requires further investigation when slag compositions and droplet size distributions are considered.

Assumption accuracy has been post analysed giving evidence for model validity in the current state. The novel use of XCT to interrogate droplet population within the emulsion zone, has also been conducted showing a 3D analysis of non-sectioned droplets to provide evidence to the amount of decarburization possible in the gas/slag/metal emulsion. The samples also are seen to show the capture of gas bubbles, and reactive droplet geometries. In addition images presented earlier in the chapter show the complexity of droplet geometries; 2D analytical techniques would never be able to detect these geometries, and could result in over counting of droplet numbers (not observing sections were connected below the surface) and clear misrepresentation of the droplet size. As a result it is believed hypothesis 2 is strongly supported and an extensive bridge of work using this technique would offer the most reliable data to date on BOF emulsion droplet size and distribution.

The variable morphologies of droplets within the emulsion presents a microscopic change in interfacial area during slag-metal reactions which requires further understanding and quantification.

Chapter 6

Investigation into the Cause of Spontaneous Emulsification of a Free Steel Droplet; Validation of the Chemical Exchange Pathway

6.1 Hypothesis to be Interrogated

Hypothesis 3: “Spontaneous emulsification is a result of material transfer across the metal slag interface, causing a drop in interfacial tension. This causes an overall increased rate of free energy reduction, physically expressed by the production of an increased surface area.”

Hypothesis 4: “Factors that are known to affect the rate of dephosphorization also promote spontaneous emulsification.”

These hypotheses aid in the development of findings in the previous chapter, where individual droplets in the BOF emulsion were seen to uptake non-quiescent spherical geometries; with respect to why these geometries may occur.

6.2 Introduction

Many steps in the process of steel making rely on the transfer of elements from metal to slag; a few examples are silica removal in the blast furnace [47], sulfur in the desulfurization pre-treatment [87], and phosphorus removal during steelmaking in the basic oxygen furnace (BOF) [88]. In the case of phosphorus refining in the BOF, much work has been carried out on the thermodynamic equilibrium between the metal and slag [30] [29] [28], giving evidence to the kinetic inhibition of the potential partition possible [22]. This lack of equilibrium could either be caused by lack of homogeneity in the slag layer of the BOF, (reducing the local driving force for phosphorus partition into the slag), or through kinetic restrictions through a deficiency of required interface for refining to transpose across/mass transfer controlling delivery of impurities to the interface [22] [77] [78]. Due to the inherent high temperatures, the reaction of material at the interface tends to be fast in comparison to the kinetically restricting mass transfer of materials in their respective bulk phases [22] [77] [78]. Current levels of understanding have extended beyond equilibrium conditions to include the description of mass transport in the slag and metal phases [17] [89] [90]. It is however known that under dynamic conditions the interface between phases can display significant perturbation in comparison to a relaxed planar state, and may even lead to emulsification [63] [64] [65] [66] [91] [92]. A proper description of the slag/metal reaction necessitates an elucidation of the dynamic change of interfacial area and the coupling of this change to the interfacial reactions. As such this work intends to investigate the effects of refining performance on interface morphology between Fe alloys and slags where mixing of phases may intrinsically occur to reduce the kinetic restrictions of mass transfer. Understanding when and by how much areas change during a reaction would be critical when describing the transient trajectory towards equilibrium in metallurgical processes.

In this study the specific case of the transient interface in the BOF emulsion phase is considered, which has previously been attributed to offering large contributions to the overall refining performance seen within the BOF [23]. The emulsion phase of the BOF is a mix of slag, gas (O_2, CO, CO_2), and metal droplets caused by the impinging oxygen jet delivered to the bulk bath surface overcoming the surface tension of the molten metal and shearing material away to form discrete droplets (as well as larger plumes of metal) [84] [85].

The reactive interface of metal and slag in this emulsion phase depends upon several factors:

1. Amount of metal in the emulsion

2. How long the metal stays in the emulsion (average residence time)
3. The size of discrete metal droplets
4. The morphology of metal droplets

Previous studies, including that of the present authors have investigated the macroscopic elements (points 1 & 2 above) of this interface. Reported residence times ranging from 0.4 to 120 seconds are given, with an average of around 40 seconds [38] [51] [52] [53] [54] [79] [80]. The amount of metal in the emulsion has been reported in a complete range of up to 50% of the tap weight dependant on blow time [32] [69].

With regard to the kinetics of a specific metal droplet in the emulsion, several authors have investigated variable aspects (point 3 & 4 above). Studies have been carried out both on industrial scale and laboratory scale on the size of quenched static samples; these results as well as how they were obtained are shown in table 6.1.

Table 6.1: A summary of the previous findings of metal droplet size in oxygen steelmaking emulsions.

Researchers	Place of collection	Droplet Size Range (μm)
IMPHOS [4]	Inside pilot converter, special lance	16-6360
Resch [42]	Paused and tilted converter	50-2000
Tokovoi et al [41]	Upper slag/metal emulsion	1000-2500
Cicutti [23]	Inside full converter, special lance	230-3350
Koria et al [46]	Slashed liquid outside crucible	40-70,000
Baptizmanskii et al [43]	Cutting hole in crucible wall	50-18000
Meyer [37]	Through tap hole, outside converter	150-3320
Block et al [39]	50-150mm above bulk bath inside converter	500-4000
Urquhart et al [40]	Inside full converter, special lance	63 - 2000

More recently work began into the tracking of a droplet transient morphology during refining processes. An example in this area is the work conducted by Rhamdhani et al. [63] where $Fe-Al$ droplets were immersed in $CaO-SiO_2-Al_2O_3$, the recovered metal droplets were then measured using a system of paper standards covering the droplet surface, giving an effective but rudimentory method of calculating the change in surface area. X-ray fluoroscopy and direct observation of in situ droplets has also given evidence to the change in droplet shape during Fe alloy/slag interactions [82] [92] [93] [94]. It has been proposed by these studies that the initial driving force is integral when evaluating the change in droplet morphology as the interfacial tension between the two mediums decreases rapidly allowing for interfacial area increase.

The use of microscopy is perhaps the most essential tool for investigative material science offering the ability to discern micro-structures at finer and finer scales; but usually a posteriori to a process. Professor Toshihiko Emi pioneered the use of laser confocal optics with an Au-image furnace allowing for in situ imaging, and his group at Tohoku University was the first to document the clustering of inclusions [95] [96], peritectic solidification [97], and particle pushing [98].

The present work, leads on from the initial findings of Assis et al. [62], where high-temperature confocal scanning laser microscopy (HT-CSLM) and micro X-ray computer tomography (XCT) were coupled together to provide insight into the full transient morphology of an $Fe-P$ 0.2 wt% alloy droplet submerged in slag similar to that seen in end blow BOF refining. HT-CSLM was used to provide a high heating rate reaction platform and XCT was used to offer 5 micron resolution 3D quantification of the metal-slag interface of quenched samples.

Initially a repeat of the previously reported work has been carried out to offer consideration to the consistency of the intricate technique used to produce the samples required due to the significant differences with Rhamdhani's [63] [64] [65] findings and give insights into the mechanism of spontaneous emulsification. This has been followed by initial chemical analysis of the samples from the previous study [62]. The results of which indicate the need for a further trial, where no phosphorus was present, leading to the exploration of oxygen transition across the interface causing spontaneous emulsification. A system at near equilibrium has also been studied to interrogate the need for a chemical exchange to cause the emulsification. The objectives of this work are to investigate (i) whether emulsification observed in the experimental drops are indeed caused by a chemical exchange (by comparing with a non-reactive system) and not by the experimental technique and (ii) to attempt to isolate whether it is caused by the transfer of phosphorous, transfer of oxygen, or both.

6.3 Experimental

The experimental setup consists of a HT-CSLM, used for its high heating and cooling rates. This is followed by XCT to give 3D representations of an entire sample. XCT also allows for identification of a representative slice through a sample that can then be sectioned, polished, and chemical analysis performed. The chemical analysis techniques used are: Inductively coupled plasma-mass spectrometry (ICP-MS), wavelength dispersive spectroscopy-scanning electron microscope (WDS-SEM), laser ablation-inductively coupled plasma mass spectrometry (LA-ICPMS), and secondary ion mass spectrometry (SIMS) .

6.3.1 Materials & Methods

The material used in the initial study has been reported previously [62]. In summary, it consists of an $Fe - 0.2$ wt$\%P$ alloy, which was reacted with a slag whose X-ray fluoroscopy (XRF) chemical analysis can be seen in table 6.2, this will be called S1.

Table 6.2: XRF detected chemical composition of master slags, used in this study and by Assis et al.

	$\%CaO$	$\%MgO$	$\%SiO_2$	$\%FeO_t$	$\%P_2O_5$	CaO/SiO_2	$\%Al_2O_3$
S1	36.64	7.08	16.98	33.56	1.66	2.16	0
S2	36.89	7.14	16.21	32.31	1.65	2.28	0
S3	38.15	10.26	16.89	34.70	0.01	2.26	0
S4	43.02	8.74	24.11	0	0	1.78	24.13

A repeat of the system described by Assis et al. [62], has been conducted. An $Fe - P$ 0.2 wt% alloy droplet of 17 mg ± 0.4 mg with a cylindrical input geometry of 1.19 mm H 1.49 mm D is used (the alloy has the exact same composition as used in the initial study, seen in table 6.3. This will be called alloy1 (a1). A master slag of the composition seen in table 6.2 (analysis via XRF) was prepared under shield gas argon in an induction furnace at 1873 K (1600^oC) from the stock materials, CaO, SiO_2, MgO, Fe_2O_3, and $Ca_2P_2O_7$; this will be called S2.

The second set of material used consists of a 2 mm diameter iron wire supplied by Alfa Aesar, cut into disks using a low speed diamond blade saw. This will be

Table 6.3: ICP detected chemical composition of Fe- alloys used in this study.

	$\%Mn$	$\%P$	$\%Ni$	$\%Cr$	$\%Al$	$\%C$	$\%S$	$\%O$	$\%N$
a1	0.011	0.201	0.003	0.002	0.002	0.0008	0.0012	0.0737	0.0005
a2	0.0003	0.0004	0.0001	0.0003	0.0005	0.004	<0.001	0.0034	<0.001

called alloy 2 (a2), the composition of which can be seen in Table 6.3. The weight of the resulting disks was between 14 and 16 mg. A master slag for this was prepared with the same reagent grade powders as previously stated inside an MgO crucible, melted at 1873 K (1600^{o}C) for 2 hours in a tube furnace under high purity argon to ensure homogeneous mixing. The crucible was then ground, slag pulverized, and analyzed via XRF (the composition can be seen in table 6.2). This will be called S3. A further slag composition was created in the same way to be in near equilibrium with a2 with respect to oxygen partition; this slag will be referred to as S4 and the composition is seen in Table 6.2.

6.3.2 High-Temperature Confocal Scanning Laser Microscope

MgO crucibles (9 mm inner diameter and 4.5 mm height) were packed with 0.45 g ± 0.06 g of the respective master slag. The crucible was then loaded into the HT-CSLM, and the chamber was cycled 3 times for ten minutes each through vacuum and argon backfilling (99.9999% argon). The slag was pre-melted at 1898 K (1625^oC) for 30 seconds and then cooled at a nominal rate of 1000 K min^{-1} with helium gas. The crucible was then removed from the chamber and a droplet ass loaded into the centre of the slag meniscus surface. A further 0.15 g ± 0.042 of slag powder is hand pressed on top to ensure the droplet gets submerged when in liquid state. The entire sample was reloaded, cycled 3 times again, and the experiment is then run following the regime shown in Table 6.4, under 200 ml min^{-1} argon flow. Steps 1 and 4 are required to reduce the chance of damaging the bulb.

Table 6.4: Heating and quenching regime of all samples. ## being the period of time a sample was held at high temperature for.

	Step 1	Step 2	Step 3	Step 4
Temp (K)	Rt-373.2	373.2 → 1873.2	1873.2 → 773.2	773.2 → Rt
Heating Rate (K min^{-1})	50	500	-1200	-300
Hold Time (s)	45	##	70	-

This was the same for all systems apart from that of S4, where a sapphire crucible was used in order to increase scattered light detection, giving a way to effectively increase the depth of focus field for the UV laser.

6.3.3 X-ray Computer Tomography

Samples containing S1 and S3, were scanned using a 'Nikon Metrology XT H 320 LC' XCT scanner and samples containing S2 and S4 were scanned using a 'Zeiss Versa 520'. The difference in machines was due to the availability during experiments, with the Zeiss preferred due to its better signal-to-noise ratio within images. This arises from different source and detectors within the systems, and a smaller source/detector distance in the Zeiss machine that is better suited for higher-resolution tomography.

The Nikon machine consists of a 225 kV micro focus with tungsten reflection target and a flat panel detector consisting of 2000 x 2000 pixels, each of 200 microns in size. The Zeiss machine has a 160 kV micro focus source with an alumina transmission target and charge-couple device-based detector 2000 x 2000 pixels, with a size dependant on the optic used (90.4 optic was used in this study with 1.75 micron pixel size).

The parameters for each scan are shown in Table 6.5. The scans were then reconstructed in proprietary packages included within the systems that use filtered back projection. The reconstructed 3D volume was then evaluated in 'VGStudio MAX' (Volume Graphics GmbH, Germany). Further information on the XCT scanning including reference pieces used for scaling, determination of the droplet isosurface, and validation of the scanning parameters can be found in previous works [62] [81].

6.3.4 Chemical Analysis

In order to evaluate the phosphorus content in the metal before and during emulsification for system 1 samples, WDS-SEM, LA-ICPMS, and SIMS were used. Each of these techniques has the advantage of having small spot sizes which make it possible to chemically analyse the metal drop and emulsion.

WDS-SEM was the initially selected tool to analyse the phosphorus content in the metal drops as it is a non-destructive technique and relatively simple to use. WDS offers better peak resolution and separation than EDS and can potentially

Table 6.5: Parameters used within the two scanners. * There is an additional focusing step performed by an optic in the Zeiss machine, where x0.4 was used in this study.

	Nikon	Zeiss
Voltage (kV)	220	140
Power (W)	3.1	10
Exposure	4	3
Projections 3142 3142		
Filter (mm)	Cu 0.5	CaF_2 1.0
Magnification	x39.5	*x6.69
Voxel Size	5.06	4.90

detect concentrations below 1 wt% with the usage of proper standards. Unlike EDS, the detector reads and counts X-rays generated of a single wavelength at a time that are diffracted by a crystal of proper lattice spacing. In the present study the standards used were pure Fe and GaP for iron and phosphorus, respectively. Each of the standards were used to standardize accelerating beam voltages of 25 and 30 kV with spot sizes of 6 and 7 microns. The high accelerating voltages and bigger spot sizes were necessary in order to achieve the highest beam current possible in the SEM, which helps in quantifying low concentrations.

LA-ICPMS differs from regular ICP-MS in that it uses a focused laser beam to ablate a small area of the sample. This technique was used to confirm the data acquired by WDS and only one sample was analysed via this technique. A total of four measurements were taken using ICP-MS across different regions of the metal drop. Each “shot” ablated roughly 5 μm in depth with a spot size of 100 μm in diameter.

SIMS was used for the analysis of oxygen in the 20-second sample. SIMS uses a focused ion beam to sputter the surface of the sample. As the ion beam mills the surface, secondary ions are generated and these ions are analysed by a mass spectrometer. Quantification was based on a stainless steel 302 standard.

6.4 Results and Discussion

The interaction of metal droplets with slag has been interrogated via the CT scanning of quenched samples produced in the HT-CSLM. The first series reported by

Assis et al. [62], has now undergone initial chemical analysis of representative sectioned surfaces (a1 and S1). Secondly a repeat of these initial conditions has been completed to interrogate the consistency of the previously reported tomography results (a1 and S2), as well as further samples taken in the period before emulsification to give insight into the pathway of the droplet breakup. Thus these experiments are very similar and both will be referred to as system 1. As a result of the initial chemical analysis of system 1, a low phosphorus system has been created and analysed to investigate the true cause of emulsification (a2 and S3, system 2) in the previous works. Finally a system at near equilibrium has been inspected via in situ imaging in the CSLM (a2 and S4, system 3).

6.4.1 The Pathways of Emulsification

XCT scans of quenched samples for a system (system 1) have been reconstructed to produce images seen in figure 6.1. It can be seen from figure 6.1 that emulsification of the droplet in S2 has occurred.

Several points should be taken from these initial images that display significant differences from the original study. Firstly, the holding times of these samples cross over, and extend beyond that of the originals (0 to 120 seconds). This is most likely because the repeat samples were run on a different HT-CSLM by a different user; this resulted in a diverted regime, where it was found that the droplet was taking longer to melt than seen before. At 90 seconds the sample is molten with a spherical geometry and the surface can be seen to have begun to roughen, either through the starting of initial emulsification, or due to the shrinkage of the droplet in an uneven manner during quenching.

The next observation is the pathway of emulsification to coalescence is seen to differ significantly from previously reported. This is thought to be due to the slower heating rates seen within the new samples. A slower heating rate will have caused slag and metal to become molten at a greater time separation. This will potentially reduce the initial driving force of partition equilibration, as material will begin to exchange before the droplet is fully molten. Due to this slower heating rate and the need to hold material at high temperature for longer periods of time, the amount of droplet dissolved into the slag could greatly increase. There are two proposed pathways for the new samples in system 1:

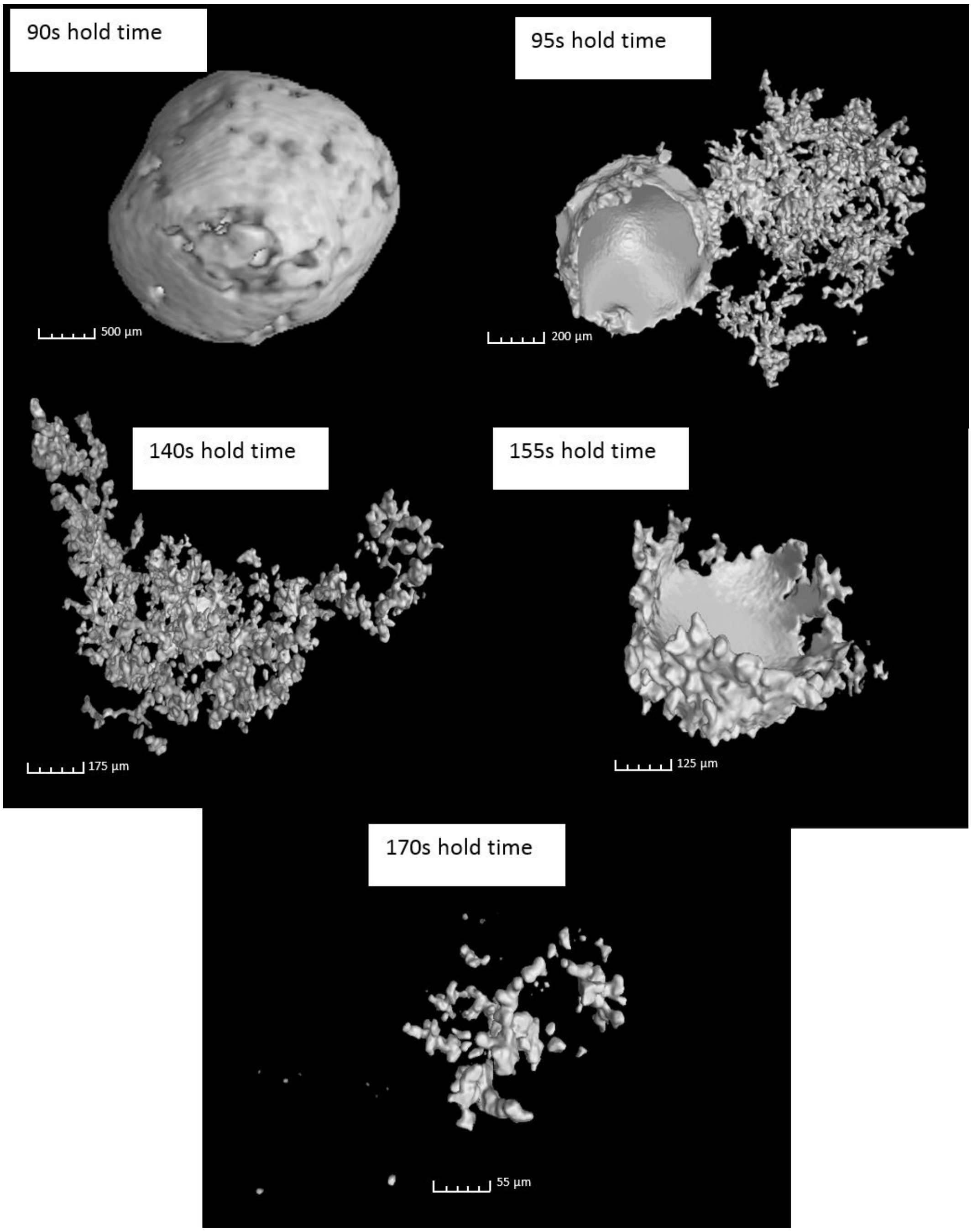

Figure 6.1: Reconstructed images from XCT scanning, showing only the metal fraction of the sample

1. The droplet reaches molten state slowly, with initial refining taking place (90 seconds), emulsification begins with half the droplet breaking away (95 seconds), the remaining sample continues to emulsify (140 seconds), and then coalesces (155 seconds). Finally the sample continues to be dissolved into the slag, reducing the visible material (170 seconds).

2. Up to 90 seconds the same behaviour, full emulsification where some of the sample pools back together due to gravitational effects through porous areas (95 seconds), emulsification continues through to 155 seconds (with pooling due to porosity in the slag happening in 110- and 155-second samples). Finally after 170 seconds large amounts of the sample have either dissolved or dispersed below XCT resolution.

The pooling theory is due to the orientation of the half-domed sections of the sample, where the cup faces upwards, and has large areas of porosity seen above (see figure 6.2). Any emulsified material here would have dropped (have no support to be separated) under quenching conditions.

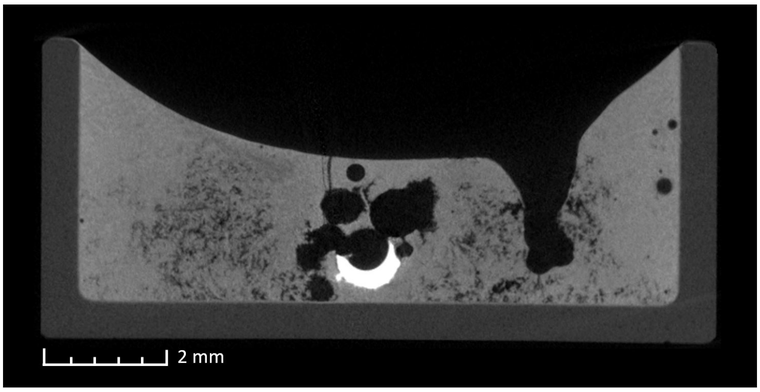

Figure 6.2: 2D slice of 95 second sample showing the orientation of the domed part of the sample

Finally it can be observed that a large amount of material is being lost throughout the reaction (briefly mentioned in the previous point). At this stage, the two options are either emulsification beyond the resolution of the current XCT scans, or dissolving of the $Fe - P$ droplet into the slag medium. It is believed that the 155-second sample is coalesced, and due to the relatively high holding time of 170 seconds significant amounts of dissolution is the most plausible result. In the future higher-resolution XCT scanning and SEM imaging will be used to investigate the presence of smaller particles. XRF analysis of the slag may also be carried out to investigate if the Fe content has increased.

6.4.2 Chemical Analysis of System 1

The expected reaction in system 1 is:

$$5(FeO) + 2[P] \rightarrow (P_2O_5) + 5[Fe] \tag{6.1}$$

where the material in () is in the slag, and those in [] are in the metal droplet.

As previously mentioned WDS-SEM and LA-ICPMS were used for phosphorus analysis while SIMS was used for oxygen analysis. A total of 5 shots were made close to the centre of the metal drop. Each shot milled roughly 10 μm in depth with a spot size of 30 μm. A sixth oxygen measurement was performed using SIMS to generate a depth profile of the oxygen concentration. This profile was obtained by milling from the centre of the cross section of the droplet towards the interface of the droplet. This profile is shown in figure 6.3. The summary of chemical analysis carried out by each technique is shown in table 6.6.

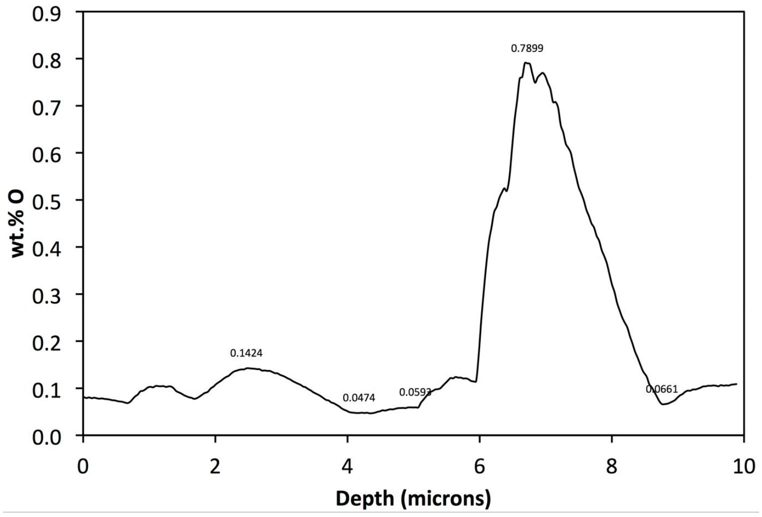

Figure 6.3: Measured oxygen concentration as a function of depth into the 20s sample (using a cross section) from Assis *et al* [62]

Table 6.6: Summary of chemical analysis performed using the various techniques described

		(wt.% P)			(wt.% O)
Reaction Time (s)	ICP-MS	WDS-SEM	LA-ICPMS	LECO	SIMS
Original alloy	0.201	0.170±0.032	-	0.0737	
0	-	0.179±0.015	-	-	-
10	-	0.002±0.002	-	-	-
20	-	0.008±0.005	0.0019±0.0001	-	0.213±0.139
30	-	0.003±0.002	-	-	-

The results mapped against the previously reported surface area profiles of the samples (Ai/A0) show that phosphorus had been removed from the droplet before 10 seconds of reaction time (see figure 6.4). This was much sooner than the first visualization of emulsification in system 1, at 30 seconds. This leads to the conclusion that phosphorus exchange across the interface is not the reason for emulsification to occur, and the equilibration time for phosphorus between metal and slag is much shorter than the ideal predicted time of 120 seconds calculated previously [62].

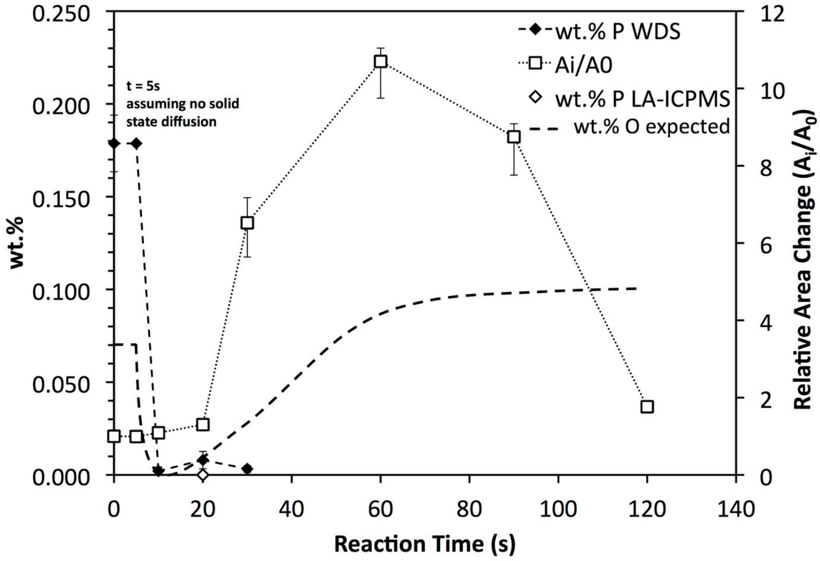

Figure 6.4: Expected oxygen concentration profile as a function of reaction time (LA-ICPMS only available at 20s)

SIMS results show a large increase in oxygen concentration within the droplet at 20 seconds, as compared to the initial alloy (whose oxygen analysis was outsourced to LECO). The $Fe - FeO$ equilibrium based on the activity of FeO in the master slag has been predicted using FactSage, giving oxygen equilibrium content within the metal of ∼1000 ppm. This coupled with the calculated reduction in oxygen early on due to reaction with phosphorus gives the predicted oxygen content as a function of time mapped in figure 6.4. SIMS analysis showed an average oxygen content of 0.213 ± 0.139 wt%, significantly higher than the predicted equilibrium. Figure 6.3 also shows the heterogeneous distribution of oxygen radially through the droplet, with values from below equilibrium to those much higher. SIMS does not offer quantified data, however it should be within a factor of 2 when appropriate standards are used.

From the points mentioned above, it is hypothesized that the exchange of oxygen across the metal/slag interface is the cause of emulsification. It is not known what would cause the mass oversaturation of oxygen within the droplet, however the mass transfer of oxygen back into the slag to reach equilibrium between 20 and 30 seconds, would be rapid. This along with the known fact that oxygen is a surfactant in a metal/slag system, leads the authors to the presented hypothesis.

In addition to the material presented, it was found that the cross-sectioned 0-second sample contained a dispersion of particles throughout the droplet (see figure 6.5). Local WDS of these particles showed them to be significantly higher in phosphorus than the bulk material (from 1.7 to 3.1 wt% P). These particles were not seen in the cross-sectioned images of later samples, where the phosphorus levels were seen to be drastically reduced (10 seconds onwards). Several images of the particles were used to calculate an area fraction of 0.4%; with this and the average particle concentration the amount of phosphorus removed is still significantly greater. It is possible that the phosphorus was held in a phase which was immiscible or did not melt at the same stage as the main bulk droplet; if this was the case, the high phosphorus phase may have been removed on the macro scale through particle migration from the bulk liquid to the droplet surface. Thus mechanical features rather than chemical reaction would be responsible for phosphorus removal. However, the challenges associated with the chemical analysis of oxygen and phosphorous need to be overcome before we can confirm whether the two reactions indeed can be separated. This requires further interrogation in order to define a realistic mechanism for phosphorus removal.

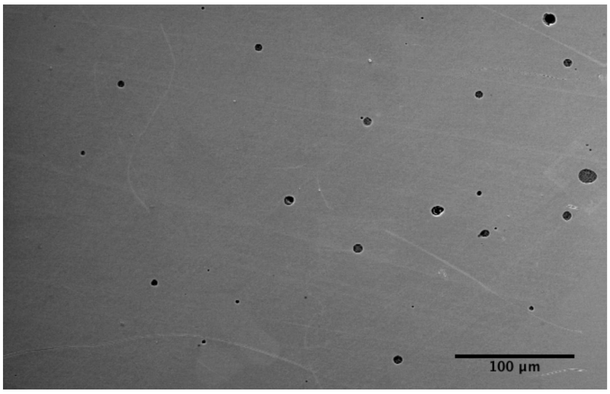

Figure 6.5: Low magnification SEM picture of 'P-rich' particles

6.4.3 System 2, Dynamic Changes in Surface Area

The expected reaction in system 2 is the electron exchange between ionic Fe and O in the slag to elemental Fe and O at the interface with the metal droplet:

$$(Fe^{2+}) + [O^{2-}] \rightarrow [Fe] + [O] \tag{6.2}$$

again where material in () is in the slag phase, and material in [] is in the metal droplet.

3D reconstructions of XCT scans performed on system 2 quenched samples are shown in figure 6.6. The initial sample of 10 seconds was selected as the starting point as this was when samples were shown to be fully liquid from system 1 [62] and used the same sample setup and user as previously, other sample times were selected in order to try and capture comparative emulsification data as to the initial study.

The surface area and volume of the droplets in system 2 samples were determined as described previously [62], the results of which are shown in tables 6.7 and 6.8, respectively. The min, max, and selected surface areas/ volumes are based on manual selection of grey values.

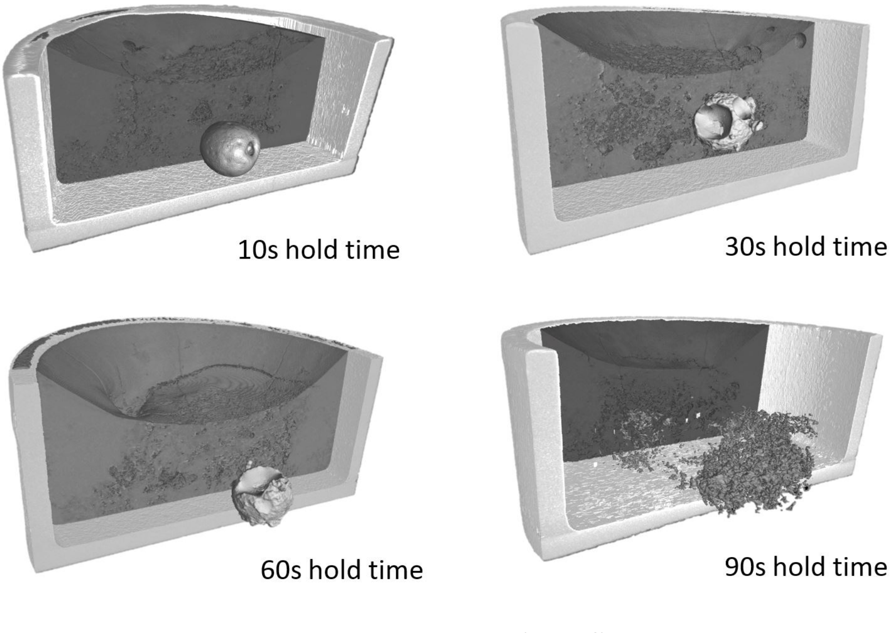

Figure 6.6: Metal droplet 3D spatial geometry for different holding times in system 2

The 10-second sample has melted and acquired a spherical shape, and emulsification takes place between 60 and 90 seconds. From table 6.7 the surface area of the drop stays relatively constant through the first 3 samples at 6 to 8 mm^2, followed

Table 6.7: Raw data for surface area measurements of system 3.

Time (s)	Surface Area Selected (mm^2)	Surface Area Max (mm^2)	Surface AreaMin (mm^2)	Ai/A0
10	6.60	6.60	N.A	1.00
30	8.37	8.38	8.36	1.27
60	6.84	6.86	6.83	1.04
90	65.75	73.69	58.13	9.96

Table 6.8: Raw data for volume measurements of system 2.

Time (s)	Volume Selected (mm^3)	Volume Max (mm^3)	Volume Min (mm^3)	Vi/V0
10	1.29	1.30	1.28	1
30	1.31	1.32	1.30	1.02
60	1.19	1.19	1.18	0.92
90	0.96	1.10	0.83	0.74

by an increase by an order of magnitude to 65.75 mm [47]. This increase in area is very similar to that seen in the previous study [62]; however there is a delay of ∼30 seconds. This is clearly seen in the normalized area curves displayed in Figure 6.7. In system 2, oxygen is transferred from the slag into the metal, and the result appears to validate the hypothesis of oxygen transfer across the interface being responsible for the spontaneous emulsification (the behaviour should occur regardless of oxygen transfer direction). The delay of 30 seconds, may be a product of the fact that no phosphorus exchange occurs in comparison to system 1, however it may also be due to aspects such as inconsistent heat transfer inside the HT-CSLM, or other parameters that affected the differences seen in system 2.

6.4.4 System 3, Validation of Chemical Exchange Causing Spontaneous Emulsification

A system designed with near equilibrium elemental distribution between slag and metal phases has been used to validate the hypothesis of chemical exchange across the interface being the cause of spontaneous emulsification.

System 3, notably has very low oxygen presence in the droplet (34 ppm) and zero FeO/SiO_2 in the slag phase (oxidation of Fe is thermodynamically un-

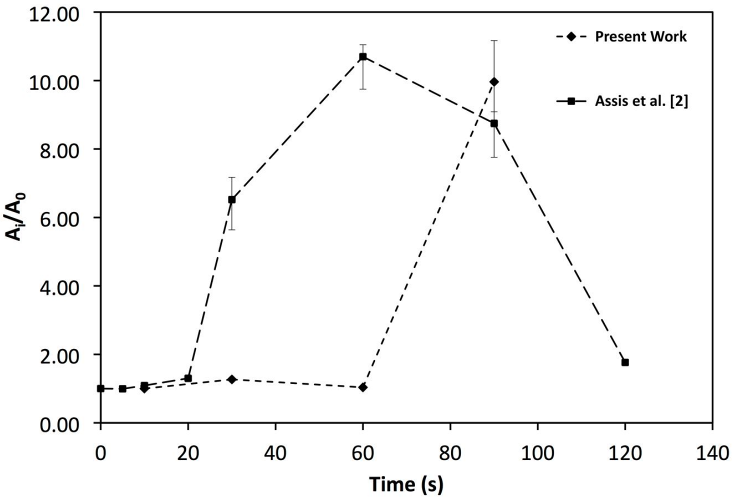

Figure 6.7: Normalized surface area of metal droplets as a function of time, for system 2 where oxygen from the slag enters the droplet, and system 1 where phosphorus from the droplet is being refined to the slag

favourable compared to all slag components).

It is known that thermal gradients across a medium can be a cause for spontaneous emulsification [60], and with the hot spot of the CSLM being ∼2 mm in diameter (smaller than the sample), and heat transfer being required from sample surface through the sample, it is unlikely the entire sample is constantly at the same temperature, especially during heating and during the early period of the programed isotherm.

System 3 being transparent in nature allowed for the in situ viewing of the droplet throughout a reaction profile. It was seen that the droplet appears to stay spherical in shape throughout the period of viewing, well past the previously reported emulsification times. Figure 6.8 also shows an XCT cross section of the entire sample, where the droplet is shown to be completely spherical and no Fe material was detected separate from the main mass of iron. This sample had a smoother surface than all previously reported samples not emulsified. The authors feel confident as a result that thermal gradients are not the cause of emulsification in this case.

6.4.5 Mechanisms of Oxygen Transfer into the Droplet

Due to the highly basic nature of the slags used in this study, it is likely a bi-layer would form at the interface with a cation and anion layering [99]. With this in mind, it is possible that a stabilizing interaction forms as the ions order into a favourable

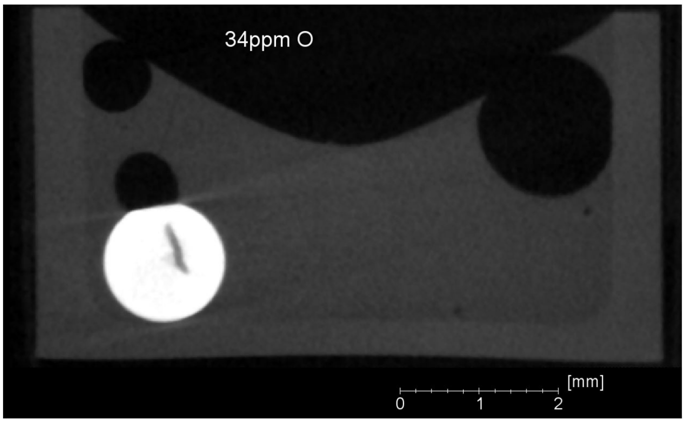

Figure 6.8: Ortho slice of CT scan of system 4 sample quenched at 90 seconds

geometry lowering interfacial tension through charge matching with electrons in the liquid metal (electro capillary formation). Although this can reduce the energy required for phase mixing in the systems, the observation of system 3 where a basic slag is also used gives evidence that electro capillary action is insufficient to allow spontaneous emulsification alone.

If the work of Sanfeld [100] is considered, stabilization of a phase or reaction in the bulk can be reverted due to either catalytic or reduced freedom (pinning of species) contributions through ordering at the interface of immiscible fluids. Hence it is proposed that the micro environment created by a bi-layer may allow for the disproportionation between ionic iron and oxygen at the interface, creating neutral species and allowing absorption into the non-charged liquid metal phase (as depicted for system 2), as opposed to the existence of stable O^{2-} and Fe^{2+} in the bulk metal oxide slurry. This process would still be governed by the mass transfer of material in the slag phase, however once ions enter the bi-layer the stabilization for disproportionation would still be present, and thus the formation of atomic O is possible with regards to equilibrium concentration between the two phases.

It should be noted however, that the formation of atomic species and transport through the interface would disrupt the ordering of any formed bi-layer and hence expectantly reduce the stabilizing effects it forms. Thus this destabilization should be accounted for when considering the driving force during active chemical exchange across the interface; an addition to the energy barrier for chemical exchange previously discussed.

A further mechanism is the use of the droplet as an electron carrier [70] [101].

If we account for mass transport of Fe^{2+} in the slag to be the rate-limiting step, a depletion of this ion at the surface is likely. As a result the reaction mechanism may take advantage of the metal droplet reach through the slag (through not only its large size compared to that of chemical interaction, but also the continued growth of perturbations penetrating new areas of bulk slag) and the fast transport of electrons through the liquid metal to reduce the kinetic constraints on oxygen uptake. The steps for this mechanism are as follows:

1. Anionic oxygen transport across the interface from slag into the droplet
2. Transport of electrons through the metal droplet to a site in contact with an iron cation
3. Transfer of the electrons to the iron cation to form an iron atom
4. Uptake of the neutral iron atom into the droplet

These steps can be expressed by the redox reactions:

$$(O^{2-}) \rightarrow [O][2e^-] \tag{6.3}$$

$$(Fe^{2+}) + [2e^-] \rightarrow [Fe] \tag{6.4}$$

where species in () are in the slag phase, and those in [] are in the metal phase. Where O^{2-} may be representative of a single oxygen ion or any reacting complex containing the ion.

This mechanism requires the movement of a charged oxygen ion into the non-charged metal droplet; this has a reliably large energetic cost and thus the concentration gradient is required to be large in order for this to happen at any meaningful rate. As such, this process may have a large influence early on in the experiment, however as the process continues it is unlikely that this mechanism could be responsible for the over saturation of oxygen seen from the SIMS results.

To interrogate these effects further, the authors propose experimentation with lower basicity slags, and electrochemical experimentation. By these methods it may be possible to isolate each effect and give quantification to its participation in the phenomena reported here.

6.5 Conclusions and Revisiting the Hypothesis

Chemical analysis of samples from a previous study by Assis et al. [62] appear to show that phosphorus movement across the interface between a metal drop and slag is not responsible for spontaneous emulsification. Instead it is proposed that oxygen partition in either direction across the interface causes a drop in interfacial tension through surfactant effects and active refining. This is supported by a system where only oxygen content was drastically away from equilibrium, showing similar behaviour to that seen previously (apart from a slight delay). This statement directly supports the interrogated hypothesis 3.

A replication of the previous study has also been carried out by another user with a different HT-CSLM. This showed very different melting times for the metal droplet and as a result a changed pathway of droplet morphology through the reaction period. Discussion has been given as to why these differences may have been seen, with heating performance, and sample preparation being the clearest possibilities. It has also been seen that prior to emulsification the droplet appears to show substantial roughening over the entire surface of the droplet, a link to the emulsification mechanism.

Although the availability of oxygen is integral to the phosphorus refining to the slag phase, the phosphorus appears to have completely equilibrated before emulsification occurs . This has however been potentially caused by a macroscopic flotation effect of phosphorus rich phases not entering the liquid matrix of the droplet. Hypothesis 4 requires further interrogation with a starting high phosphorus alloy where the phosphorus is within the bulk matrix.

With the cause of spontaneous emulsification now justified, the pathway by which this driving force causes emulsification must be considered. With a such study there presents a possibility to predict spontaneous emulsification.

Chapter 7

Quantifying the Pathway and Predicting Spontaneous Emulsification During Material Exchange in a Two Phase Liquid System

7.1 Hypothesis to be Interrogated

Hypothesis 5: "Spontaneous emulsification is initiated by perturbation and the potential this creates for reducing diffusion distance."

Hypothesis 6: "Spontaneous emulsification can be predicted from fundamental knowledge of the system."

With the knowledge as to why spontaneous emulsification occurs, the hypotheses above are presented to structure the interrogation of the emulsification physical pathway and present a method to model the behaviour.

7.2 Introduction

Reaction rates dependent on the interfacial area between two phases is an encompassing multidisciplinary expanse of study. The problem approach is imperative, as when diffusion in the bulk is rate limiting, the reduction in diffusion length offered by mixing of systems can drastically speed up the rate of a reaction. This results in higher efficiency and, if the necessary magnitude of change occurs, a different rate limiting step. This can often manifest as spontaneous emulsification (SE) [60] [102] of the species to form momentarily stabilized micro pockets of one phase dispersed through the other [62] [103]. Considering this, it is desirable to create a system with low interfacial tension, to allow the maximum sustained interfacial area. This can be aided or stabilized [104] through several mechanisms: bi-layer formation, induced charge gradients, surfactant addition and material exchange [86] [105] [27] [106].

In addition to classical areas [107] [108] [109] where interfacial breakdown is sought to reduce or remove a kinetic barrier or naturally occurring high-temperature reactions in geochemical systems, known systems where SE occurs can be utilized to produce desirable micro dispersions instead of traditional physical shear methods [58]. For example in silicon particle production [110], controlling the morphology of polymeric membranes [31] and even the formation of edible systems for controlled taste without affecting texture [111].

Mapping the transient interfacial area is key to understanding the rate of material exchange between two immiscible liquids, as well as controlling and predicting the phenomena such as the “tears of wine” or soap-aided spreading between hydrocarbons and water [59]. These are prime examples of how interfaces can behave in the presence of surface active species and physical influences causing a favourable increase in immiscible phase contact area. The authors hypothesise that the manifestations of these physical phenomena are controlled through the systematic growth, necking and finally budding (when SE is considered) of perturbations at the liquid-liquid interface. This cycle follows strict geometries controlled by the fundamental properties of the species such that the resultant geometries can be understood and predicted mathematically.

Here two systems are explored where the interfacial exchange of material is thermodynamically favourable and very fast in comparison to the mass transport of material in their bulk phases [67]. This situation is unusual in the lower temperature systems home to classical interface studies, where the reaction at the interface is often rate limiting. The systems being investigated consist of two immiscible phases, a molten metal and a molten oxide. Such systems are critical for extraction refining, casting and welding of metallic alloys. System 1 consists of a high-purity iron droplet and a high level of iron(ll) oxide in the molten oxide phase ($Fe - FeO$ system) to allow for quantification of the interface at varying stages of emulsification. The active reaction within this system is displayed in equation 7.1, and is of practical importance in the conversion of iron to steel during integrated steel manufacturing. System 2 uses a high-aluminium alloyed iron droplet and an enriched silicon dioxide oxide phase ($FeAl - SiO_2$ system) for in-situ observation of the emulsification's physical pathway. The active reaction is shown in equation 7.2. The latter is relevant for processing of low-density advanced high-strength steels for automotive components, but also has the convenience of study in the present discussion due to lack of transition metals in the oxide phase, making this phase optically transparent.

$$(FeO) \rightarrow [Fe] + [O] \tag{7.1}$$

$$4[Al] + 3(SiO_2) \rightarrow 3[Si] + 2(Al_2O_3) \tag{7.2}$$

where species in [] are present in the liquid metal phase, and those in () are within the slag phase.

The findings from these experiments and further input from the literature have been used to create a phase-field representation of the systems, where emulsification behaviour can be tracked and predicted through both chemical gradient mapping and graphical representation of the interface morphology. It is suggested while the reaction is occurring in these systems there is a chance the interface between the two phases perturbs. In addition, depending on the interfacial tension chemical driving force the system may break up into an emulsion to facilitate the faster dissipation of free energy.

7.3 Experimental

7.3.1 Materials

All molten oxide mixtures were prepared through powder mixing of reagent grade: CaO, MgO, SiO_2, Al_2O_3, $CaO.P_2O_5$, and FeO followed by pre-melting at 1873 K for 2 hours in a horizontal tube furnace with use of either MgO ($Fe - FeO$ system) or Al_2O_3 crucibles ($FeAl - SiO_2$ and null system). FeO was prepared through heating of Fe_2O_3 and Fe at 1273 K for 4 hours in a Fe crucible using a 99.9999% Ar environment (used for the mixture pre-melts as well). After pre-melting the oxide mixtures were then ground using a disk mill. Molten oxide mixture compositions were measured using XRF.

Samples containing the iron alloy of composition 0.0003% Mn, 0.0004% P, 0.0001% Ni, 0.0003% Cr, 0.0005% Al, 0.004% C, 0.001% S, 0.0034% O, <0.001 N, and slag of composition 36.89% CaO, 7.14% MgO, 16.21% SiO_2, 32.31% FeO_t, 1.65% P_2O_5, comprise the $Fe - FeO$ system. Experiments were conducted using high-density MgO crucibles.

Samples containing the iron alloy of the same composition as the $Fe - FeO$ system and slag with the composition 43.02% CaO, 8.74% MgO, 24.11% SiO_2, 24.11% Al_2O_3 comprise the null experimental system. Experiments were conducted using sapphire crucibles. Samples containing the iron alloy of composition 0.0002% Mn, 0.0004% P, 0.002% Ni, 0.0005% Cr, 7.87% Al, 0.0007% C, 0.001% S, 0.0038% O, <0.001% N and slag of composition 36.17% CaO, 23.11% SiO_2, 38.53% Al_2O_3 comprise the $FeAl - SiO_2$ system. Experiments were conducted using sapphire crucibles.

7.3.2 High-Temperature Confocal Scanning Laser Microscopy

A scanning UV laser is then used to view the sample while the experiment is conducted, recording at 15 fps with use of the HiTOS software package. A widening aperture function (inbuilt within the machine) was also used on the laser focusing to increase field of view in the z-direction (this reduces resolution in grey-scale accuracy when analysing the recorded video, this is the reason no size quantification is appropriate from the HT-CSLM images).

0.2 g ± 0.034 of molten oxide was loaded into a crucible. The mix was then pre-melt using the HT-CSLM, following the same heating cycle as shown in figure 7.6 with the 0-second hold. After cooling a metal cylinder of dimensions 1.19 mm H, 1.49 mm D weighing 17 mg ± 0.52 is added into the centre of the quenched molten oxide meniscus and a further 0.3g ± 0.12 of molten oxide is then added on top of the cylinder. This is followed by lightly compressing the powder by hand before the sample is loaded into the HT-CSLM for the experimental heating cycle. In the case of the null experiment system and the $FeAl - SiO_2$ system samples, a separate Pt and Al_2O_3 spacer are added to the underside of the crucible. The platinum spacer is used to increase reflected light through the sample, giving greater depth of vision in the HT-CSLM. The alumina spacer is present to stop sticking of the Pt spacer to the Pt sample holder. The chamber is evacuated using a rotary pump for 30 minutes and back filled three times. Experiments are run under an inert atmosphere of 99.9999% Ar passed through a further 623 K heated getter containing Cu and Mg chips.

Experimental times reported are normalized through determination of the molten oxide entering a fully liquid state, as viewed through the HT-CSLM video output. This time varied from between 5 and 25 seconds after reaching the programmed temperature of 1873 K. Reasons for this are expectedly due to variation in HT-CSLM performance, chamber maintenance, as well as effective interaction with the IR radiation due to differences in the sample surface topology (surface roughness for example [112]) and powder packing density.

7.3.3 Micro X-ray Computer Tomography

The samples were scanned using a ‘Zeiss Versa 520’, which has a 160 kV micro focus source with an alumina transmission target and charge-couple device-based detector 2000 x 2000 pixels, with a size dependent on the optic used. The machine has a cone beam X-ray source and a rotating turntable between source and detector.

The scanning parameters used were: voltage 140 kV, power 10 W, exposure 3 s, projections 3142, filter CaF_2 1.0 mm, magnification x6.69*, voxel size 4.90. The additional optical focusing used was x0.4.

The scans are then reconstructed in a proprietary package included within the systems that use filtered back projection. The 3D volume is reconstructed using a Feldkamp back projection method, creating a series of volume elements. The 3D volumes are then evaluated using ‘VGStudio MAX’ (Volume Graphics GmbH, Germany).

The surface area and volume of the iron pellet is evaluated by individual segmentation to determine the surface based on grey values, enabling selection of an appropriate isosurface. To ensure consistency the selected isosurface was automatically determined by the program through selection of sample voxels considered to be background (air) and the material (iron). Strong contrast in grey values between the oxide and metal fractions of the sample aided in the precise determination. Through this mechanism all measurements will be subject only to a consistent error across all samples.

To combat the inherent errors within XCT scanning (dependent on the given detector-source/source-object distance) a precision ball bar with a centre-to-centre distance of 5 mm is scanned. The results of the size evaluation of this can then be used to rationalize that of the experimental samples. Further information on XCT scanning parameter validation and development of the isosurface measurement can be found in previous works [62] [81].

7.3.4 Phase-Field Modelling

A phase-field theory of liquid phase separation coupled to fluid flow is employed for the current study. The respective Cahn-Hillard-type and Navier-Stokes equations are solved numerically. The interfacial free energy is assumed to be γ = 60 mJ m^{-2} [113]. The free energies of the bulk liquid phases are taken from the regular solution model. During the simulation the temperature was fixed. The time scale of the process is set by the interplay of melt flow and chemical diffusion [114] [115]. The equation of motion was made dimensionless using the length and time scale ζ = 6 x 10^{-6} cm, $\Gamma = \zeta^2$/D = 1.2 μ s, where D = 3 x 10^{-5} cm^2 s^{-1} and is the diffusion coefficient. The dimensionless time and spatial steps were chosen as $\Delta t = 1.25x10^{-7}$ and $\Delta x = 5x10^{-3}$.

7.4 Results and Discussion

In figure 7.1 a cross section of a quenched system at equilibrium (<34 ppm O_2 Fe droplet, with a slag containing no FeO) produced from X-ray Computed Tomography (XCT), an almost perfectly spherical geometry is found. Figure 7.2 is a series of stills taken from high-temperature confocal scanning laser microscopy (HT-CSLM) of the equilibrium system over a period crossing the emulsification times of both reactive systems. Very slight perturbation can be seen at times during the analysed recording, yet no individual wave shows sustained growth. Hazing and lack of distinction in the images is expected as the HT-CSLM is able to view a narrow vertical slice of an extremely dynamic 3D system, where the imaging light is also undergoing refraction when exiting the molten surface. Both the appearance of the spherical droplet identified through XCT scanning and the lasting placidity of the droplet viewed in-situ, give a standard behaviour against which to set the rest of our findings. The lack of emulsification shows temperature gradients and surfactant stabilization are unable to cause SE by themselves within the systems explored [86]. XCT images presented in figure 7.3 show only the metal proportion (light grey) of scanned samples produced from the $Fe - FeO$ system. From left to right (increasing in time after reaching 1873 K) a progression of emulsification is observed: the droplet has formed into a molten sphere on reaching temperature; perturbation begins on the droplet surface; the level of perturbation drastically increases and a small amount of material is seen to have separated; a gradually increasing portion of the droplet has entered a highly emulsified state (20-45 seconds); the entire sample has broken down to form a fully emulsified droplet (65 seconds).

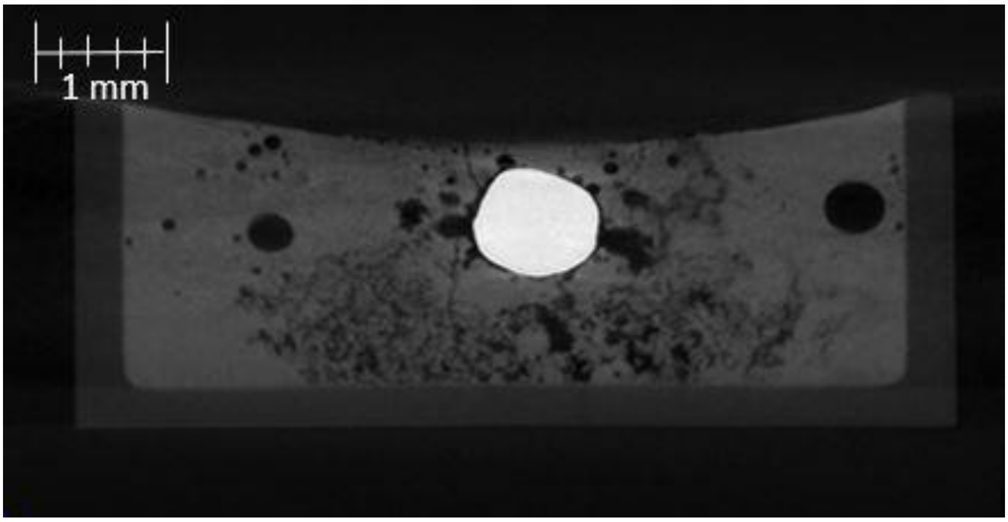

Figure 7.1: A 2D XCT reconstruction of a system at equilibrium, where the metal droplet is displayed in white, the slag in light grey, the crucible in dark grey and porosity as black ($3\mu m$ resolution scan).

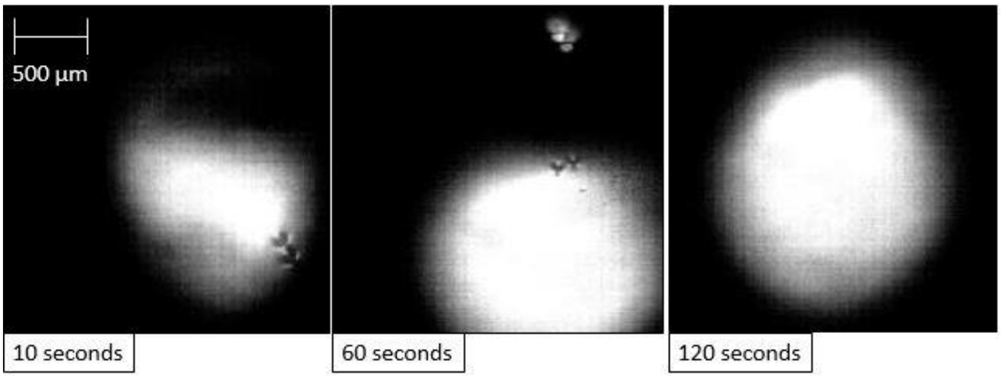

Figure 7.2: A three step sequence showing the quiescent droplet in the equilibrium system with time as imaged by the HT-CSLM through a transparent slag.

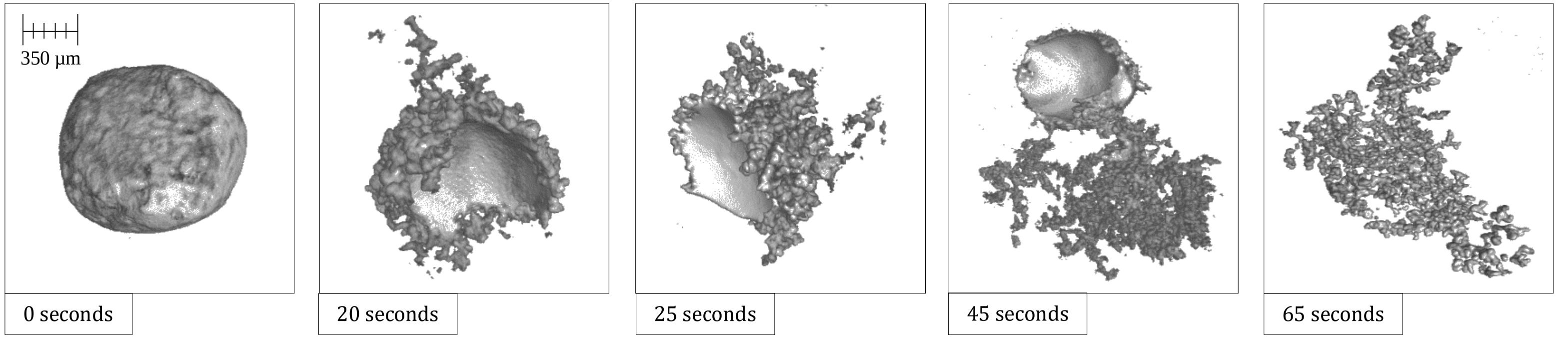

Figure 7.3: Reconstructed XCT images of the $Fe - FeO$ system quenched at defined times; only the metal part of the sample is displayed in light grey (3 μm resolution scan).

Figure 7.4 offers a qualitative view of the level of perturbation change between 20 and 25 seconds. The images at the top show the 20-second sample having a significantly higher area of the segmental perturbations in the darker blue end of the scale spectrum, as opposed to the 25-second sample where the image depicts on average a longer perturbation distance from the segmentation sphere and multiple perturbations at the very top of the length scale, above 400 μm in length. As the reaction progresses, perturbations grow due to sustained transfer of material between slag and metal phase; the lowering of diffusion distances through growth allows for the faster dissipation of free energy. The effect is an increase in perturbation size and overall interfacial area increase; the energetic cost of increased interfacial area must be outweighed by the free energy release [90]. The metallic material can be envisaged as being dragged into the perturbation by the expanding surface. This is quantified in figure 7.5 where the surface areas of the metal droplets from figure 7.3 are presented along with the expected change in surface area of the null experiment previously discussed. Here it can be seen that the increased perturbation level between the 20- and 25-second samples has resulted in a slight increase in surface area. The null experiment shows a slight reduction in surface area due to loss of material through oxidation and dissolution into the slag phase with time (modelled using FactSage^{TM}). Examples of heating profiles entered in the HT-CSLM for the experiments discussed are given in figure 7.6; the HT-CSLM was able to follow these profiles to within $\pm 10^{o}$C with the most deviation at the point of change between heating to reaction temperature (1873 K) and the isotherm.

Next the $FeAl - SiO_2$ system is considered, where in figure 7.7 a time-step HT-CSLM image sequence is presented of the system during reaction at low magnification. The droplet can be seen to increase in size followed by distortion and observation of perturbations. The material then spreads into a cloud covering most of the field of view before coalescence back to a near-spherical shape. Figure 7.8 shows the same reaction at higher magnification; the stage of SE can clearly be observed: random perturbation beginning; growth in both size and number of these perturbations; complete breakdown/clouding of the system over the entire image; finally coalescence of the system to a single near-spherical shape. Due to the speed of this reaction the droplet was unobservable from the very commencement of slag melting, as such the first image of Figure 7.8 shows slight perturbation already. Only

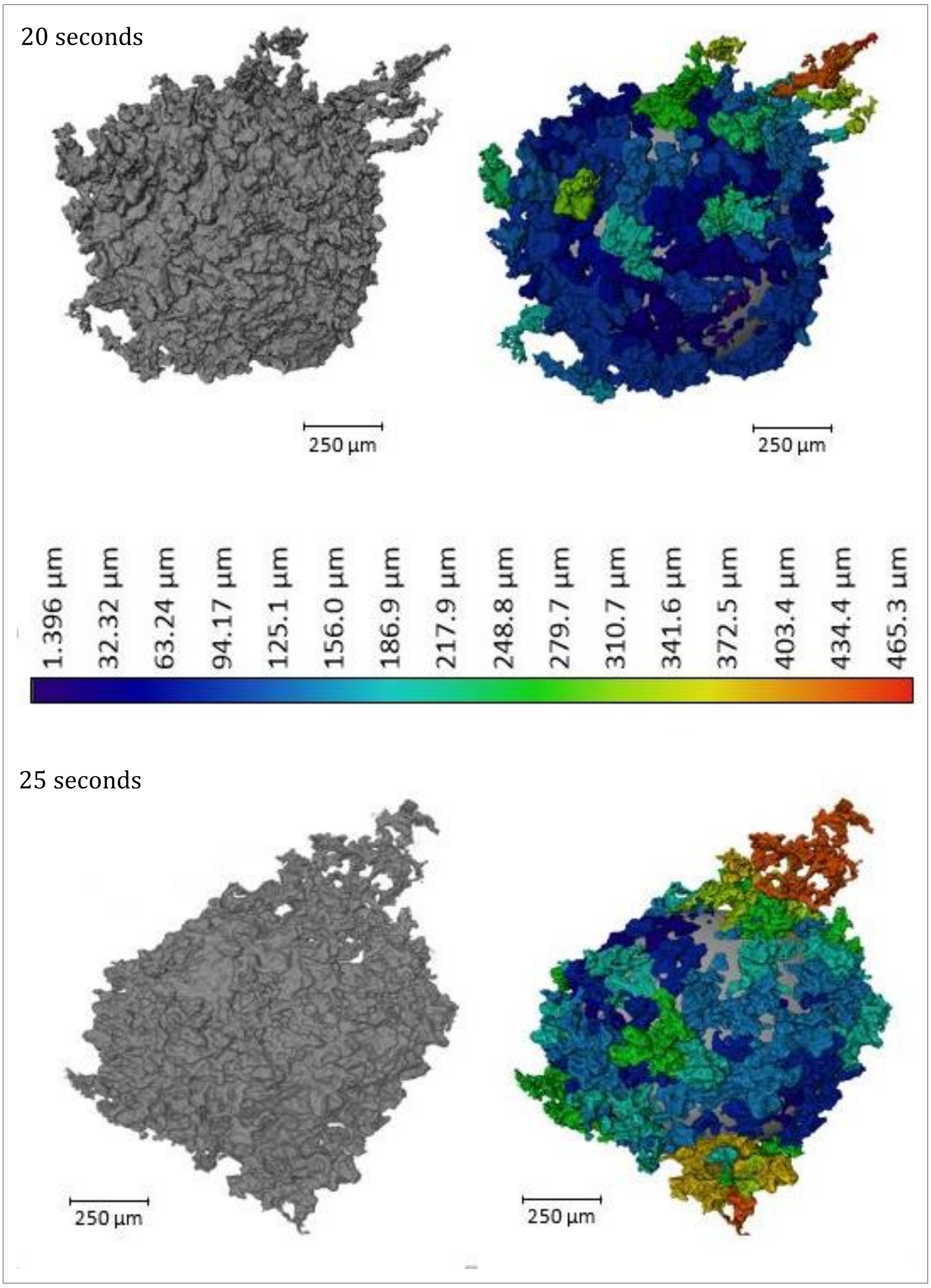

Figure 7.4: 3D reconstructions of the 20- and 25-second samples, with the addition of the segmented perturbations displayed in colour dependent on length of protrusion from the segmentation sphere.

the last image shows a smooth droplet similar to those seen in the null experiment which coincides with when the $FeAl-SiO_2$ system should have reached equilibrium.

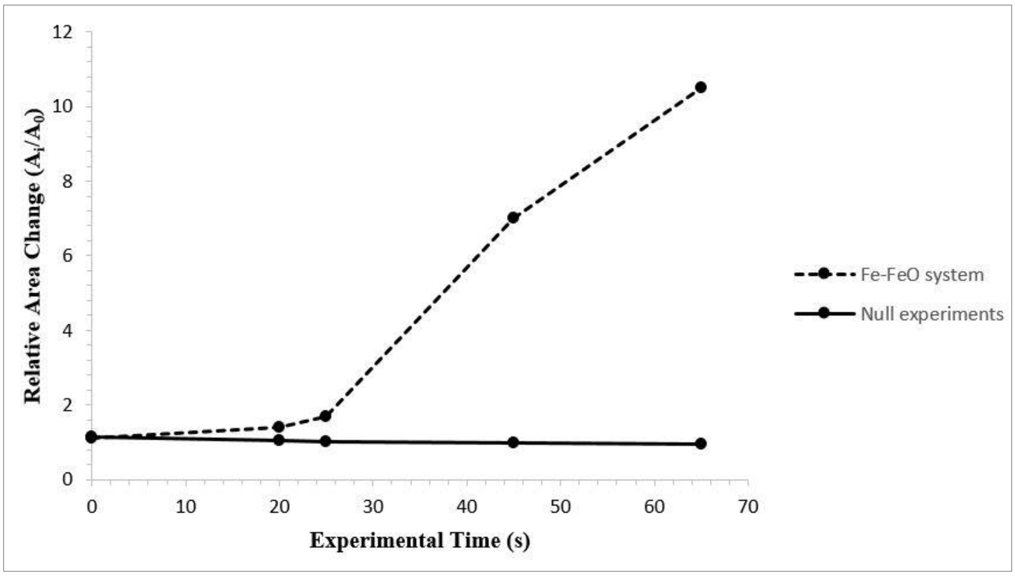

Figure 7.5: The quantified surface area of the metal droplet in the $Fe - FeO$ system with time from XCT analysis, along with the expected surface area of the null experiment assuming a perfectly quiescent sphere; the null experiment surface area reduces with time due to slight oxidation as modelled using the equilibrium module in Factsage^{TM}.

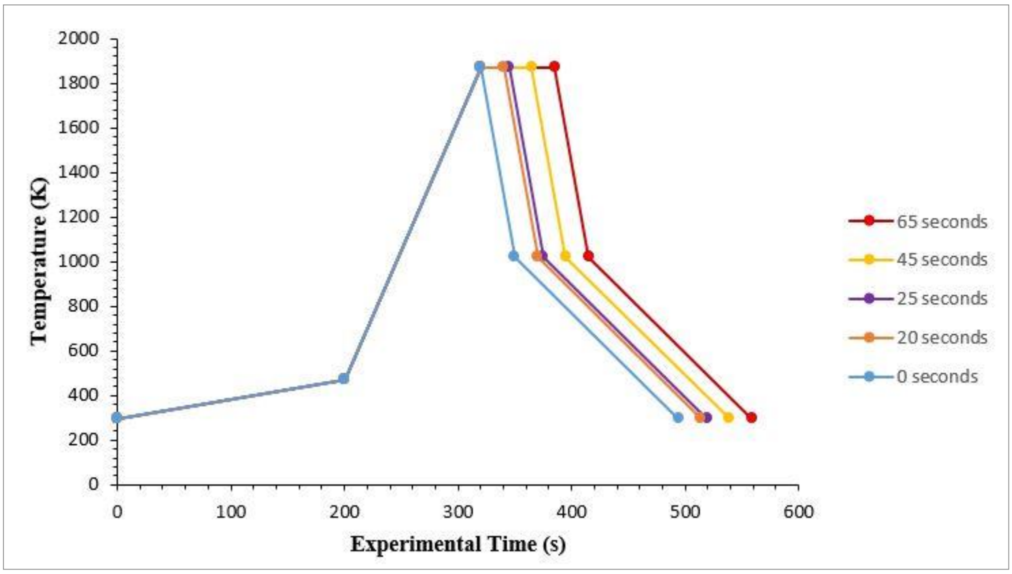

Figure 7.6: The programmed heating cycle of the HT-CSLM, showing a slow early heating regime and a quench point on cooling for protection of the equipment against thermal shock.

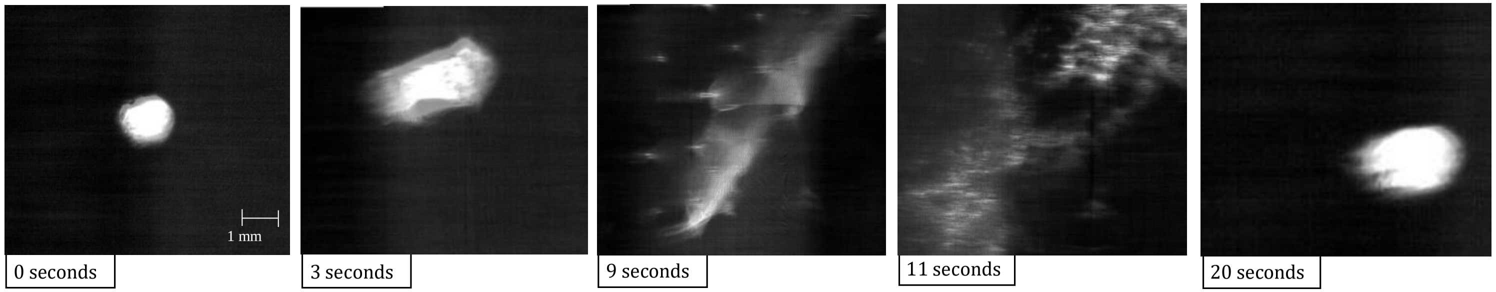

Figure 7.7: An image time step of the $FeAl - SiO_2$ system as visualised by the HT-CSLM at lower magnification; the droplet can be seen to grow in size, spread and perturbations are observable surrounding it, followed by dispersion into a cloud covering the field of view before coalescence.

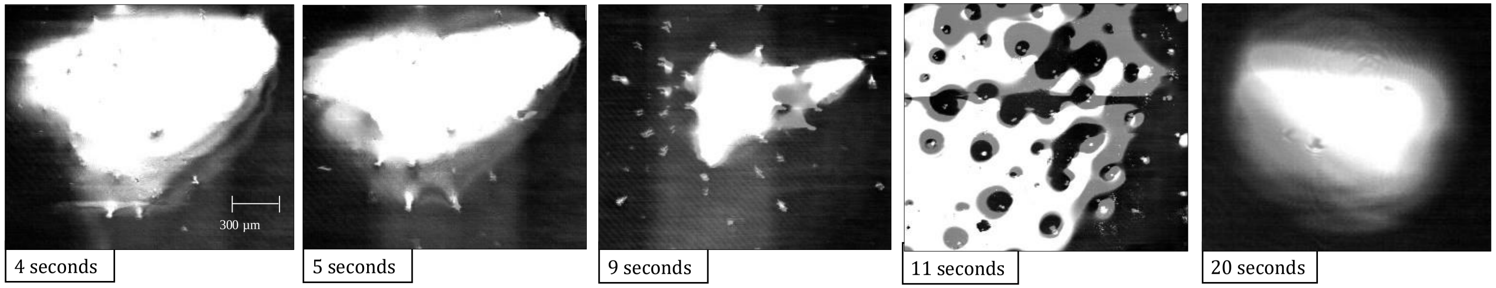

Figure 7.8: Emulsification visualization of the $FeAl - SiO_2$ system at higher resolution via the HT-CSLM. As noted in the main text, the HT-CSLM effectively views a 2D slice of the sample; this results in perturbations from lower in the sample appearing as a halo of in-focus white line or spots around the parent droplet such as seen at 9 seconds, this is also the reason the image at 11 seconds shows a continuous metal phase, as overlapping droplets will appear as one mass.

Quenched samples of the $FeAl-SiO_2$ system are displayed in figure 7.9 where the 15-second sample (the quickest time in which this sample could be captured with reduced cooling performance due to the experimental setup of this system) can be seen to have undergone significant coalescence. Yet there are still a large number of well dispersed smaller droplets throughout the sample. The 20-, 25- and 30-second samples show a reduced number and size of droplets outside the main coalesced body. The surface area and detected volume of metal in these samples has been added in figure 7.10, where it is clearly visible that the $FeAl-SiO_2$ system is coalescing and near complete equilibrium within the same time frame that the $Fe-FeO$ system begins emulsification to a significant extent. This shows significant differences in the rate of reactive species mobility in the systems, where the $Fe-FeO$ system is most likely dependent on the rate of mass transport of FeO through the slag phase, whereas the $FeAl-SiO_2$ system is likely dependent on Al mass transport in the metal phase [74] [75].

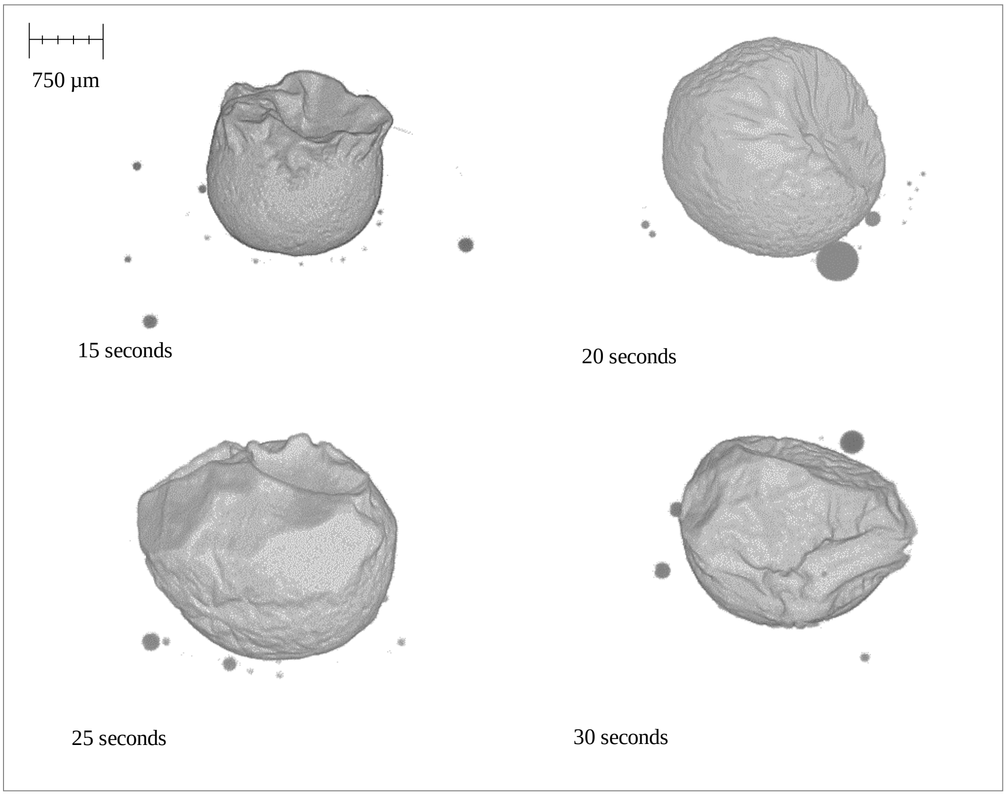

Figure 7.9: 3D reconstructions of the quenched $FeAl-SiO_2$ system where the crucible and slag phases have been removed to expose the metal phase of the sample in free space.

The classical Fick's law which is generally known for explaining the diffu-

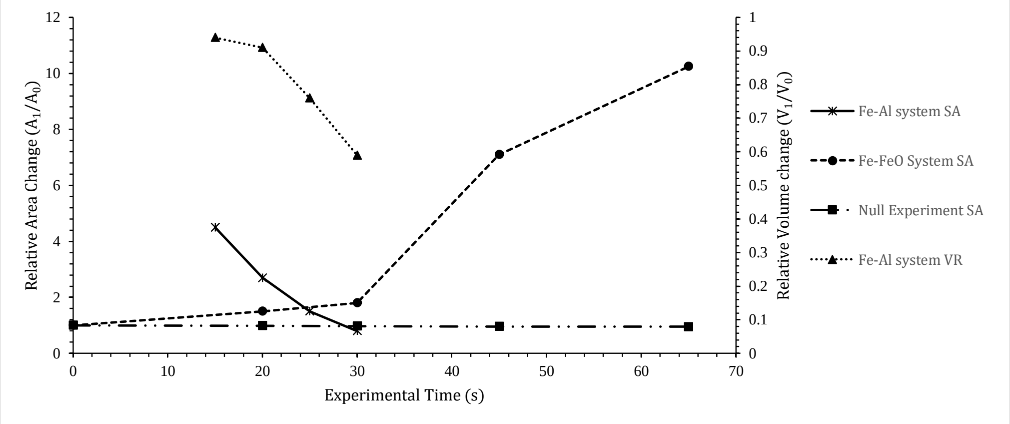

Figure 7.10: A graphical representation of the surface area change of the $Fe - FeO$ and $FeAl - SiO_2$ systems as measured through XCT, as well as the volume change of the $Fe - Al$ droplet mass with time and the modelled surface area change within the null experiment.

sion process, does not explain interpenetration of molecules through liquid-liquid boundaries within a horizontal capillary [27]. The grounding knowledge from these experiments is used to inform the practice of phase-field models in both 2D (for the $Fe-FeO$ system) and 3D (for the $FeAl-SiO_2$ system) with the inclusion of Navier-Stokes solutions. Figure 7.11 shows time-step images from the 2D $Fe-FeO$ system where the droplet can be seen to go from the starting quiescent sphere through levels of perturbation; at $t^* = 70,000\ \delta t$ material can be seen to have necked and broken away from the parent droplet beginning the emulsification process. Figure 7.12 shows 3D images of the modelled $FeAl-SiO_2$ system where again a similar progression in time can be seen. The model goes further than that of system 1 to view a highly emulsified state at $t^* = 38,500\ \delta t$ and culminating in a coalesced droplet at the final 70,000th time step. Both models show a clear pathway of emulsification, which supports that seen in the in-situ HT-CSLM experiments. This defined staged pathway is further developed through the use of figure 7.13a and figure 7.13b where 2D ortho slices of the 20- and 25-second $Fe-FeO$ samples are shown. Perturbations are selected in the lifecycle from left to right of the image showing stages of growth in length → necking at a position between the main droplet and perturbation tip → divergent growth of a perturbation → break away with material retraction to the main body → and finally complete separation of an offspring droplet.

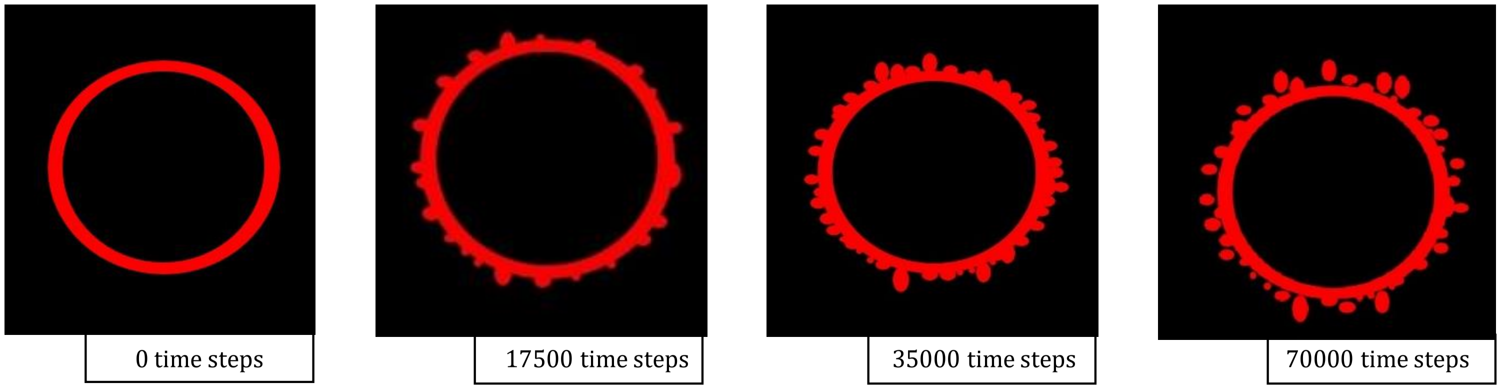

Figure 7.11: Selected graphical outputs from the 2D $Fe - FeO$ phase-field modelling showing the progression from a quiescent sphere to a highly perturbed state where material has begun to break away from the parent droplet.

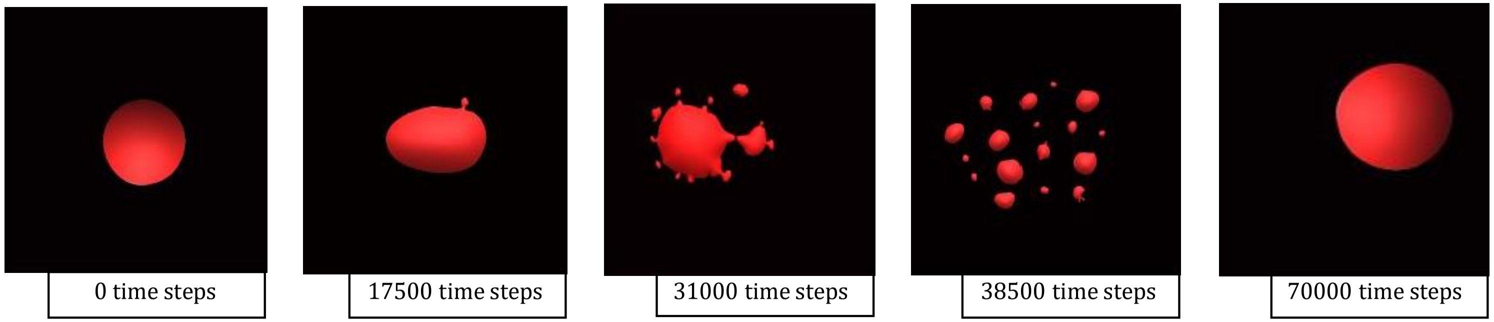

Figure 7.12: 3D graphical outputs from the $FeAl - SiO_2$ phase-field model, where the full life cycle of emulsification and coalescence can be seen within the simulated 70,000 time steps.

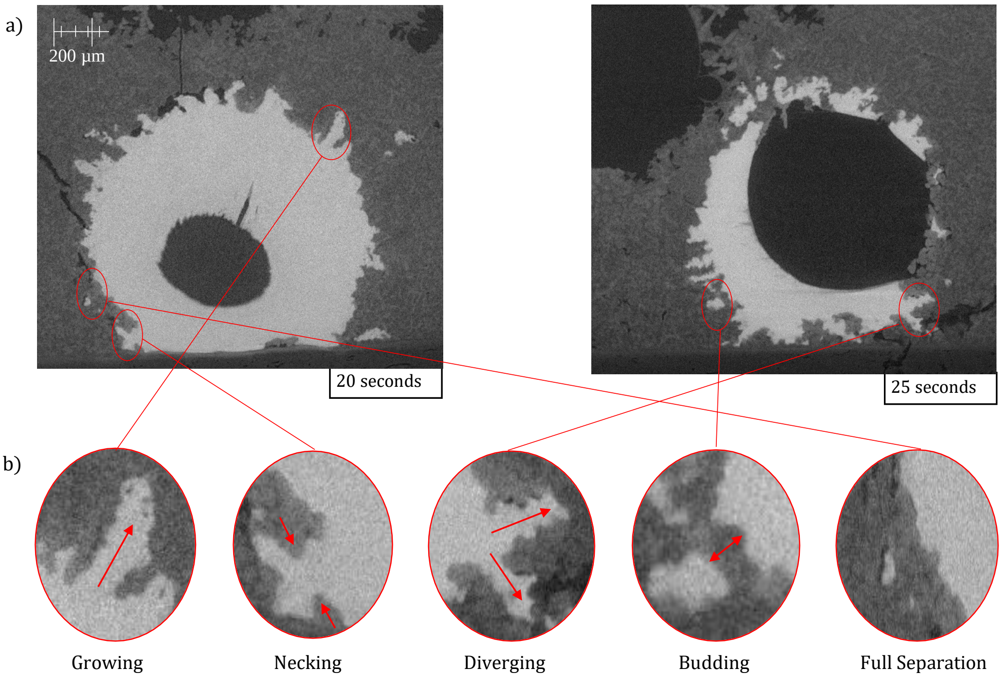

Figure 7.13: a) 2D ortho slices of the XCT 20- and 25-second reconstructions where the metal phase is in light grey, slag in dark grey and porosity in black. b) Magnified section of the 20- and 25-second ortho slice images where each growth cycle stage of a perturbation as identified from the phase-field modelling has been highlighted as present in the experimental samples.

The similarity between the patterns of behaviour observed for perturbations in both the experimental and modelling approach give strong validation of the models' driving forces. Equally the time-step images from the 3D phase field model and the in-situ HT-CSLM video of the same system can then be correlated. This offers a method to deduce the number of time steps in the model equivalent to a period of time in the high-temperature experiments. This results in 3,500 time steps being equivalent to 1 second. In figure 7.14 the culmination of the two experimental systems' interfacial area ratios where time has been converted to time steps is given, as well as the addition of both the $FeAl - SiO_2$ system and $Fe - FeO$ system interfacial area ratios computed from the phase-field model. From this it is clearly observable that both pairings have a high level of coherency between the modelled data and experimental measurement with several overlapping data points between each. Although there is slight deviation, this is expected to be due to temperature variation in the experimental method (under heating in the case of the $Fe - FeO$ system limiting diffusion rates, and cooling during the quenching of the $FeAl - SiO_2$

system reducing coalescence activity) compared to the innately held isotherm the model follows at 1873 K throughout the entire droplet reaction cycle.

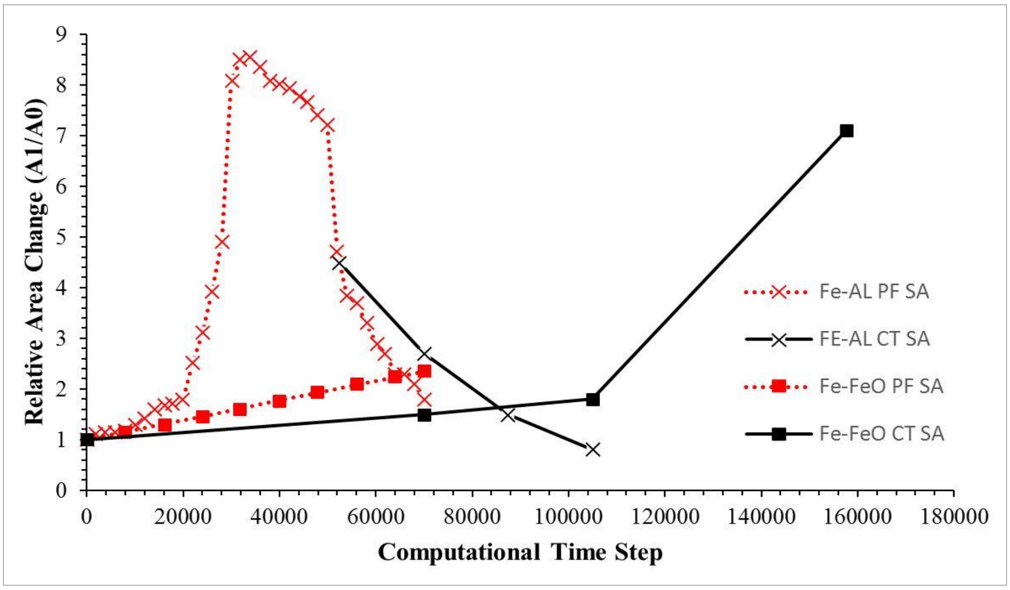

Figure 7.14: Graphical display of the transient surface area as measured via XCT for experimental samples and output geometries from the phase-field model; experimental samples have been time-step normalized through comparison of in-situ HT-CSLM with phase-field results.

Figure 7.15 and figure 7.16 show the individual perturbation measurements for both the 20- and 25-second samples where the maximum distance from a defined quiescent sphere is taken as the length, and the narrowest point of the perturbation is taken as the width. It is visible from the redline drawn at a 1:1 aspect in each graph that a large portion of the perturbations sit on or very close to this ratio. Due to the large number of perturbations in this aspect and visual inspection of the 3D images it is reasonable to propose that the “normal” growth of a perturbation is outwards from the droplet at the same rate as they grow in width on the droplet surface. It thus follows that perturbations away from this “normal” growth regime have begun the necking phenomenon by at least 700 nm (the resolution of measurement attained within these high-resolution XCT scans). Figure 7.17 offers examples of segmented perturbations as a result of the method described in detail in appendix 1. These images give an appreciation for the more complex geometries perturbations can uptake through phenomena such as diverging growth and interaction with physical forces such as mass fluid flow due to temperature gradients or surface interaction with gas. Further to this, micro shear forces will be in effect as a result of Marangoni flow for example [91].

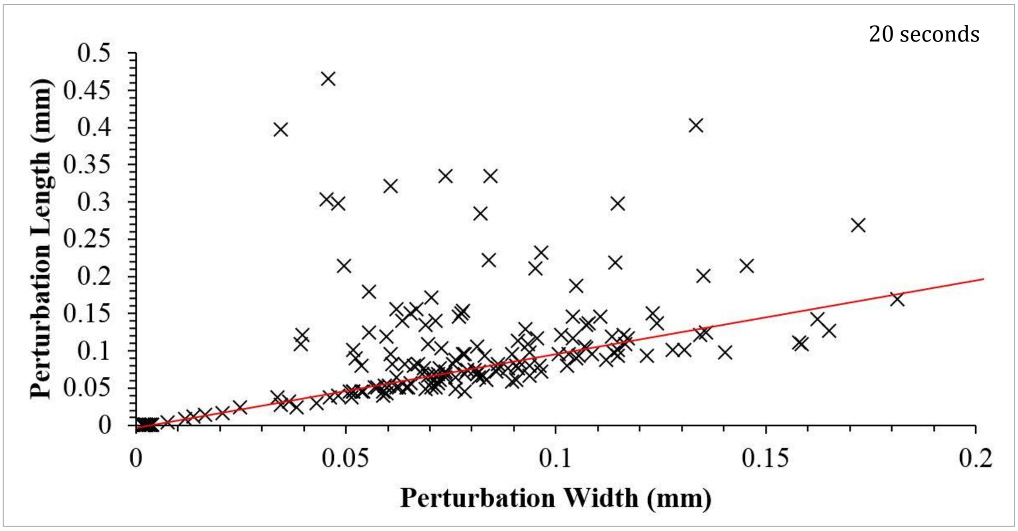

Figure 7.15: Perturbation dimensions for the 20-second $Fe - FeO$ sample.

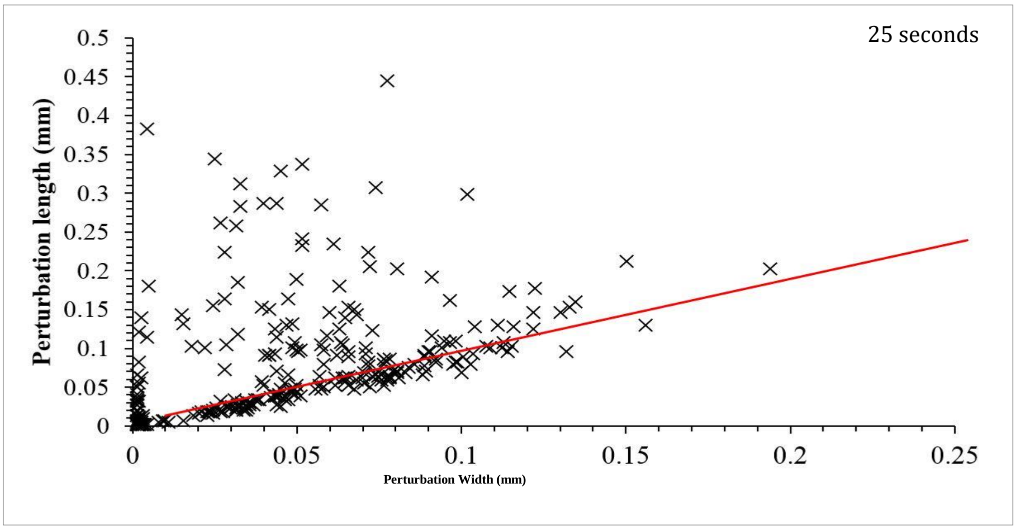

Figure 7.16: Perturbation dimensions for the 25-second $Fe - FeO$ sample.

Figure 7.18 shows the distribution of perturbations in the growth cycle for both the 20- and 25-second samples where the data has been truncated to represent roughly 85% of the total perturbations measured for both samples. This equates to a maximum height/width ratio of 2.3. Both samples show the largest proportion of perturbations to have a geometry ratio of 1:1 thus quantifying the previous observation when discussing the behaviour. However, it is clear to see that the 25-second sample has a reduced portion in this “normal” growth range compared to the 20-second sample, and a greater number at higher ratios where the width is

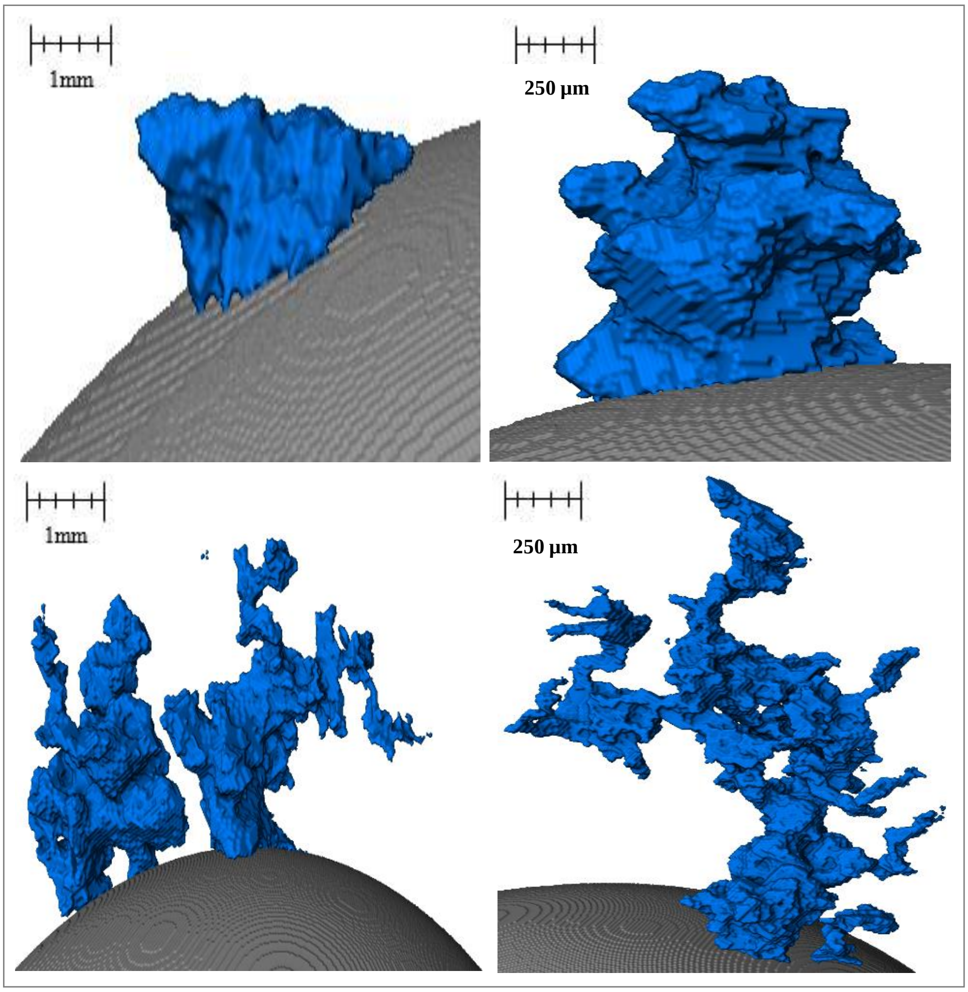

Figure 7.17: Examples of the perturbation geometries displayed in 3D space as produced via the XCT segmentation method implemented.

smaller than the length and thus a higher portion of the perturbations are within the necking stage of the cycle. Table 7.1 shows the base statistics of the perturbation measurements for both the 20- and 25-second $Fe - FeO$ samples as well as for a random measurement of 15 perturbations from the output of the 2D $Fe - FeO$ phase-field model. It is possible to rationalise the phase-field model scale through computation of the quiescent spherical diameter of the input 17 mg droplet, which can be coupled with the graphical output from the model at 0 time steps to offer standardization of measurement for the model's Cartesian space output. From the table it is apparent that both the average length and width of a perturbation has increased with time, however the maximum and minimum stay within close proximity. This indicates that a perturbation may grow to a maximum length of approximately

470 μm before material breaks away from the parent droplet, as well as a maximum width and length of near 200 μm before necking begins to occur (assuming the 1:1 “normal” growth regime). Hence it is suggested that the perturbation is likely able to double in length from the time necking begins to the time material breaks away; the acceleration of perturbation growth is an interesting prospect for further investigation. It should finally be noted from the Table 7.1 that the manually measured sizes of perturbations present in the 70,000 time step 2D $Fe-FeO$ modelled system are within close size proximity to those measured through XCT.

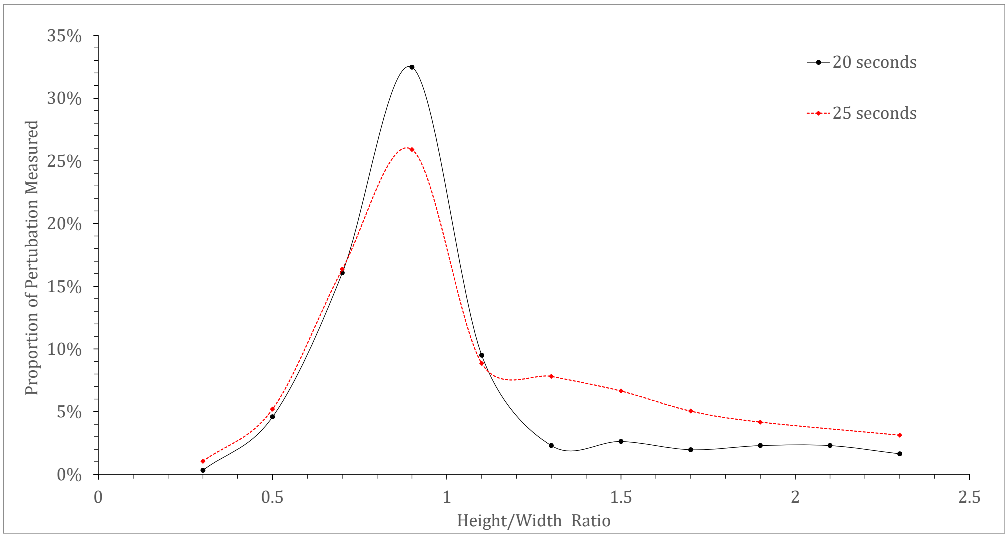

Figure 7.18: Perturbation height/width ratio distribution for the 20- and 25-second samples truncated to represent close to 85% of the total perturbations from each sample.

Table 7.1: Compositions of $FeAl$ alloys used for the experiments in HT-CSLM presented in mass %. Compositions were measured by ICP.

	Number of Perturbations	Statistic	Width (μm)	Length (μm)	Volume (μm^3)
20 Seconds	192 Detected	Mean Average	44.5	74.4	0.121
		Standard Dev	37.2	76.7	0.244
		Maximum	193.8	445	2.98
		Minimum	1.50	1.37	2.65 x 10^{-6}
25 Seconds	305 Detected	Mean Average	69.4	91.9	0.279
		Standard Dev	40.8	81.29	0.384
		Maximum	181	465	3.08
		Minimum	1.53	1.40	2.72 x 10^{-6}
70,000 Time Steps	15 Measured	Mean Average	47.0	79.0	-
		Maximum	202	457	-
		Minimum	<5	<5	-

With validation of the phase-field model through physical interrogation of its graphical expression as compared to the experimental observation and measurement, the exploration of mapping both the physical force and chemical distribution in the systems is possible. The dynamics of the 3D $FeAl - SiO_2$ system with respect to the stages of a perturbation's growth and separation from the parent droplet are possible to output from the model. Figure 7.19 maps the interfacial tension between the two phases with respect to geographical location. The surface tension is seen to be highest at the tip of the perturbation during growth, however when the perturbation reaches a certain size this tension reduces due to reduced curvature. At the same time a shift is visible of high surface tension to the necking area of the droplet, which as the neck increases in length becomes high enough to cause release of the budding section of the perturbation, relieving the highly constrained necking area to lower the surface tension overall.

The aluminium level within the sample can be viewed as a profile of depth into the metal droplet from the slag/metal interface, as well as in the perturbation compared to the bulk droplet in Figure 7.20. The model predicts a reduction in aluminium content radially outwards through the droplet, supportive of the mass transfer of aluminium being the rate-controlling step in this system. The high surface area to volume ratio within a perturbation presents a greater concentration gradient in this area of the droplet, pulling more and more aluminium from the bulk droplet into the perturbation. This is driven through the higher chemical gradient (faster than it would approach the surrounding quiescent interface) creating a higher concentration of aluminium in the "bulk" perturbation than in the surrounding surface of the droplet. Finally figure 7.21 shows the distribution of the normalized gradient of driving force including the chemical free energy and the interfacial energy within a drop. Although there is an increase in the number of reactive elements ejected into the perturbation; due to the increased curvature at the necking area, there is a larger gradient of driving force (similar to surface tension) in this area compared to the peripheral of the drop where the curvature is less as a result of the differences in the spacing between iso-concentration contours near the interface. After the separation, there is a uniform distribution of the gradient at the periphery areas of the original drop and that of the separated droplet and both systems evolve towards decreasing their interfacial energies (surface areas). This process continues until the

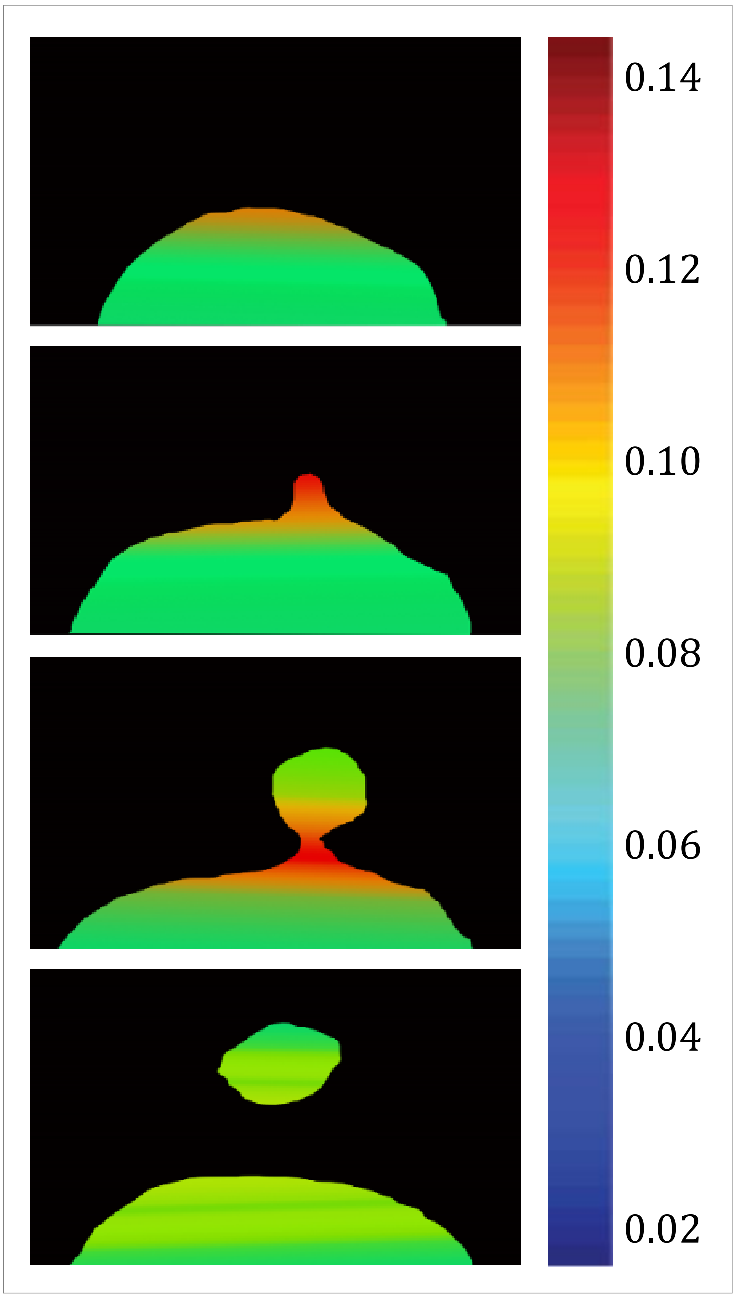

Figure 7.19: The computed distribution of surface tension through and in close proximity to a growing perturbation (t^*=15000, 20000, 30000 and 35000 δ t).

equilibrium state (chemical equilibrium as well as lowest possible interfacial area) is reached.

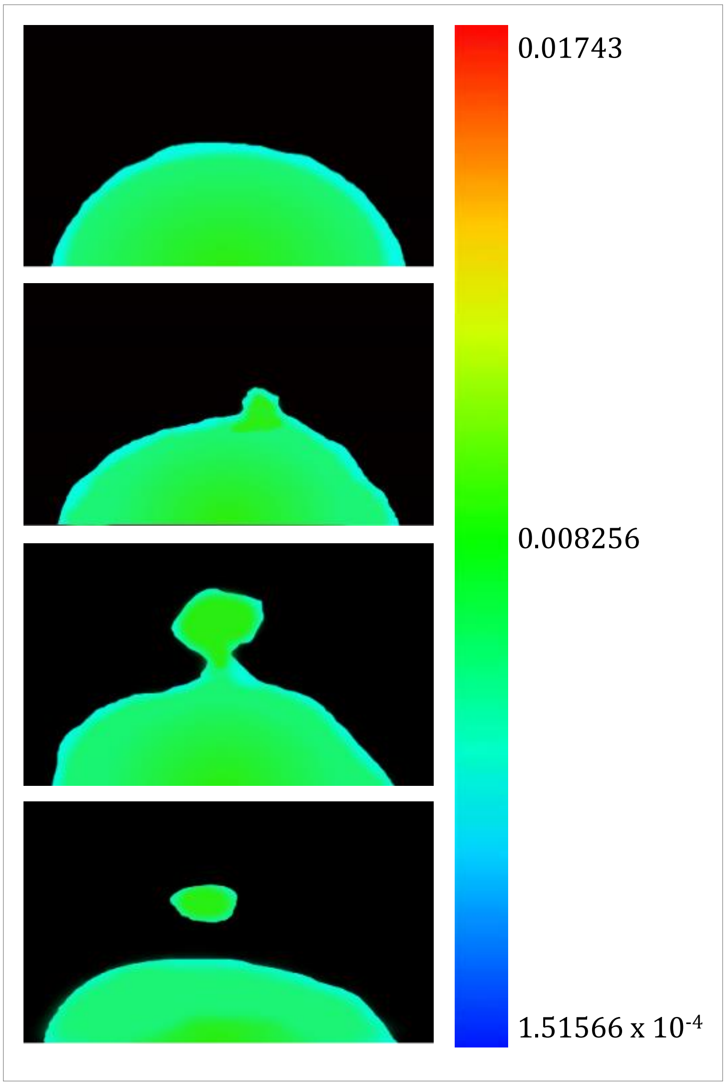

Figure 7.20: The simulated variation of chemical composition, specifically aluminium content as a distribution through the metal droplet (t*=15000, 20000, 30000 and 35000 δ t).

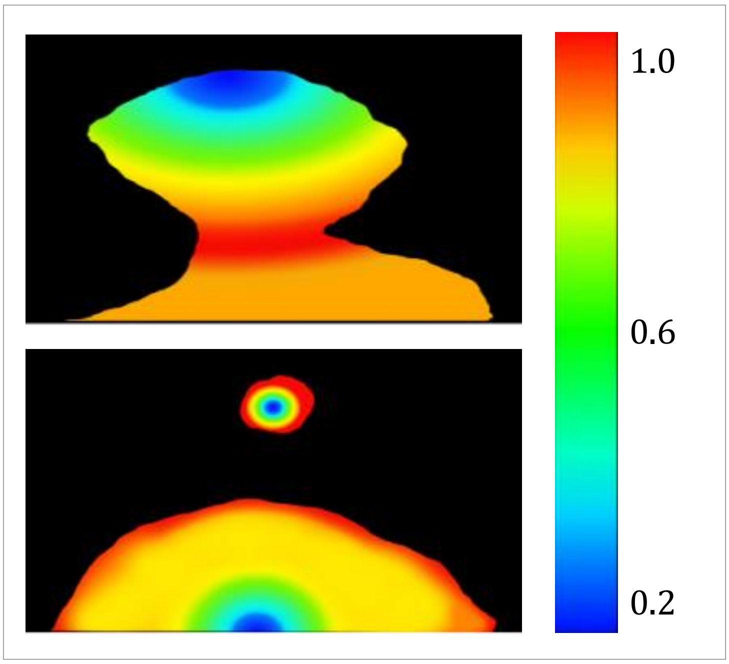

Figure 7.21: The gradient of driving force for perturbation growth and breakaway as a combination of chemical free energy and interfacial energy in close time proximity before and after material break away (t* =20000 and 35000 δ t).

7.5 Conclusion

The coupling of experimental techniques and modelling has allowed the in-depth investigation into the pathway of not only SE in a two-phase system, but also the life cycle of a perturbation and the limits of size before material breaks away to form the emulsion. The in-situ observation of emulsification greatly backs the proposal of hypothesis 5, with spontaneous emulsification being perturbation growth led. The ability to track these phenomena in ultra-high-temperature systems such as those presented is of significant importance to directly related fields such as liquid steel refining of impurity removal such as phosphorus, manganese or silicon. The converse is also true when considering the ability to predict stable new alloy compositions with respect to interaction with ladle slags and mould fluxes. In these reactions knowledge and ability to track the interfacial area between reacting liquid phases offers the potential for precise control in macroscopic systems where dispersions of droplets can have significant control over the observed performance. The direct application of the systems presented here are refining in basic oxygen steelmaking controlled by emulsion kinetics [37] [53] and the composition control and stability of lightweight high-aluminium steel grades.

The formation of a physically validated phase-field model to interrogate SE systems is of great wider value. In addition to the brief summary at the beginning of this chapter, advanced forms of controllable micro dispersions are under use in the fields of medicine [116], polymeric nanoparticle production [117] and efficient recycling of metals [118]. This system is highly dynamic and difficult to capture reliable first principle data for, due to the extreme temperatures involved. As a result, reactions and movement can be magnitudes greater than those seen at room temperature. A greater number of time-step iterations would expectedly be needed for the model to produce a complete life cycle of an emulsifying system in some of the slower reacting systems. Although a 3D model of a system is clearer for qualitative observation and to achieve greater absolute accuracy, the findings in this work show a 2D phase-field system to have strong experimental agreement, and offer a viable option when computation time is considered to track the physical phenomena present in highly dynamic systems over a greater period of time, thus hypothesis 6 is strongly supported, and the level of accuracy possible to acquire for these systems to date presents a viable data source for the prediction of SE occurrence. It is however thought the true engineering of geometries through the process would require more accurate data and development of the model used here.

Despite being able to accurately simulate the interface shape, the phase-field model is still incapable of reproducing features of the interfacial diffusion. Further development of the theory is needed to comprehensively understand the interactions involved in a liquid-liquid interface. An example would be to study whether non-isothermal effects that may result from latent heat could affect propagation of the interface. Another direction is to investigate the phenomenological relationships between diffusion flux and stress tensor. Both expressions were considered to be isotropic; however, an interface (strong gradients in concentration fields) generates anisotropy, so the relationships between thermodynamic fluxes and forces should be reconsidered.

In addition to quantifying the pathway, it is integral to deduce the level of reaction at the interface required for spontaneous emulsification to occur.

Chapter 8

Spontaneous Emulsification as a Function of Material Exchange

8.1 Hypothesis to be Interrogated

Hypothesis 7: "Within a given system there is a critical point at which spontaneous emulsification will begin to occur with respect to starting material composition."

Hypothesis 7 presents the problem of exploring the inflection point of when emulsification does or does not occur. This will be influenced by the overall flux of material across the interface and subsequently it is required to quantify the energy balance between thermodynamic gain against increased interfacial area.

8.2 Introduction

Interfacial tension between molten oxide slurries and liquid steel controls the rate of reaction where material exchange between the two phases is concerned. The steps involved in the transfer of material between the two phases are:

1. Mass transfer of a reactive oxide species to the interface in the molten oxide phase
2. Mass transfer of the reactive element to the interface in the liquid metal phase
3. Interaction of the respective species at the interface
4. Mass transfer of the reaction product away from the interface in the respective phase

The specific system interrogated within the present work is of particular pertinence in manufacturing due to the social drive of lightweighting in sectors such as the automobile industry. As a result, the steel industry finds itself in a position where the development of high aluminium content grades such as TRIP and low density products is no longer a luxury but a necessity in order to stay competitive in the market in comparison to materials such as light metals, composites or carbon fibre.

A high aluminium alloyed steel offers the potential for a stronger lighter material in comparison to those currently available. However, such an alloy presents product issues such as grain refinement due to the lack of phase change, as well as processing chemical stability with both ladle slurries and mould flux compositions due to the high SiO_2 content favourable for both viscosity and melting point influences. Processing flow and the addition of material are known to cause droplet formation of the liquid metal suspended through a protective or partitioning oxide phase, resulting in a large increase in reactive surface area and a potential for significant material exchange.

In the case of aluminium transfer from liquid steel to a metal oxide phase the species involved are elemental aluminium and silicon dioxide; the reaction is shown in equation 8.1

$$4[Al] + 3(SiO_2) \rightarrow 3[Si] + 2(Al_2O_3) \tag{8.1}$$

where species in [] are in within the liquid metal phase, and those in () are in the molten oxide phase. In systems such as these, at liquid temperatures it is well documented that the reactions at the interface are much faster than material mass transfer within the bulk phases and thus reduction of the diffusion length from bulk to interfacial reaction site would increase reaction kinetics. This has previously been reported as a broadening of a metal droplet during sessile drop interrogation [66] (reduced contact angle) or in the case of an unbound metal droplet mixing of the two phases into a micro emulsion [62] [86].

With these conditions the reaction rates of a system where a defined first phase (in this study the metal droplet) is freely suspended in a continuous second phase (in this study the metal oxide mixture) are limited by the interfacial area/bulk volume ratio, with the size of the interface (or surface area of a single material) being a balance between material size, interfacial tension and physical forces.

8.2.1 Theoretical Consideration of Interfacial Tension

Interfacial tension (γ) is a balance of the favourable homogeneous phase interactions as opposed to heterogeneous phase interactions; this is shown through equation 8.2:

$$\gamma = (\sum aE_i^{1-1}, bE_{i+1}^{1-1}, cE_{i+2}^{1-1}, \ldots, xE_{i+n}^{1-1}) - (\sum dE_i^{1-2}, eE_{i+1}^{1-2}, fE_{i+2}^{1-2}, \ldots, yE_{i+n}^{1-2}) \tag{8.2}$$

where E_i^{1-1} is the homogeneous phase interaction within the ith solvation shell; E_i^{1-2} is the heterogeneous interaction within the ith solvation shell; and $a, b, c \ldots x, y$ are scaling factors for the number of interactions experienced with each solvation shell. Within a defined interface a < b and so on for the scale of each solvation shell. It should be noted from the relationship described in equation 8.2 that interfacial tension can never be zero. Homolytic and heterolytic interaction will never be equal in energy. If heterolytic interaction is stronger than homolytic then equation 8.3 would become true:

$$\sum_i^n E^{1-2} > \sum_i^n E^{1-1} \tag{8.3}$$

If this were true there is favourable free mixing of species, there is no defined interface, only a single phase. From this we see that interfacial tension minimization is driven by an increase in free energy as atomic interaction energies are fixed for a given condition. This results in the driving force of surfactant behaviour arising if possible where heterogeneous interaction between the interfacial location driven species and a bulk phase is less of an energy cost. For iron and metal oxide two-phase systems, known atomic interfacial active species of significance are O, S and P in descending order of influence [119]. The concentration of these species with respect to interfacial energy reduction has been extensively studied; for example the present author has shown the driving of this species to an equilibrium state throughout an industrially relevant system as being a key contributing factor to the spontaneous emulsification of a metal droplet [62] [86].

As well as the doping of an interface with surfactants, the author will investigate if material exchange across the interface alone can be enough to reduce “effective” interfacial tension to a point where physical forces such as Marangoni flow can be enough to cause the break-up of an interface.

Movement of species across an interface due to thermodynamically favourable reaction is a manifestation of the E^{1-2}_{i+n} term increasing from equation 8.3. In the case presented here, transfer of aluminium across the interface can be seen as a sublattice of aluminium kinetically partitioned from the thermodynamically stable oxide phase, where the iron-aluminium interactions dictate the rate of aluminium movement through the bulk metal phase and across the interface (the diffusion rate). An example of when equation 8.4 holds true is if phase homolysis is considered as opposed to atomic homolysis:

$$\sum_{i}^{n} E^{P1-2} + f(\Delta S_{mix}) > \sum_{i}^{n} E^{P1-1} \tag{8.4}$$

where E^{P1-2}, E^{P1-1} are representative of the interaction energies of aluminium with the bulk oxide phase and bulk metal phase respectively depicted in figure 8.1. In addition a function of the entropy of mixing ($f(\Delta S_{mix})$) should be considered as shown within equation 8.4. When an aluminium atom reaches the interface, it must displace/fill a void of the bulk phase locations (in this case iron atoms), reducing order at the interface and the number of E^{1-1} interactions an iron atom experiences at the interface. Hence an impurity at the interface reduces interfacial tension [120].

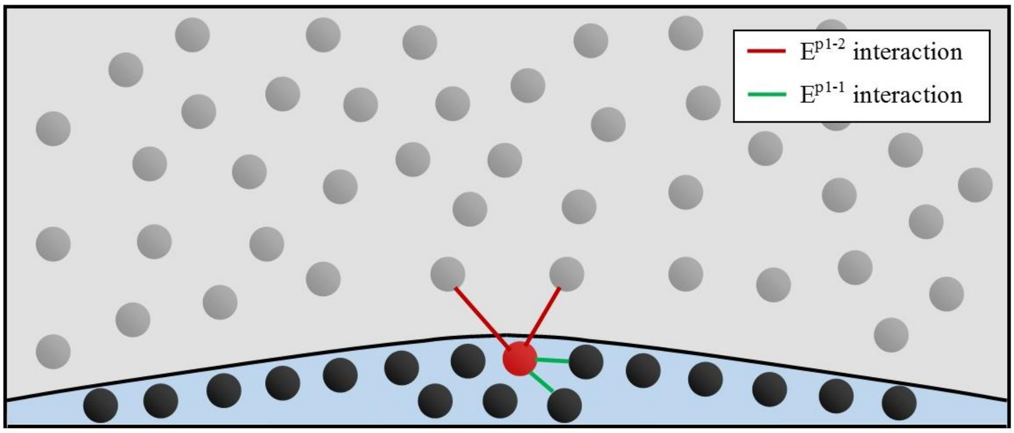

Figure 8.1: A schematic of the interface between a molten iron droplet (black particles) and a molten oxide suspension medium (grey particles). An *Al* atom is present at the interface (red) with examples of inter (E^{P1-1}) and intra (E^{P1-2}) phase interactions depicted.

In this paper, we will interrogate the starting concentration of aluminium atoms in the metal drop (which governs the flux of aluminium atoms to the interface) required to cause sustained perturbation growth on the metal phase surface, as well as the number required to facilitate spontaneous emulsification of the metal phase through a molten oxide matrix.

8.3 Experimental

In this investigation seven $FeAl$ alloys were used; their compositions are presented in table 8.1. The alloys were formed using an open induction furnace with a stock electrically produced "pure" iron chip source and the addition of high-purity aluminium chips with consecutive addition and sampling of the melt to screen the required compositions. All experiments used the same master oxide mixture, the composition of which is presented in table 8.2. The oxide phase was produced from powder mixing of the three reagent grade powders followed by pre-melting of the mixture at 1873 K in a horizontal tube furnace using a gaseous environment of argon (<2 ppm oxygen). The pre-melting stage was used to ensure full mixing of the oxide compounds, and was followed by disc milling to form a well-mixed master oxide phase.

Table 8.1: Compositions of $FeAl$ alloys used for the experiments in HT-CSLM presented in mass %. Compositions were measured by ICP (all alloys contained <0.001 %N).

Sample ID	$Mn\%$	$P\%$	$Ni\%$	$Cr\%$	$Al\%$	$C\%$	$S\%$	$O\%$
0% Al	0.0003	0.0004	0.0001	0.0003	0.00005	0.004	0.001	0.0034
1% Al	0.0003	0.0004	0.002	0.0005	0.99	0.0011	0.001	0.0028
2% Al	0.0004	0.0004	0.001	0.0003	1.92	0.0006	0.001	0.0029
3% Al	0.0002	0.0004	0.002	0.0005	2.84	0.0011	0.002	0.0035
4% Al	0.0004	0.0004	0.002	0.0005	3.98	0.0007	0.002	0.0042
5% Al	0.0003	0.0003	0.002	0.0004	4.92	0.0009	0.002	0.0040
8% Al	0.0002	0.0004	0.002	0.0005	7.87	0.0007	0.001	0.0038

A high-temperature confocal scanning laser microscope (HT-CSLM) was used to perform the in-situ observation of the reacting phases. Details on the microscope can be found in previous reportings [86]. 0.2 g ± 0.02 of the oxide powder was placed into a sapphire crucible. After placing of the sample inside the HT-CSLM

Table 8.2: Composition of the metal oxide mixture used for HT-CSLM experimentation after pre-melting of reagent grade hand-mixed powders presented in mass %. Compositions were measured by XRF.

$CaO\%$	$SiO_2\%$	$Al_2O_3\%$
36.17	23.11	38.53

chamber, the chamber is evacuated using a rotary pump for half an hour, followed by back filling with high-purity argon (99.9999% argon passed through a further heated getter containing copper and magnesium chips at 623 K); this is done three times to ensure a clean environment with a minimal oxygen partial pressure in the chamber. This initial sample is then pre-melted at 1873 K in the HT-CSLM following the regime depicted in figure 8.2. Upon cooling to room temperature. the oxide forms a glassy phase with a deep meniscus due to high wettability of the liquid oxide with the crucible walls. A cylinder of mass 17 mg ± 0.7 (a large mass range is due to the varying density of the alloys) with dimensions 1.19 mm H, 1.49 mm D (professionally machined) of the respective alloy is then added to the centre of the glass meniscus and a further 0.3 g ± 0.12 of oxide powder is placed on top of the metal and lightly compressed by hand. The crucible is then placed back into the HT-CSLM on top of a platinum foil spacer which in turn is on top of an alumina spacer. The platinum spacer is used to increase back scattering of light through the optically transparent molten oxide phase at experimental temperature (increased field of view in the z-direction); the alumina spacer is used to stop the platinum spacer sticking to the platinum ring of the sample stage. This chamber is again cycled three times through the vacuuming and argon back filling stages before the experiment is conducted under the melting profile displayed in figure 8.2. Due to the dynamic environment produced within the HT-CSLM sample it is very challenging to locate the metal droplet; high levels of light gain (widening of the UV laser aperture) and brightness are used to locate the droplet between the slag melting point and the beginning of meaningful video recording before settings are returned to those suitable for imaging. Video was captured at 15 fps.

Calibration of the HT-CSLM is conducted through the melting of silver, copper and iron samples and aligning the temperature readout with the actual melting temperature of these samples. Under such setup the thermocouple of the HT-CSLM can be as much as 70 K away from the true sample temperature when investigated

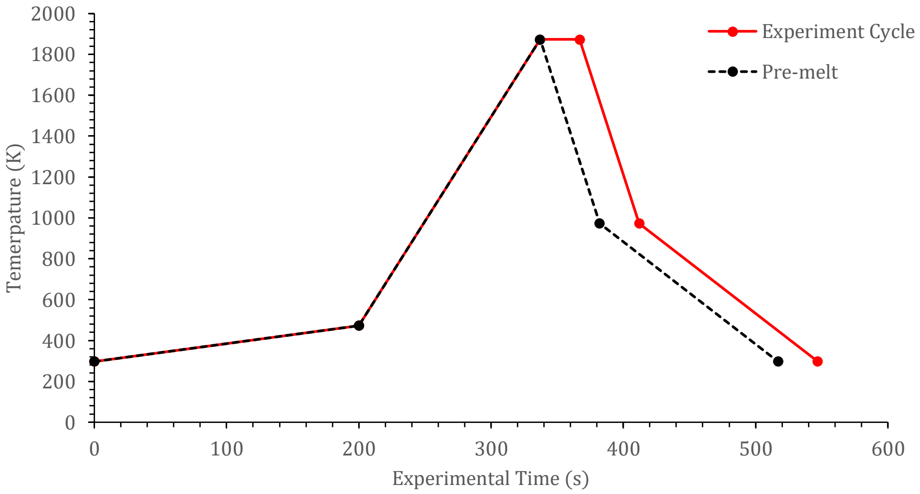

Figure 8.2: The nominal heating cycle used for both pre-melting of metal oxides and experimentation of oxide/metal alloy reaction in the HT-CSLM.

in this manner. Figure 8.2 and reported experimental temperatures are after calibration.

With the use of the semi-transparent sapphire crucibles the physical heating profile of the HT-CSLM was also investigated. Pieces of thermal paper (similar to that used in till receipts) cut to size were placed in the base of the crucible on the stage and spacers. The halogen bulb was then manually turned on for short periods of time and the resulting heat markings on the paper observed. At low bulb powers and very short times a 2 mm diameter spot in the centre of the crucible was observed, this represents the designed focal point of the HT-CSLM chamber. With incremental increases in time and power exposure, the centre point in the paper was not seen to grow by an amount observable by eye (due to the poor thermal conduction of the paper), however a ring around the outside of the crucible was seen to form and grow inwards. In comparison an opaque crucible such as one of the same dimensions formed of high-density MgO, did not display the outer heat ring on the crucible base. It is thought that the transparency of the sapphire crucibles to the IR wave lengths emitted by the halogen bulb allows for direct heating of a sample not only from the centre focal point but also from the crucible edges inwards. This creates a more uniform heat profile through the sample than in previous experiments, reducing convection and aiding the metal droplet to stay relatively stationary for viewing during reaction.

The videos produced from HT-CSLM experiments have undergone image processing through grey scale correction to a two-point grey scale, followed by a segmentation of the image through manual determination of white dictating in-focus metal phase, and black dictating molten oxide phase. In the case of observation such as in the first 2% $FeAl$ image for example, the large hollow in the light area of the droplet image is included in the droplet area segmentation. Data produced from this method was averaged over 3 frames (the frame each side and the frame of the time point reported) due to the raster of confocal focus point in the z-plane to give clearer imaging and greater accuracy in determination of surface area calculation.

Further to this, samples were mounted in resin and sectioned to observe the quenched material. Figure 8.3 shows the cross sections observed by eye of quenched samples originally containing the 0%, 3% and 5% $FeAl$ alloys. From these images we can clearly see that the droplet is suspended in the oxide phase (not on the surface). In addition, it is qualitatively notable that there is a reduced mass of material recovered when the initial $FeAl$ content has been increased (a-0%, b-3% and c-5%). This is expected due to the higher droplet surface area produced during the experiment allowing for a larger quantity of Fe to be oxidized (causing the metal phase volume reduction), as well as the additional factor of offspring droplets having not fully coalesced in the emulsifying systems.

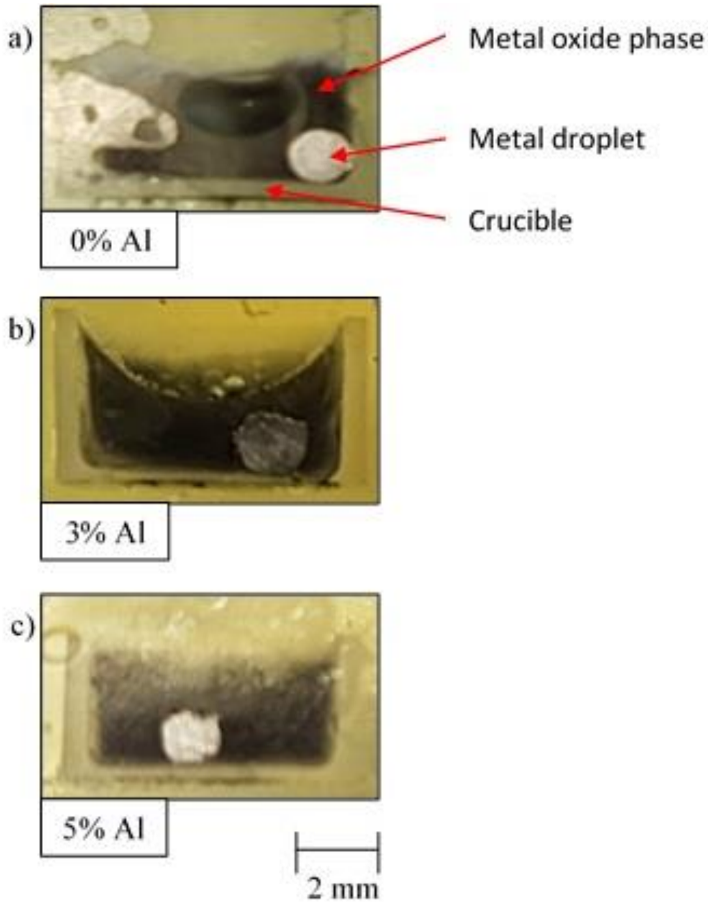

Figure 8.3: Images of the sectioned quenched samples showing the droplet suspended in the oxide phase and the reduction in metal recovery in higher Al content systems. a) 0% $FeAl$, b) 3% $FeAl$, c) 5% $FeAl$.

8.4 Results

Stills of the video output from the HT-CSLM are presented in figures 8.4, 8.5, 8.6, 8.7 and 8.8. These figures correspond to samples 5% $FeAl$ through to 1% $FeAl$ in respective descending order. Images from 8% $FeAl$ show a very similar behaviour to that of 5% $FeAl$, and those of 0% $FeAl$ show a quiescent near-spherical droplet for the entire period.

Figure 8.4 shows the time-dependent behaviour of the 5% $FeAl$ sample. From the point at which the droplet is focused upon, perturbation levels are seen to exponentially increase to a point where the entire field of view is flecked with points at which perturbations from lower down in the sample have grown into the focal level. At 8 seconds the metallic phase clouds the entire field of view as seen in figure 8.4d (due to the 2D imaging of the 3D system, individual droplets of the formed micro emulsion are indistinguishable). The system then goes on to begin coalescence of the metal droplets at 12 seconds where towards the edge of the sample defined small pockets of isolated metal phase can be seen, before complete coalescence is observed at 15 seconds after temperature is reached.

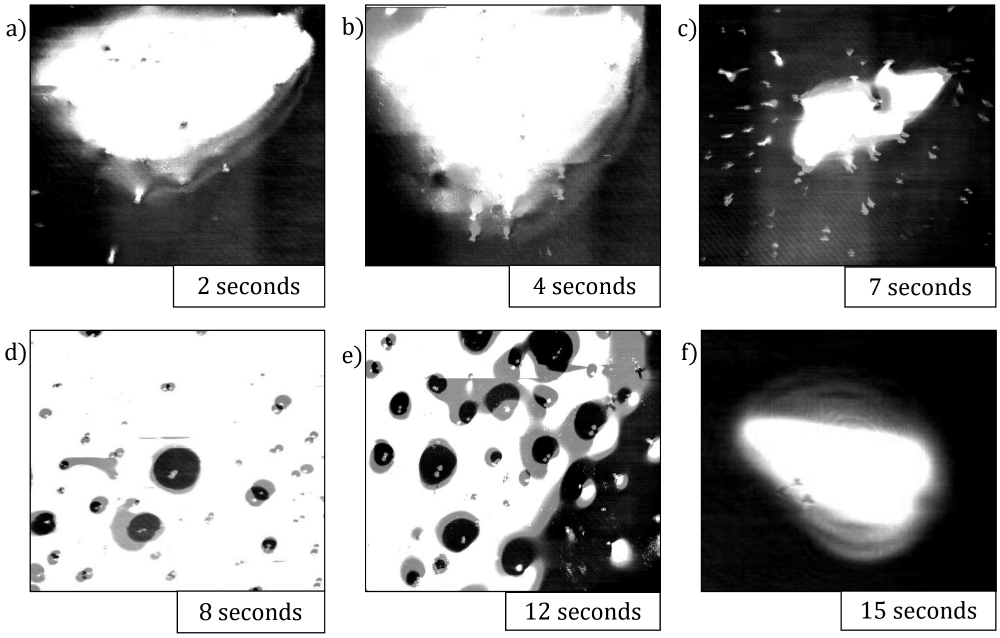

Figure 8.4: Time step images of the 5% *FeAl* experiment as seen in the HT-CSLM. In focus metal phases appear as lighter in grey scale and the molten metal oxide phase is seen as black. a)-f) show the cycle of perturbation-emulsification and finally coalescence.

Figure 8.5 is the time-step image sequence from the 4% *FeAl* sample with the same image times as that of figure 8.4. It is quantitatively observable that the level of perturbations observed in figure 8.5a, b and c are lower (there are a lower number of distinct perturbations) than that of the 5% *FeAl* sample with the sample emulsification seen to be delayed; emulsification is only visible in the 12 second still and the level of emulsification is seen to be less than that of the 5% *FeAl* sample.

In figure 8.6 the sample time-steps are presented for the 3% *FeAl* sample; in this video no clouding/emulsifying behaviour was observed. The level of perturbation is much reduced compared to that of the images in steps preceding emulsification in the 5% and 4% *FeAl* samples, however the period of highest perturbation levels is still in the region of 8 seconds. The sample is however seen to be quiescent at 12

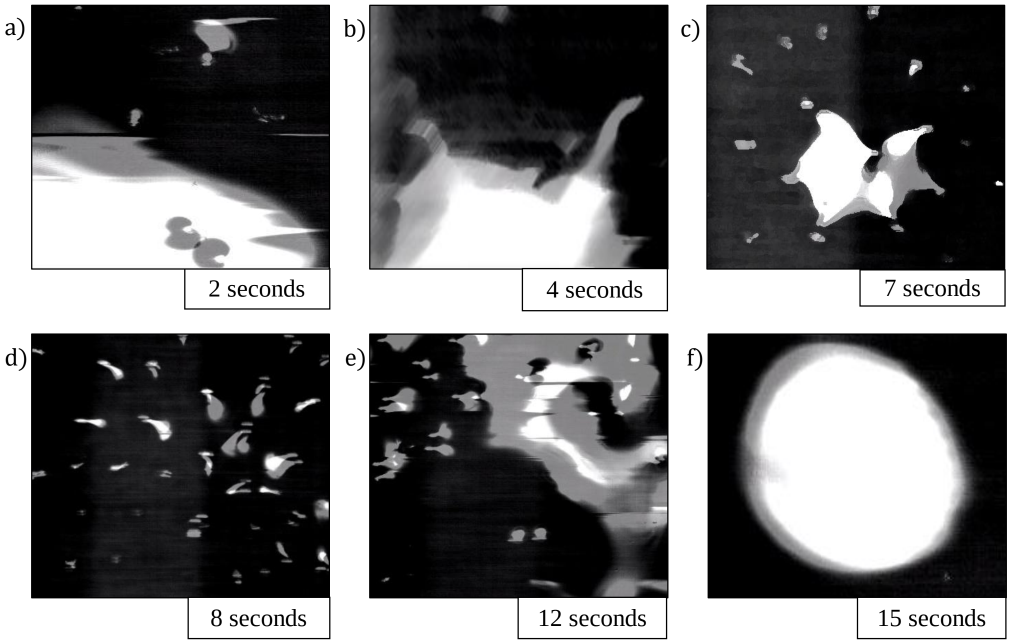

Figure 8.5: Time step images of the 4% $FeAl$ experiment as seen in the HT-CSLM. In focus metal phases appear as lighter in grey scale and the molten metal oxide phase is seen as black. a)-f) show the cycle of perturbation-emulsification and finally coalescence.

seconds.

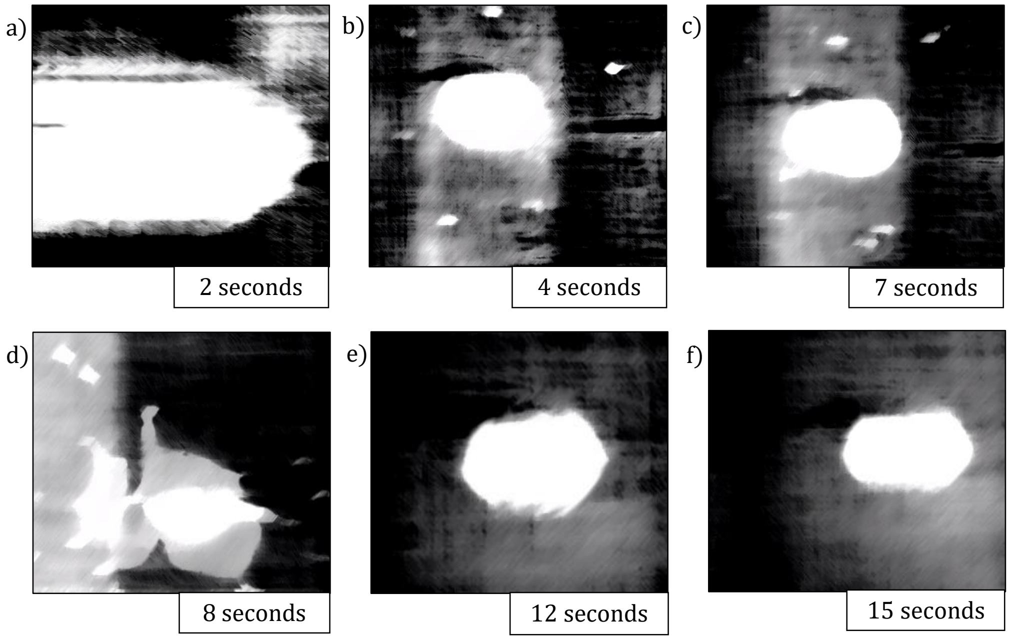

Figure 8.6: Time step images of the 3% $FeAl$ experiment as seen in the HT-CSLM. In focus metal phases appear as lighter in grey scale and the molten metal oxide phase is seen as black. a)-f) show the cycle of perturbation growth with no emulsification seen.

The cycle of the 2% $FeAl$ and 1% $FeAl$ samples during reaction can be seen in figures 8.7 and 8.8 respectively. The images show significantly reduced levels of perturbation compared to that of the 3% $FeAl$ sample, and a shift of the highest level of perturbation to earlier in the experimental regime (around 7 seconds). The difference in behaviour is difficult to qualitatively justify from viewing of the video, however after imaging processing and subsequent measurements being performed there is a subtle but definite reduction in perturbation level and sustained perturbation time between the 2% and 1% $FeAl$ samples.

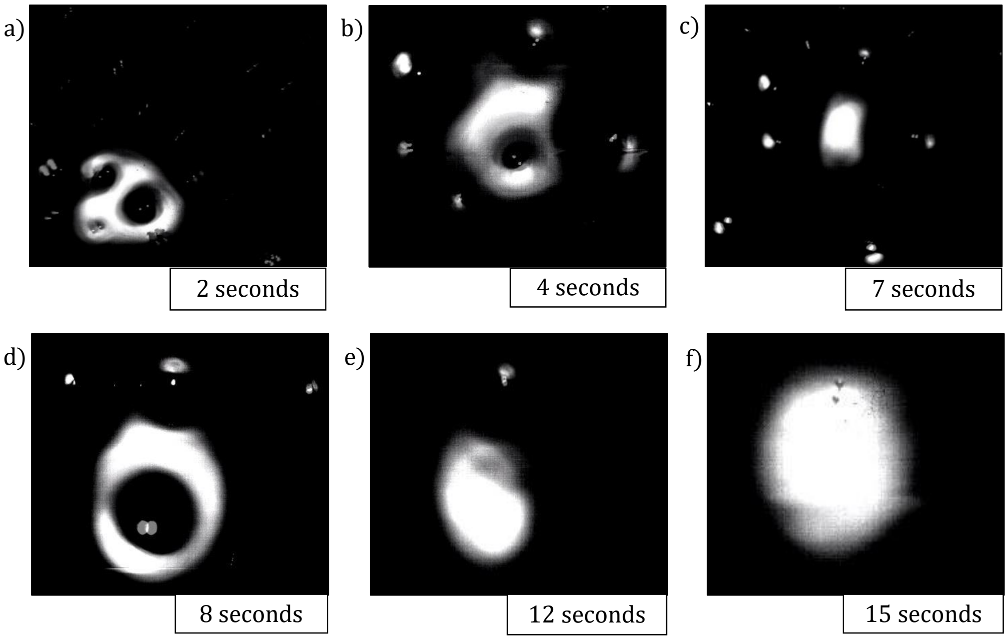

Figure 8.7: Time step images of the 2% $FeAl$ experiment as seen in the HT-CSLM. In focus metal phases appear as lighter in grey scale and the molten metal oxide phase is seen as black. a)-f) show the cycle of perturbation growth to quiescent droplet.

Image processing allows for quantification of the liquid metal surface area as seen in the 2D images of the HT-CSLM. Figure 8.9 displays the relative metal surface area change as a function of time for all seven experiments (extrapolated back to zero time assuming a quiescent sphere is formed on first melting). The measurements of the images displayed in figures 8.4-8.8 are highlighted.

From figure 8.9 we can see the 2D image analysis has led to distinct profiles for different levels of Al in the metal droplets. Both 8% and 5% $FeAl$ samples show an emulsification profile near 10 times the original surface area of an ideal droplet (spherical shape) at its highest point; they both peak at 8 seconds. The 4% $FeAl$

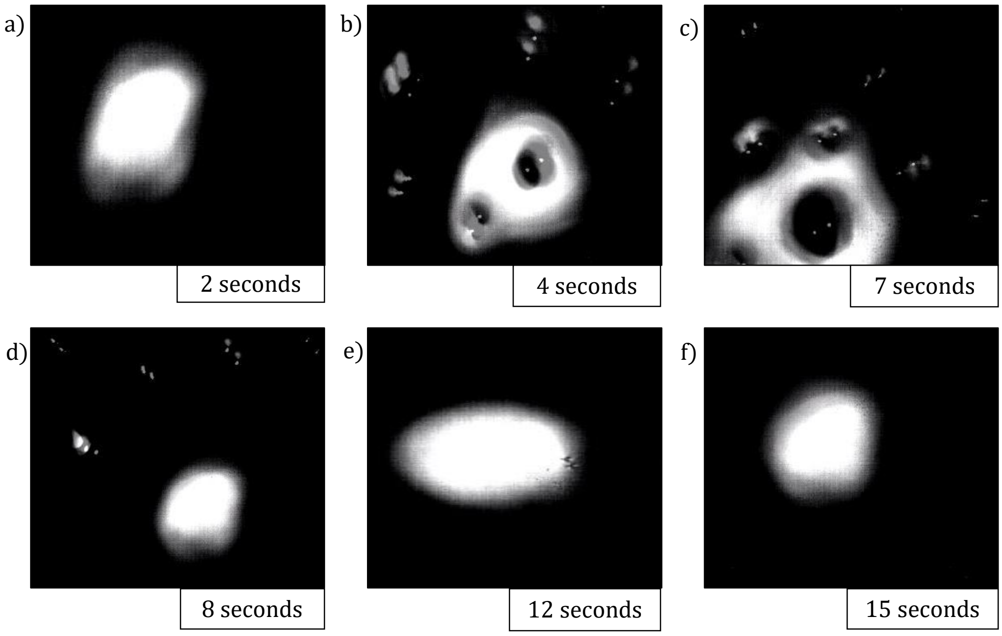

Figure 8.8: Time step images of the 1% $FeAl$ experiment as seen in the HT-CSLM. In focus metal phases appear as lighter in grey scale and the molten metal oxide phase is seen as black. a)-f) show the cycle of perturbation growth to quiescent droplet.

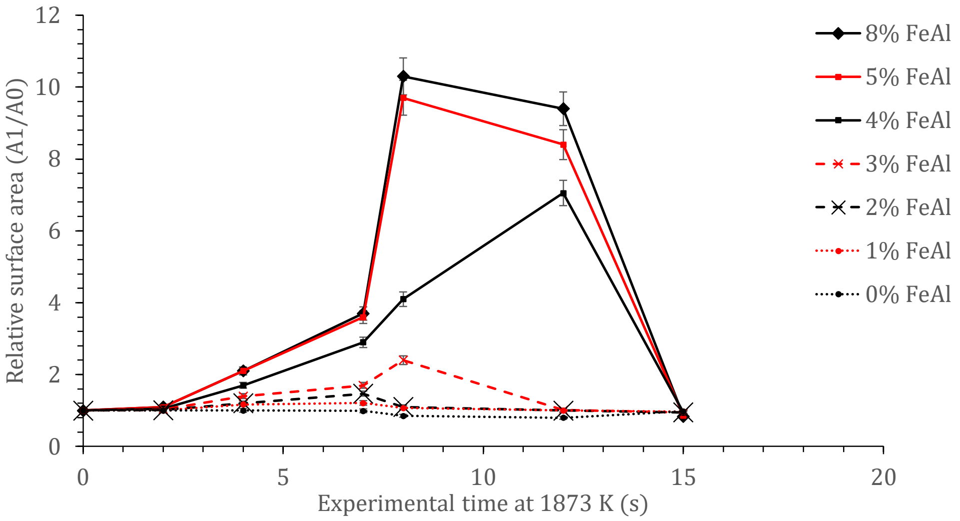

Figure 8.9: The surface area ratio profiles as deduced from image analysis of the HT-CSLM video (to the nearest 0.05). 1 in 15 frames have been analysed but only the points corresponding to those in figures 8.4-8.8 are highlighted.

sample still shows emulsification behaviour to a lesser extent, with a maximum of near 7 times an ideal droplet; this maximum does however come significantly later in the reaction process. Samples of 3%, 2% and 1% $FeAl$ show much lower levels of surface area increase, with less perturbation than the higher aluminium content alloys and no emulsification behaviour. Although not visible due to scale on the graph here, there is a trend of end-point surface area ratio being below 1, with samples that emulsified having a lower ratio than those that didn't. This reduction in size is due to the oxidation of the sample/dissolution into the slag phase. Samples which emulsified have much larger surface area not only for aluminium refinement but also for oxidation of the bulk iron phase, meaning greater loss of material (as previously depicted in figure 8.3).

8.5 Discussion

Figures 8.4-8.8 clearly depict the change in droplet morphology lifecycle when aluminium content is reduced in the metal droplet. The quantification of surface area change shown in figure 8.9 offers clarification of four behaviours. The 8% and 5% $FeAl$ samples show exponential increase in surface area between 7 and 8 seconds. This large increase in area over such a short period shows true spontaneous emulsification behaviour; the droplets effectively tear themselves apart into the micro-emulsion of smaller droplets. This may be indicative of breakaway droplets further breaking down due to the large chemical potential in place across the interface. The 4% $FeAl$ sample shows a similar level of emulsification to the higher aluminium content samples, however the peak in surface area is later into the reaction cycle and the increase is more gradual. A method by which this would happen is if the budding of perturbations on the droplet surface continued to occur at a faster rate than any coalescence; rather than a sudden break down of the droplet there is a gradual release of offspring droplets through the reaction period.

Although the 8%, 5% and 4% $FeAl$ samples show differing emulsification profiles, the coalescence behaviour is very similar. Due to the differing time scales for emulsification to occur, the severity of emulsification and the sustained chemical potential across the interface in the offspring droplets aluminium content is reduced at a faster rate in the metal droplet at higher original aluminium content. So much so that we see all emulsifying systems coming to a quiescent droplet within a very close time proximity.

Riboud and Lucas [99] conducted similar experiments where a larger iron-aluminium alloy droplet was observed via X-ray radiography. Their results were recorded over a much longer time period (around 50 minutes), and their interpreted interfacial tension between metal and oxide phase during the observation is reported. They follow the workings of Defay, Sanfeld, Steinchen and Friedel [121] [122] [123], where a model of equidistant planes parallel to the interface containing the molecules is considered against a perpendicular z diffusion axis. In this model they discuss a mechanical equilibrium expression for interfacial tension such that:

$$\gamma = e^3 \int_a^b \sum_x \sum_{x'} k_{xx'} c'_x c'_{x'} dz \tag{8.5}$$

where $k_{xx'}$ is the attraction between molecules x and x' situated in a layer thickness e; $c'_x = dc_y/dz$ and $c'_{x'} = dc_{y'}/dz$ are the concentration gradients along the z-axis; a and b are positions on the z-axis in two phases A and B far enough from the interface that c'_y and $c'_{y'}$ are negligible. This results in a discussion of interfacial tension being zero when there exists a pair of concentration gradients with opposite signs and heterogeneous interactions are greater in strength than homogeneous interactions. Although this is similar to the treatment of interfacial tension discussed in the opening arguments, there is a fundamental difference where the current work considers this movement of favourable exchange between phases to be a sublattice exchange; this is not the mixing of the two bulk phases. If two bulk phases still exist, there must be a net positive interfacial tension.

This being said the trend of interfacial tension change does not change, only the absolute values. These values are incomputable from the data collected in this study, however if the trend reported by Riboud and Lucas [99] is corrected for time scale due to the miniaturization of the present study the interfacial tension coincides well with the interfacial area changes in current systems, with the spontaneity of emulsification and coalescence captured. There is a delay of surface tension increase in comparison to that of interfacial tension in the earlier study which is thought to be caused by the heating performance of the HT-CSLM. During these early stages the sample in the HT-CSLM may be below the programmed temperature of 1873 K and spatially heterogeneous with regards to temperature, this would cause the reaction between aluminium and SiO_2 to be hindered.

Both Riboud et al [99] and Rhamdhani et al [63] [64] [65], present the most directly relevant system reports in the literature previously. The major experimental differences between the three studies are: Riboud [99] uses a larger droplet dimension (0.5-2 g) and the experiment is akin to in-situ x-ray observation of a sessile experiment, the droplet is in contact with a substrate at all times; Rhamdhani [63] uses a larger droplet dimension (1.7-3.25 g), with the droplet suspended in the oxide medium and samples were quenched and crushed for evaluation; the present study uses smaller droplets (17 mg ± 0.7), suspended in the oxide medium observed in-situ via a scanning UV laser.

The first consideration for analysing the effects of experimental differences is the pathway of perturbation growth and budding of the system. Perturbations initially grow due to the shortening of diffusion distance to reactive species in the bulk oxide phase. Figure 8.10 offers a schematic tool to explain this, where: a) depicts the diffusion distance for SiO_2 to reach the perturbation head from the bulk oxide phase; b) depicts the diffusion distance for SiO_2 to reach the perturbation length centre (and at a later stage the neck of a perturbation); c) depicts diffusion distance for SiO_2 to reach the main droplet body. As material is reacted the perturbation growth is sustained through entering areas of the bulk oxide phase where SiO_2 is still enriched; this microscopic growth phenomena reduces the diffusion length required for new SiO_2 molecules to reach the interface. The sustained growth/increase in surface area is energetically rationalised by the increase in material exchange between the two phases; the Gibbs free energy is still reducing in the overall system. As the perturbation grows distance a) is maintained, and distance c) is maintained, but the effective distance b) (distance from the perturbation centre to the bulk oxide phase) is increased due to depressed levels of SiO_2 in the oxide bulk phase through which the perturbation front has previously grown. This creates a profile of reaction potential down the perturbation, with higher chemical potential in the perturbation head and lower chemical potential further down the direction of growth. This results locally in a necking phenomenon as the advancing perturbation head growth is sustained while there is much less drive for increased width close to the main droplet body. This results in the development and gradually increasing severity of the angle labelled θ on figure 8.10. We can add this geometric constraint to the expression for interfacial tension presented earlier in this work, together with mixing drive in the system, to give an expression for inter-phase tension γ_p:

$$\gamma_p = g(\theta)(\sum aE_i^{1-1}, bE_{i+1}^{1-1}, cE_{i+2}^{1-1}, \ldots, xE_{i+n}^{1-1}) - (\sum dE_i^{1-2}, eE_{i+1}^{1-2}, fE_{i+2}^{1-2}, \ldots, yE_{i+n}^{1-2}) - f(\Delta S_{mix}) \quad (8.6)$$

where $g(\theta)$ is the geometric strain on the homolytic interactions and $f(\Delta S_{mix})$ is a function of entropic mixing.

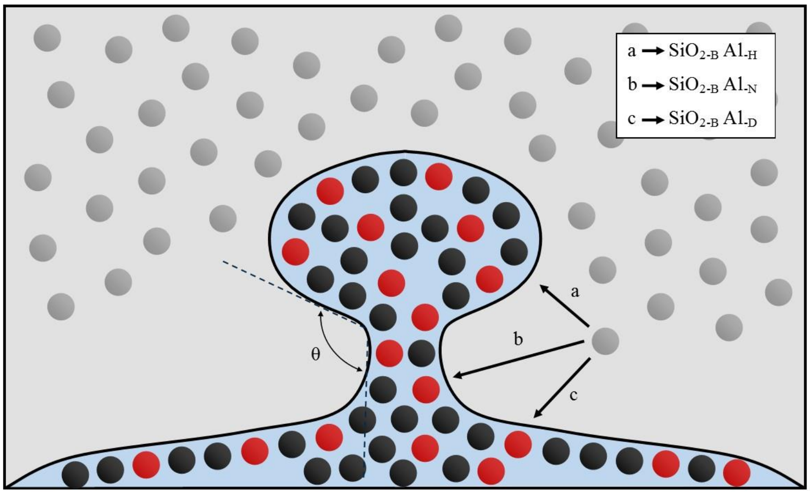

Figure 8.10: A schematic of the interface between an iron aluminium metal alloy (black particles represent iron atoms, red particles represent aluminium atoms) and a metal oxide medium (specifically silica molecules, grey particles). An example of perturbation growth and necking is given with varying diffusion distances of SiO_2 bulk particles to perturbation head ($SiO_{2-B}Al_{-H}$, neck ($SiO_{2-B}Al_{-N}$) and bulk droplet ($SiO_{2-B}Al_{-D}$) qualitatively depicted. The strain angle θ as a result of necking is also indicated.

The differing results found in each experiment can thus be explained through interrogation of the curvature stress caused on the droplet while undergoing reactions. When the metal is in contact with an inert substrate as in Riboud's report [99], the droplet shows a preference to wet the substrate (this effect was also seen in the observation of unsuccessful experiments in the present study where the droplet touched the crucible wall or base). The result of the contact is that when a perturbation grows there is little resistance from the bulk droplet (little strain) so perturbation necking is less severe, giving a reduction in geometric strain on bonding interaction at the interface. If the converse is considered (the present work), a smaller droplet in free space results in a more acute angle as θ is reduced, with the perturbation neck merging with the main droplet curvature. This creates high levels of strain at the perturbation neck. This strain along with the system free energy can be stabilized by the physical detachment of the perturbation head from the main droplet body. This is the phenomenon we refer to as budding.

The levels of perturbation/emulsification follow this trend through Riboud and Lucas [99] who report a wavy quenched interface geometry for a sample in the middle of the reaction; Rhamdhani et al [64] reported some material break up through the discovery of several metal droplets of varying sizes in the quench sample; the present work shows full emulsification of the higher aluminium content samples, but also behaviour similar to those of larger droplets when lower aluminium contents are investigated (this is due to the reduction in perturbation growth speed, giving greater time for diffusion of SiO_2 towards the perturbation length centre, reducing the impact on necking severity).

As stated earlier, the time taken to reach a quiescent droplet interface at/near equilibrium is greatly reduced in the current work in comparison to that of Riboud and Lucas [99]. This is expected to be due to three reasons: 1) the droplet being much smaller, 2) spontaneous emulsification occurring, greatly increasing the surface area/volume ratio, and 3) an unbound droplet being able to grow perturbations into new bulk composition areas of oxide phase in all directions. These factors change the probable rate controlling step from SiO_2 mass transport in the earlier reported work to Al mass transport in the current findings.

The effect of oxygen concentration in the metal droplet of similar two-phase systems is well documented by several authors [92] [119] [124] [125] [126]. Reports range from a surface tension of close to 1500 mN m^{-1} at near zero oxygen content and follow an exponential decay in interfacial tension to values of near 400 mN m^{-1}. From previous discussion we know barriers close to the lower end of this spectrum are possible to overcome and emulsification occurs to a high degree [62] [86].

This allows us to confirm that interfacial tension of the 3%, 2% and 1% $FeAl$ samples did not reach levels as low as 400 mN m^{-1} as emulsification did not occur. Further to this, the current study contains no FeO in the oxide phase, a key agent in the provision of oxygen content for low interfacial tension. Although we cannot bound the interfacial tension for higher levels of aluminium, it is improbable when considering the behaviour shown with oxygen content that a 1% increase in aluminium content would drastically reduce the interfacial tension to a near zero or negative value.

In an effort to quantify the interfacial tension through visualization of spontaneous emulsification performance, it is thought a future investigation where iron (II) oxide content is varied in the oxide phase of experiments in the HT-CSLM could be used to validate interfacial tension in systems undergoing transport of material across the interface.

To quantify the reasoning behind the inflection point in emulsification behaviour of the varying $FeAl$ content alloys, an investigation into the energy balance of free energy dissipation competing with the increased global interfacial tension due to increasing surface area is performed (values for calculations given in table 8.3). Using the interfacial areas measured for 8% $FeAl$, (deemed the standard emulsification behaviour) and an interfacial tension of 1500 mN m^{-1} as a realistic maximum from the literature [91], the energetic cost of interfacial area change with time can be calculated with use of equation 8.7 as shown in figure 8.11:

$$SI_T = I_A x I_T \tag{8.7}$$

where SI_T is the energy cost of sustaining the interface between metal and oxide in the system, I_A is the interfacial area between metal and oxide phases and I_T is the interfacial tension.

Table 8.3: Literature values used for calculation of global interfacial tension and dissipation of free energy as displayed in figure 8.11.

Interfacial Tension	1500 mN m^{-1}
$\Delta H_{Formation} Al_2O_3$	-1669.8 kJ mol^{-1}
$\Delta H_{Formation} SiO_2$	-859.4 kJ mol^{-1}
SAl_2O_3	50.92 J mol^{-1} K^{-1}
$SSiO_2$	42.0 J mol^{-1} K^{-1}
$C_pAl_2O_3$	880 J Kg^{-1} K^{-1}
C_pSiO_2	680 J Kg^{-1} K^{-1}
Temperature	1873 K

The total dissipation of free energy due to reaction for each level of aluminium content is then also calculated with use of equation 8 and displayed in figure 8.11:

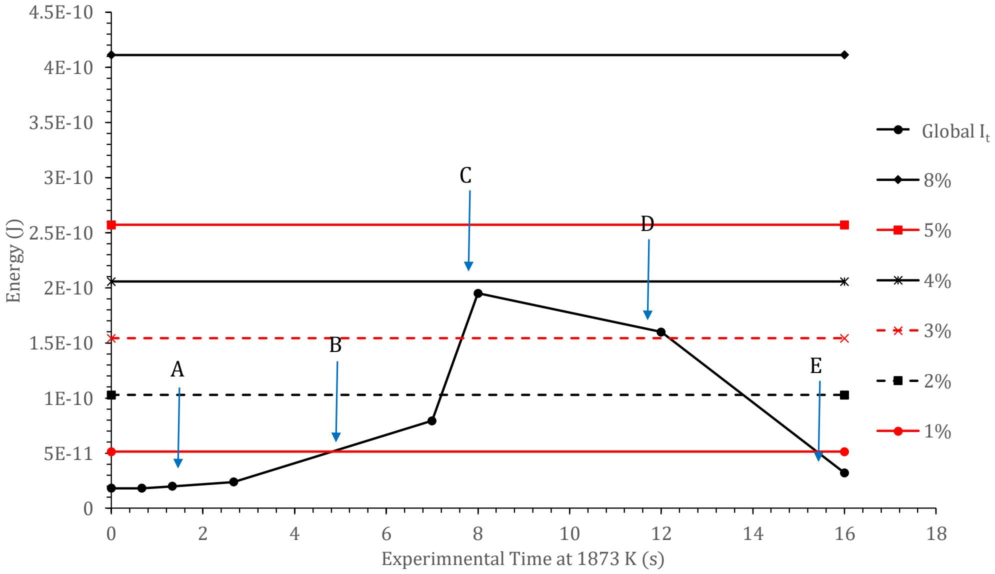

Figure 8.11: Global interfacial tension during the increase and reduction of interfacial area as measured for the 8% $FeAl$ sample coupled with the free energy gain of reaction to equilibrium for the 8, 5, 4, 3, 2, and 1% FeAl systems. Period A is during initial light perturbation, B during heavy perturbation, C fully emulsified, D ongoing coalescence and E a fully coalesced droplet.

$$\Delta G = \Delta H^* - T\delta S \tag{8.8}$$

where G is the Gibbs free energy, H^* the reaction enthalpy calculated using Kirchhoff's Law, T is the temperature and S is the reaction entropy.

Input values for these calculations are also presented in table 3. At 8 seconds, the point of highest emulsification level observed in the higher aluminium content samples is pin pointed in the centre of the global I_t curve (zone C), with the free energy gain of the 4% $FeAl$ sample just slightly higher. This agrees well with the experimental observations as up to zone C the surface area is growing (through regions A and B where perturbation begins, and grows), and thus a driving force for the spontaneous emulsification cycle is required. After point C we have gradual coalescence of the metal phase defined by D, restricted through statistical colocation of material and restraints such as film drain barriers (previously discussed to be dictated in a pathway well described by DVLO theory [62]). Thus after 8 seconds the surface area is unstable. There is no longer a driving force for a sustained interfacial area. Finally, the reaction reaches point E where the droplet has fully coalesced. Although 4% $FeAl$ is above the energy required to develop the fully emulsified state, it is extremely close in energy levels required. This may explain the prolonged time, and reduced level of emulsification seen compared to the higher levels of $FeAl$ which exhibit more similar behaviour to each other.

8.6 Conclusions

The effect of aluminium content on the transient interface morphology between iron aluminium alloy droplets and an enriched silicon oxide phase has been studied in-situ with use of a HT-CSLM. The behaviour shows an inflection between 4% and 3% $FeAl$ content samples evaluated through the surface area determination of the metal phase as analysed via automated post-experiment image analysis.

A discussion is given into the nature of interfacial tension where previously reported near-zero and negative interfacial tension energies are deemed unrealistic, with an alternative interpretation of the system treatment given to account for the phenomena observed.

The physical manifestation of interfacial energy change is discussed with regards to the severity of necking behaviour. This is used to evaluate the differences seen in metal morphologies between the current findings reported here and those previously reported in the literature of the most relevant systems.

Finally, an interrogation of the energy balance between free energy dissipation of reaction and interfacial tension cost is given. The inflection point in behaviour relative to the aluminium content can be seen to straddle the energy cost of interfacial area increase between the 3% and 4% $FeAl$ samples. Presenting an energetic reasoning to the observations given.

The nature of the results show hypothesis 7 to be true, and the exploration of energetic gain through reaction is seen to be a reasonable explanation for the change in behaviour. In addition, below the critical point of emulsification, there is still variation in behaviour, manifesting in these findings as the level to which the metal droplet surface perturbs; to a large extent at 3% aluminium, with reducing levels through 2%, 1% and 0% aluminium.

Chapter 9

Conclusions and Suggested Further Work

9.1 Conclusions

9.1.1 Macroscopic Dynamics

With the use of pilot plant data in chapter 5 a model for the calculation of residence time, metal circulation rate and % tap weight in the emulsion phase has been created for a BOF. The assumptions have been interrogated through critical assessment in comparison to previous literature, as well as new analytical XCT data with regard to the potential for decarburization in the emulsion phase through metal droplets.

Points of high residence time draw correlation with high bulk dephosphorization, whereby it is reasonable to state that dephosphorization is driven through the emulsion droplet interaction with slag. However, even though there is a reasonable trend in decarburization, the calculation of possible decarburization in the emulsion fell short ($\sim 60\%$) of the overall decarburization rate seen at times.

Metal circulation rate is seen to gradually increase with time, until end-blow periods where the level of decarburization is reduced, slag foaming collapses and droplets are likely to take on a more direct flight trajectory through the gas phase above the collapsed slag layer rather than through the previously stabilized emulsion. These factors couple to cause droplets to move faster/experience less hindrance to their movement in the late blow.

% Tap weight in the emulsion is seen to be considerably higher than is reported in most previous literature, giving further credence to the process being driven by material in the emulsion phase. There is however little to comment on trends within these findings: some heats appear to gradually increase; some stay relatively stable; and others show erratic behaviour throughout the blow. The main point to take however, is that there does not seem to be an overall reduction in metal within the emulsion for any heat between start and end values.

Overall the formulation of this macroscopic model gives a successful output and builds upon previous knowledge both direct from IMPHOS findings and the wider literature. It should however be noted that this study was on a 6 ton pilot scale, where all factors are scaled down apart from the velocity of the oxygen jet, which was still supplied at Mach 2 in resemblance to industrial practice. Factors such as a reduced vessel cross section, reduced material masses and reduced potential flight path (both horizontally and vertically) must be taken into serious consideration when these findings are considered at an industrial scale.

9.1.2 Driving Force of Spontaneous Emulsification

The chemical analysis of samples from $FeP - FeO$ reactive droplet systems has been conducted. The results show clearly that the phosphorus reaction was likely uninvolved in the emulsification process. In addition, SEM-SIMS was conducted to quantify oxygen levels in the droplet during the emulsification profile. It was found that the oversaturation of oxygen in the droplet and the re-equilibration of this transferring back to the slag phase was the likely cause of the phenomenon. This was backed up through the investigation of a zero P system, where again emulsification was witnessed. However, the emulsification profile was seen to be displaced from the original $FeP - FeO$ findings, which could well have been due to the additional P removal driving force in the initial phases of the experiment. Though, it would be crude to draw definition on this statement as HT-CSLM experiments are sensitive to usage variation through packing of slag, and maintenance of the chamber.

Further to this, the in-situ observation of the spontaneous emulsification phenomena through the use of $FeAl - SiO_2$ systems show initial aluminium content to cause the development of differing behaviour. The spontaneity and severity of emulsification showed reduction at 4% aluminium content and was further reduced to a non-emulsifying system at 3% aluminium.

The energy balance of increased interfacial area cost with the free energy dissipation of reaction is then considered. A clear relationship between the two can be seen to account for the occurrence of emulsification or lack thereof. In addition the level of free energy dissipation can be seen to be relative to the severity of perturbation growth in the non-emulsifying systems. This is a key finding in understanding the possibility for a system to emulsify or not.

9.1.3 Physical Pathway of Spontaneous Emulsification

Observations of emulsifying systems in low and high magnification show clearly a perturbation growth-driven pathway for emulsification. Theory is developed as to why perturbations grow, neck and bud, through a diffusion length lead argument. In addition, with the use of XCT and HT-CSLM image analysis the interfacial area increase during perturbation and emulsification is given; this is a key variable in the interfacial transfer pathway many elements are refined through during steelmaking.

High-resolution XCT of quenched perturbed samples allowed for the quantification of average perturbation growth size with respect to reaction time and a clear change in perturbation lifecycle profile is reported. The findings show that perturbations will grow in a 1:1 ratio untill 200 μm when necking occurs and a final maximum perturbation length of 470 μm before material breaks away from the parent droplet. The knowledge of how emulsification manifests gives insight into the parameters requiring control to predict and engineer the formation of a desired micro-emulsion.

Further to this, phase-field modelling techniques have been developed to incorporate the correct driving force and fluid mechanics to be able to map emulsification in two and three dimensions with respect to time. The linking of experimental techniques with modelling allows for the rationalization of a Fourier based modelling approach.

9.2 Potential Industrial Impact

The cumulative findings from this work have direct implication when considering the transient interfacial area during BOS processing. The macroscopic dynamics deduced through novel treatment of an extensive data set presents findings in a format allowing industry to fully appreciate the conditions and assumptions the results apply to. Specifically the residence times reported show strong consistency with those of model output in the literature, giving credence to the finding as well as information on how this parameter changed throughout the blow.

Results from the metal/slag HT-CSLM experiments show an individual droplet's surface area may increase by 10 times during a reactive process. When you consider at the time over half the total metal was found to be in droplet form within the emulsion phase of the BOF, this has the potential to greatly affect refining performances in the BOF, as well as the rate of reactions in ladles, the tundish, or even during casting.

Specifically these experiments do not include carbon as a reacting species, which is known to cause bloating and gas halos from the produced gases [35]. When we consider this, the low levels of carbon in the BOF towards end blow, and the potential for high levels of metal suspended in the slag phase with rising temperatures; potentially there is evidence as to why phosphorus reversion may occur.

9.3 Suggested Further Work

The following points give suggestions for future work to build on the current findings within this project:

1. Introduction of carbon to the spontaneous emulsification experiments. This would give a system with direct comparison to a significant profile of work in the literature as a technique validation.

2. Introduction of tertiary alloys to the emulsification experiments. This would allow for the observation of effects such as either interfacial site blocking or gas evolution to see which reactions are dominant in the cause of the observed phenomena. A prime example would be an $Fe - C - P$ droplet, where the evolution of a gas halo may inhibit dephosphorization/the flux of oxygen into the droplet and an inflection in behaviour from decarburization to dephosphorization led behaviour may be witnessed.

3. Continued development of the phase-field model presented, where the level of material movement can be interrogated to test the drive and extent of

emulsification similar to the results seen in the variable $FeAl$ profile of work. Once validated in this fashion the phase-field model should offer a robust prediction method for binary alloys. A key variable to explore would be the effect of changing FeO content in the slag phase.

4. The use and incorporation of data from more experimentally complex alloy systems to see how competing reactions affect each other (as discussed in point 2) would offer information required for the phase-field model to make the final step into an invaluable tool for informing slag/metal reactions.

5. Further use of XCT to interrogate quenched emulsion samples from the IMPHOS converter would allow for a robust droplet size distribution measurement in both a converter height profile and blow time profile. This has timely pertinence to many BOF modelling approaches being undertaken globally today (droplet size distribution is key to defining both the interfacial area and the governing behaviour of metal size fractions in the BOF emulsion).

6. Further additions of information to the macroscopic dynamic model are required to improve its accuracy. Addition of decarburization potential assigned to both the bulk bath and hot zone would improve calculation accuracy.

7. Finally, if the above scheme of work were to be conducted, it's combination along with processing parameter effects from the literature would offer the potential to truly understand and predict refining performance within the BOF.

Bibliography

[1] World Steel Association. World Steel Association Yearbook. Technical report, 2016.

[2] H. Tanabe and M. Nakada. Steelmaking technologies contributing to steel industries. *NKK Technical Review(Japan)*, 88(88), 2003.

[3] M. De Graef and M.E. McHenry. *Structure of Materials: An Introduction to Crystallography, Diffraction and Symmetry.* 2012.

[4] M.S. Millman, A. Kapilashrami, M. Bramming, and D. Malmberg. Imphos: improving phosphorus refining. Technical report, European Commision: Research Fund for Coal and Steel (RFCS), Brussels, 2011.

[5] D.C. Copley, J.W. Eberhard, and G.A. Mohr. Computed tomography part I: introduction and industrial applications. *JOM*, (January), 1994.

[6] T. Matsumiya. Steelmaking technology for a sustainable society. *Calphad*, 35(4):627–635, Dec 2011.

[7] U. Martin. Integrated Mill. Technical report, viewed 2017.

[8] E.T. Turkdogan. Physiochemical Aspects of Reactions in Ironmaking and Steelmaking Processes. *ISIJ*, 24, 1983.

[9] L.J. Westholm. The Use of Blast Furnace Slag for Removal of Phosphorus from Wastewater in Sweden - A Review. *Water*, 2(4):826–837, Oct 2010.

[10] W.J.B. Chater. Oxygen processes in the steel industry. *Chemical Engineering Science*, 3:105–IN5, Jan 1954.

[11] H. Yi, G. Xu, H. Cheng, J. Wang, Y. Wan, and H. Chen. An Overview of Utilization of Steel Slag. *Procedia Environmental Sciences*, 16:791–801, Jan 2012.

[12] M. Han and Y. Zhao. Dynamic control model of BOF steelmaking process based on ANFIS and robust relevance vector machine. *Expert Systems with Applications*, 38(12):14786–14798, Nov 2011.

[13] United States Environmental Protection Agency. Available and Emerging Technologies for Reducing Greenhouse Gas Emissions from the Iron and Steel Industry. Technical Report September, United States Environmental Protection Agency, 2012.

[14] M. Wang, Y. Lü, W. Yang, S. Li, and X. Xu. Selection of Oxygen Pressure in BOF Steelmaking. *Journal of Iron and Steel Research, International*, 18(11):12–16, Nov 2011.

[15] Z. Tian, B. Li, X. Zhang, and Z. Jiang. Double Slag Operation Dephosphorization in BOF for Producing Low Phosphorus Steel. *Journal of Iron and Steel Research, International*, 16(3):6–14, May 2009.

[16] M. Swinnerton. *The influence of slag evolution on BOF dephosphorisation.* PhD thesis, University of Wollongong, 2005.

[17] S. Kitamura, K. Miyamoto, H. Shibata, N. Maruoka, and M. Matsuo. Analysis of Dephosphorization Reaction Using a Simulation Model of Hot Metal Dephosphorization by Multiphase Slag. 95:313–320, 2009.

[18] M. Muhammed and Y. Zhang. A hydrometallurgical process for the dephosphorization of iron ore. *Hydrometallurgy*, 21:277–292, 1989.

[19] B.J. Monaghan, R.J. Pomfret, and K.S. Coley. The kinetics of dephosphorization of carbon-saturated iron using an oxidizing slag. *Metallurgical and Materials Transactions B*, 29(February):29–32, 1998.

[20] G. Hayman and D.A. Denton. Process heating, power and incineration. (July):1997, 1997.

[21] S. Emea. Some Observations on BOS Refining. *Ironmaking & Steelmaking*, pages 1–17, 2009.

[22] C.P. Manning and R.J. Fruehan. The rate of the phosphorous reaction between liquid iron and slag. *Metallurgical and Materials Transactions B: Process Metallurgy and Materials Processing Science*, 44(1):37–44, 2013.

[23] C. Cicutti, M. Valdez, T. Perez, J. Petroni, A. Gomez, R. Donayo, and L. Ferro. Study of Slag-Metal Reactions in an LD-LBE Converter. In *12 IAS Steelmaking Seminar*, volume 250, 1999.

[24] American Iron and Steel Institute. The Basic Oxygen Steelmaking (BOS) Process. Technical report, viewed 2017.

[25] R.M. Smailer. Phosphorus Control in DRI. In *ILFA Congress*, Mexico City, 1983.

[26] M.Y. Mohassab-Ahmed, H.Y. Sohn, and H.G. Kim. Phosphorus Distribution between Liquid Iron and Magnesia-Saturated Slag in H2/H2O Atmosphere Relevant to a Novel Ironmaking Technology. *Industrial & Engineering Chemistry Research*, 51(20):7028–7034, May 2012.

[27] C. Solans, D. Morales, and M. Homs. Spontaneous emulsification. *Current Opinion in Colloid and Interface Science*, 22:88–93, 2016.

[28] N. Sano and P.V. Riboud. *Advanced physical chemistry for process metallurgy*. Academic Press, 1997.

[29] M.A. Tayeb, R. Fruehan, and S. Sridhar. De-phosphorization in the DRI-EAF steelmaking and the effect of alumina. In *AISTech*, page 1, 2014.

[30] M.A. Tayeb, R. Fruehan, and S. Sridhar. Phosphorus partitioning during EAF refining of DRI based steel. In *International Symposium on Liquid Metal Processing & Casting*, pages 353–358, 2013.

[31] D. Wang. A novel method for controlling the surface morphology of polymeric membranes. *Journal of Membrane Science*, 169(1):39–51, 2000.

[32] M.S. Millman, A. Overbosch, A. Kapilashrami, D. Malmberg, and M. Brämming. Some observations and insights on BOS refining. *Ironmaking & Steelmaking*, 40(6):460–469, Aug 2013.

[33] B.J. Monaghan. *Kinetics of Liquid Iron Dephosphorization Using Lime Based Slags*. PhD thesis, University of Stathclyde, 1996.

[34] H.P. Mattila, I. Grigaliunaite, and R. Zevenhoven. Chemical kinetics modeling and process parameter sensitivity for precipitated calcium carbonate production from steelmaking slags. *Chemical Engineering Journal*, 192:77–89, Jun 2012.

[35] K.S. Coley and G. Brown. Kinetics of BOF Steelmaking. In *International Conference on the Technology of Ironmaking and Steelmaking*, Jamshedphur, India, 2014.

[36] E. Chen. *Kinetic Study of Droplet*. PhD thesis, McMaster University, 2012.

[37] H.W. Meyer, W.F. Porter, G.C. Smith, and J. Szekely. Slag-Metal Emulsions and their Importance in BOF Steelmaking, 1968.

[38] D.J. Price. L.D. Steelmaking: Significance of the emulsion in carbon removal. In *Process Engineering of Pyrometallurgy*, pages 8–15. 1974.

[39] R.F. Block, A. Masui, and G. Stolzenberg. Physical Processes in the Top Blown Oxygen Converter. *Arch Eisenhuttenwes*, 44:p357–361, 1973.

[40] R.C. Urquhart and W.G. Davenport. Foams and emulsions in oxygen steelmaking. *Canadian Metallurgical Quarterly*, 12(4):507–516, 1973.

[41] O.K. Tokovoi, A.I. Stroganov, and D.Y. Povolotskii. Tokovoi. *Steel USSR*, pages 116–117, 1972.

[42] W. Resch. *Kinetics of P Removal During O Top-Blowing Processes for P-Rich Fe*. Ph.d thesis, Technical University, Clausthal, 1976.

[43] V.I. Baptizmanskii, V.B. Okhoskii, K.S. Provirin, G.A. Shcherdrin, Y.A. Ardelyan, and A.G. Velichko. Investigation of the Physico-chemical Processes in the Reaction Zone with Oxygen Injection of the Metal. *Steel USSR*, 7:p329–331, 1977.

[44] S.C. Koria and K.W. Lange. A new approach to investigate the drop size distribution in basic oxygen steelmaking. *Metallurgical Transactions B*, 15(March):109–116, 1984.

[45] S.C. Koria and K.W. Lange. Breakup of Iron-Carbon Drops by a High Velocity Oxygen Gas Jet. *Canadian Metallurgical Quarterly*, 18(2):131–143, 1979.

[46] S.C Koria and K.W. Lange. Estimation of drop sizes in impinging jet steelmaking processes. *Ironmaking and Steelmaking*, 13(5):236–240, 1986.

[47] J. Gustavsson. *Reactions in the Lower Part of the Blast Furnace with Focus on Silicon*. PhD thesis, Royal Institute of Technology, 2004.

[48] Q. He. *Fluid Dynamics and Droplet Generation in the BOF Steelmaking Process*. PhD thesis, University of Wollongong, 1991.

[49] K.C. Mills, E.D. Hondros, and Z. Li. Interfacial phenomena in high temperature processes. *Journal of Materials Science*, 40(9-10):2403–2409, 2005.

[50] Subagyo, G.A. Brooks, and K.S. Coley. Residence time of metal droplets in slag-metal-gas emulsions through top gas blowing. *Canadian Metallurgical Quarterly*, 44:119–130, 2005.

[51] P. Kozakevitch. Foams and Emulsions in Steelmaking. *Journal of Minerals, Metals and Materials Society*, 22(7):57–58, 1969.

[52] G. Brooks, Y. Pan, and K. Coley. Modeling of trajectory and residence time of metal droplets in slag-metal-gas emulsions in oxygen steelmaking. *Metallurgical and Materials Transactions B*, 36(August), 2005.

[53] Q.L. He and N. Standish. A model study of residence time of metal droplets in the slag in BOF steelmaking. *ISIJ International*, 30(5):356–361, 1990.

[54] N. Dogan and G.A. Brooks. Comprehensive Model of Oxygen Steelmaking Part 2 : Application of Bloated Droplet Theory for Decarburization in Emulsion Zone. *ISIJ International*, 51:1093–1101, 2011.

[55] M. Pomeroy. *Droplet decarburization kinetics in steelmaking slags*. PhD thesis, McMaster University, 2011.

[56] K. Coley, F. Ji, G. Brooks, M. Rhamdhani, and Y. Pan. The Interface in Slag Reactions; a Moving Target. *Researchbank.Swinburne.Edu.Au*, 2009.

[57] B. Deo, A. Karamcheti, and A. Paul. Characterization of slag-metal droplet-gas emulsion in oxygen steel making converters. *ISIJ*, 36:658–666, 1996.

[58] F. Ganachaud and J.L. Katz. Nanoparticles and nanocapsules created using the ouzo effect: Spontaneous emulsification as an alternative to ultrasonic and high-shear devices. *ChemPhysChem*, 6(2):209–216, 2005.

[59] K. Bouchemal, S. Briançon, E. Perrier, and H. Fessi. Nano-emulsion formulation using spontaneous emulsification: Solvent, oil and surfactant optimisation. *International Journal of Pharmaceutics*, 280(1-2):241–251, 2004.

[60] J.C. López-Montilla, P.E. Herrera-Morales, S. Pandey, and D.O. Shah. Spontaneous Emulsification: Mechanisms, Physicochemical Aspects, Modeling, and Applications. *Journal of Dispersion Science and Technology*, 23(1-3):219–268, 2002.

[61] Y. Chung and A.W. Cramb. Direct observation of spontaneous emulsification and associated interfacial phenomena at the slag-steel interface. *Philosophical Transactions of the Royal Society A: Mathematical, Physical and Engineering Sciences*, 356(1739):981–993, Apr 1998.

[62] A.N. Assis, J. Warnett, S. Spooner, R.J. Fruehan, M.A. Williams, and S. Sridhar. Spontaneous Emulsification of a Metal Drop Immersed in Slag Due to Dephosphorization: Surface Area Quantification. *Metallurgical and Materials Transactions B*, pages 568–576, Dec 2014.

[63] M.A. Rhamdhani, G.A. Brooks, and K.S. Coley. Analysis of interfacial area changes during spontaneous emulsification of metal droplets in slag. *Metallurgical and Materials*, 37(December):1087–1091, 2006.

[64] M.A. Rhamdhani, K.S. Coley, and G.A. Brooks. Analysis of the source of dynamic interfacial phenomena during reaction between metal droplets and slag. *Metallurgical and Materials*, 36(October), 2005.

[65] M.A. Rhamdhani, K.S. Coley, and G.A. Brooks. Kinetics of metal/slag reactions during spontaneous emulsification. *Metallurgical and Materials*, 36(April), 2005.

[66] A. Jakobsson, M. Nasu, J. Mangwiru, K.C. Mills, and S. Seetharaman. Interfacial tension effects on slag-metal reactions. *Philosophical Transactions of the Royal Society A: Mathematical, Physical and Engineering Sciences*, 356(1739):995–1001, Apr 1998.

[67] H. Gaye, L.D. Lucas, M. Olette, and P.V. Riboud. Metal-Slag Interfacial Properties: Equilibrium Values and "Dynamic" Phenomena. *Canadian Metallurgical Quarterly*, 23(2):179–191, 1984.

[68] K.S. Coley. Progress in the kinetics of slag-metal-gas reactions, past present and future. *Journal of Mining and Metallurgy, Section B: Metallurgy*, 49(2):191–199, 2013.

[69] M.S. Millman, A. Overbosch, A. Kapilashrami, D. Malmberg, and M. Brämming. Observations on BOS refining. *Transactions of the Indian Institute of Metals*, 66(5-6):525–534, 2013.

[70] C. Liu and J. Shen. A phase field model for the mixture of two incompressible fluids and its approximation by a Fourier-spectral method. *Physica D: Nonlinear Phenomena*, 179(3-4):211–228, 2003.

[71] L.A. Caffarelli and N.E. Muler. An L∞ bound for solutions of the Cahn-Hilliard equation. *Archive for Rational Mechanics and Analysis*, 133(2):129–144, 1995.

[72] V.E. Badalassi, H.D. Ceniceros, and S. Banerjee. Computation of multiphase systems with phase field models. *Journal of Computational Physics*, 190(2):371–397, 2003.

[73] A. Costa e Silva. Estimating Viscosities in Iron and Steelmaking Slags in the CaO-Al2O3-MgO-SiO2-(TiO2) System with Basis on a Thermodynamic Model. *Journal of Materials Research and Technology*, 1(3):154–160, 2012.

[74] M. Selleby. An Assessment of the Ca-Fe-O-Si System. *Metallurgical and Materials Transactions B*, 28(August):577–596, 1997.

[75] B. Sundman. An assessment of the Fe-O system. *Journal of Phase Equilibria*, 12(2):127–140, 1991.

[76] L.Q. Chen and J. Shen. Application of semi-implicit Fourier-spectral method to phase field equations. 108:147–158, 1998.

[77] P. Wei, M. Sano, M. Hirasawa, and K. Mori. Kinetics of Phosphorus Transfer between Iron Oxide Containing Slag and Molten Iron of High Carbon Concentration under Ar-O2 Atmosphere. *ISIJ International*, 33(4):479–487, 1993.

[78] P. Wei, M. Sano, and M. Hirasawa. Kinetics of Carbon Oxidation Reaction between Molten. *ISIJ International*, 31(4):358–365, 1991.

[79] N. Dogan, G.A. Brooks, and M.A. Rhamdhani. Comprehensive Model of Oxygen Steelmaking Part 1: Model Development and Validation. *ISIJ International*, 51(7):1086–1092, 2011.

[80] J. Schoop, W. Resch, and G. Mahn. Reactions occurring during the oxygen top blown process and calculation of metallurgical control parameters. *Ironmaking and Steelmaking*, (2), 1978.

[81] J. Kumar, A. Attridge, P.K.C. Wood, and M.A. Williams. Analysis of the effect of cone-beam geometry and test object configuration on the measurement accuracy of a computed tomography scanner used for dimensional measurement. *Measurement Science and Technology*, 2011.

[82] C.L. Molloseau and R.J. Fruehan. The reaction behavior of Fe-CS droplets in CaO-SiO2-MgO-FeO slags. *Metallurgical and Materials Transactions B*, 2002.

[83] M.S. Millman, A. Overbosch, A. Kapilashrami, D. Malmberg, and M. Brämming. Study of refining performance in BOS converter. *Ironmaking & Steelmaking*, 38(7):499–509, Oct 2011.

[84] S. Sabah and G. Brooks. Splashing in Oxygen Steelmaking. *ISIJ International*, 54(4):836–844, 2014.

[85] S. Sabah and G. Brooks. Splash Distribution in Oxygen Steelmaking. *Metallurgical and Materials Transactions B*, 46(2):863–872, 2014.

[86] S. Spooner, A.N. Assis, J. Warnett, R. Fruehan, M.A. Williams, and S. Sridhar. Investigation into the Cause of Spontaneous Emulsification of a Free Steel Droplet; Validation of the Chemical Exchange Pathway. *Metallurgical and Materials Transactions B: Process Metallurgy and Materials Processing Science*, 47(4):2123–2132, 2016.

[87] A. Yang. *A pre-study of Hot Metal Desulphurization.* PhD thesis, Royal Institute of Technology, 2012.

[88] S. Basu. *Studies on dephosphorisation during steelmaking.* PhD thesis, Royal Institute of Technology, 2007.

[89] J. Diao, X. Liu, T. Zhang, and B. Xie. Mass transfer of phosphorus in high-phosphorus hot-metal refining. *International Journal of Minerals, Metallurgy, and Materials*, 22(3):249–253, 2015.

[90] L. Muhmood, N.N. Viswanathan, and S. Seetharaman. Some Investigations into the Dynamic Mass Transfer at the Slag-Metal Interface Using Sulfur: Concept of Interfacial Velocity. *Metallurgical and Materials Transactions B*, 42(3):460–470, Mar 2011.

[91] Y. Chung and A.W. Cramb. Dynamic and equilibrium interfacial phenomena in liquid steel-slag systems. *Metallurgical and Materials Transactions B*, 31(October):957–971, 2000.

[92] H. Gaye and P.V. Riboud. Oxidation kinetics of iron alloy drops in oxidizing slags. *Metallurgical Transactions B*, 8(2):409–415, 1977.

[93] D.J. Min and R.J. Fruehan. Rate of reduction of FeO in slag by Fe-C drops. *Metallurgical Transactions B*, 23(February):29–37, 1992.

[94] T. Gare and G.S.F. Hazeldan. Basic oxygen steelmaking: decarburization of binary Fe-C droplets and ternary Fe-C-X droplets in ferruginous slags. *Ironmaking and Steelmaking*, 8(4):169–181, 1981.

[95] H. Yin, H. Shibata, T. Emi, and M. Suzuki. “In-situ” Observation of Collision, Agglomeration and Cluster Formation of Alumina Inclusion Particles on Steel Melts. *ISIJ International*, 37(10):936–945, 1997.

[96] H. Yin, H. Shibata, T. Emi, and M. Suzuki. Characteristics of Agglomeration of Various Inclusion Particles on Molten Steel Surface. *ISIJ International*, 37(10):946–955, 1997.

[97] H. Shibata, Y. Arai, M. Suzuki, and T. Emi. Kinetics of peritectic reaction and transformation in Fe-C alloys. *Metallurgical and Materials Transactions B*, 31(5):981–991, 2000.

[98] H. Shibata, T. Emi, H. Yin, and M. Suzuki. Kinetics and morphology of crystal growth interacting with non-metalic inclusion in iron alloy melts. In *4th Decennial International Conference on Solidification Processing*, volume 37, pages 230–233, 1997.

[99] P.V. Riboud and L.D. Lucas. Influence of Mass Transfer Upon Surface Phenomena in Iron and Steelmaking. *Canadian Metallurgical Quarterly*, 20(2):199–208, 1981.

[100] A. Sanfeld. Influence of capillarity on chemical stability and of electric field on surface tension near the critical point. *Philosophical Transactions of the Royal Society A: Mathematical, Physical and Engineering Sciences*, 356:819–828, 1998.

[101] P. Liu, E. Harder, and B.J. Berne. On the Calculation of Diffusion Coefficients in Confined Fluids and Interfaces with an Application to the Liquid - Vapor Interface of Water. *J. Phys. Chem*, pages 6595–6602, 2004.

[102] J.C. López-Montilla, P.E. Herrera-Morales, and D.O. Shah. New method to quantitatively determine the spontaneity of the emulsification process. *Langmuir*, 18(11):4258–4262, 2002.

[103] H.A. Hartung and O.K. Rice. Some Studies of Spontaneous Emulsification. *Journal of Colloid Science*, 10(5):436–439, 1955.

[104] S. Sahin, O. Bliznyuk, A.R. Cordova, and K. Schroen. 2016 Microfluidic EDGE emulsification, the importance of interface interaction on droplet formation and pressure stability. *Scientific reports Nature*, 6(26407):1–7, 2016.

[105] M.V.D. Waarden. The process of spontaneouse emulsification. *Koninklijke/Shell-Laboratorium*, pages 140–150, 1952.

[106] T. Nishimi and C.A. Miller. Spontaneous Emulsification Produced by Chemical Reactions. *Journal of colloid and interface science*, 237(2):259–266, 2001.

[107] J.B. Lewis and H.R.C. Pratt. Oscillating Droplets. *Nature*, 171(4365):1155–1156, Jun 1953.

[108] F.H. Garner, C.W. Nutt, and M.F. Mohtadi. Pulsation and Mass Transfer of Pendent Liquid Droplets. *Nature*, 175(4457):603–605, apr 1955.

[109] D.A. Haydon. Oscillating Droplets and Spontaneous Emulsification. *Nature*, 176(4487):839–840, Oct 1955.

[110] W.T. Minehan and G.L. Messing. Synthesis of spherical silica particles by spontaneous emulsification. *Colloids and Surfaces*, 63(1-2):163–171, 1992.

[111] J. Komaiko and D.J. McClements. Low-energy formation of edible nanoemulsions by spontaneous emulsification: Factors influencing particle size. *Journal of Food Engineering*, 146:122–128, 2015.

[112] M. Auinger, P. Ebbinghaus, A. Blumich, and A. Erbe. Effect of Surface Roughness on optical heating of metals. *Journal of the European Optical Society-Rapid Publications*, 9(14004):1–13, 2014.

[113] W. Hoyer, I. Kaban, and M. Merkwitz. Liquid-liquid interfacial tension in immiscible binary Al-based alloys. *Journal of Optoelectronics and Advanced Materials*, 5(5):1069–1073, 2003.

[114] J.A. Warren and W.J. Boettinger. Prediction of dendritic growth and microsegregation patterns in a binary alloy using the phase-field method. *Acta Metallurgica Et Materialia*, 43(2):689–703, 1995.

[115] L. Gránásy, T. Pusztai, J.A. Warren, J.F. Douglas, T. Börzsönyi, and V. Ferreiro. Growth of 'dizzy dendrites' in a random field of foreign particles. *Nature Materials*, 2(2):92–96, 2003.

[116] A.H. Saberi, Y. Fang, and D.J. McClements. Effect of glycerol on formation, stability, and properties of vitamin-E enriched nanoemulsions produced using spontaneous emulsification. *Journal of Colloid and Interface Science*, 411:105–113, 2013.

[117] D. Quintanar-Guerrero, E. Allémann, E. Doelker, and H. Fessi. A mechanistic study of the formation of polymer nanoparticles by the emulsification-diffusion technique. *Colloid and Polymer Science*, 275(7):640–647, 1997.

[118] J. Ye and Y. Sahai. Interaction and interfacial tension between aluminum alloys and molten salts. *Materials transactions-JIM*, 37(9):1479–1585, 1996.

[119] Ram (McMaster University) Murarka. *Surface Tension Measurements on Iron and Iron-Oxygen Alloys*. PhD thesis, McMaster University, 1971.

[120] J.W. Cahn. Thermodynamics of Solid and Fluid Surfaces. In J. Blakely W. Johnson, editor, *Papers presented at a seminar of the American society for metals*, pages 3–23, Ohio, 1977.

[121] R. Defay, A. Sanfeld, and A. Steinchen. *J. Chim. Phys. Physicochim. Biol*, 69:1374–1380, 1972.

[122] R. Defay, A. Sanfeld, and A. Steinchen. *J. Chim. Phys. Physicochim. Biol*, 7:895, 1973.

[123] J. Friedel and J.F. Instabilit. Instabilité d'une interface en présence de gradients de potentiel chimique. *Journal de Physique Lettres*, 41(10):251–254, 1980.

[124] A. Kasama, A. McLean, W.A. Miller, Z. Morita, and M.J. Ward. Surface Tension of Liquid Iron and Iron-Oxygen Alloys. *Canadian Metallurgical Quarterly*, 22(1):9–17, 1983.

[125] K. Morohoshi, M. Uchikoshi, M. Isshiki, and H. Fukuyama. Surface Tension of Liquid Iron as Functions of Oxygen Activity and Temperature. *ISIJ International*, 51(10):1580–1586, 2011.

[126] K. Ogino, S. Hara, T. Miwa, and S. Kimoto. The Effect of Oxygen Content in Molten Steel on the Interfacial Tension between Molten Steel and Slag. *Tetsu-to-Haganè*, 65(14):2012–2021, 1979.

Appendix A

Appendix 1: Method of determining perturbation length

In order to measure the perturbation length we have to define a “quiescent” surface location at which to measure from as well as define the separation of the surface into distinct non-overlapping perturbations. To do this an effective removal of the inner droplet is carried out in the XCT analysis software, followed by a systematic measurement from a set point to the tip of each perturbation.

The first stage is to define an average minimum of the wells between raised points on the droplet surface (the bottom of the perturbations). A sphere whose edge overlaps the average minimum is then created, such as figure A.1.

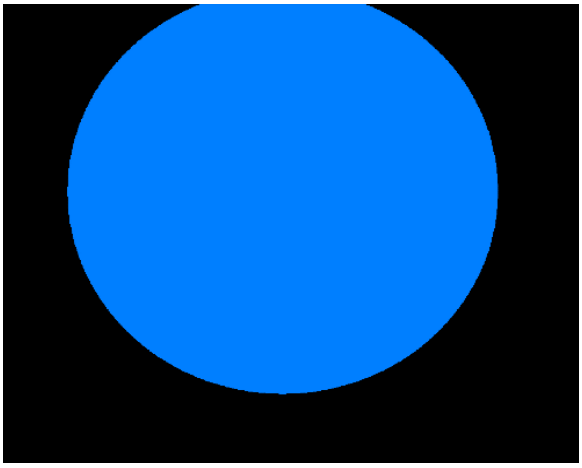

Figure A.1: An example of the sphere created from the minima averaging of perturbations

This sphere is then subtracted from the original droplet geometry, leaving only the surface of the droplet; the layer which is made due to perturbation of the system. Figure A.2a shows a 2D slice of the 20-second sample, and figure A.2b shows the residual "surface" layer of the droplet after removal of the internal droplet.

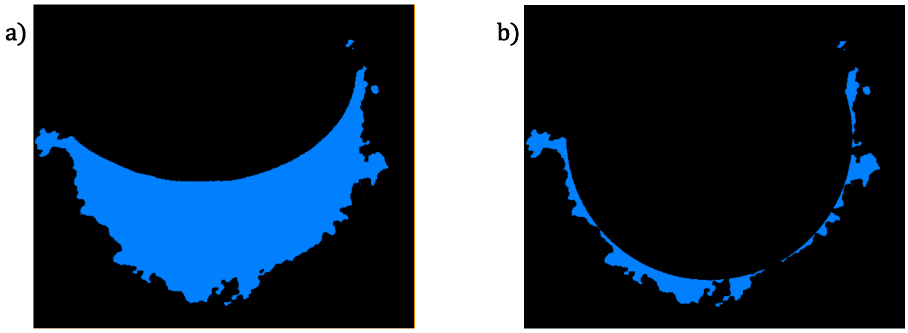

Figure A.2: a) A 2D slice of the 20-second sample, where the metal has been highlighted in blue and all other material removed. b) The resultant volume left after removal of the interior of the droplet through overlapping of the minima averaging sphere.

We then use the software to automate a segmentation of the remaining surface layer via splitting of the volume between the originally identified perturbation minima. This results in segmentation of the 2D slice in this example as seen in figure A.3. As visible from figure A.3, the software was not completely able to segment every perturbation, mainly due to the phenomena depicted in the main papers figure 7.13 "diverging growth". However this element of error was consistent across both the 20- and 25-second samples and was unavoidable in order to standardize and replicate the measurement for the number of perturbations present in the systems.

Grey-scale values are then assigned to each voxel within the reconstruction with regards to their radial distribution from the centre of the sphere (figure A.1) which was removed from the original droplet. Where all voxels under the original sphere location are assigned as pure black, followed by a linear function of 28-point grey-scale distribution over the rest of the image as seen in figure A.4.

Overlapping the radial grey scale and the segmented surface volume then allows us to calculate the outer most point of each perturbation by defining its grey-scale value which is directly related to its distance from the perturbation minima.

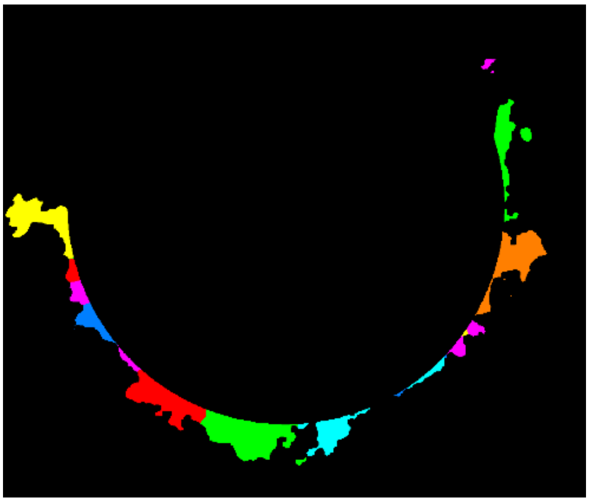

Figure A.3: The effective segmentation of the droplet surface as a result of the automated method within the software splitting at defined minima. Each colour represents a separately defined perturbation.

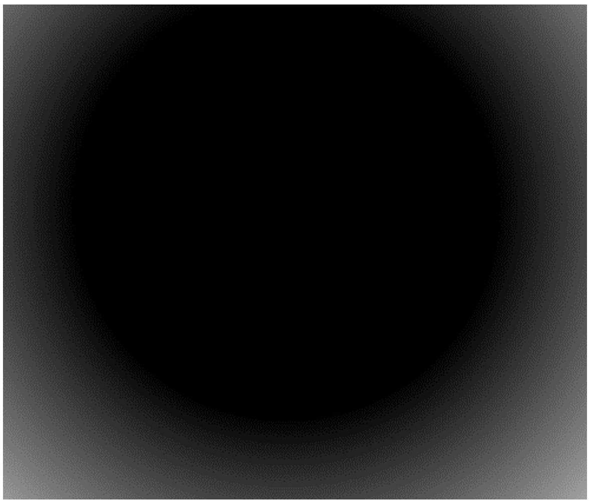

Figure A.4: The grey-scale distribution of the sample space as defined from the original average minima produced sphere size. The black circle is in the space of the sphere and the grey values lighten radially outwards from its surface.